SAPIENZA UNIVERSITY OF ROME
AND
UNIVERSITY OF ROME TOR VERGATA

PH.D. IN ASTRONOMY, ASTROPHYSICS
AND SPACE SCIENCE

CYCLE XXX

An enhanced sensitivity procedure for continuous gravitational wave detection: targeting the Galactic Center

Ornella Juliana Piccinni
A.Y. 2016/2017

Supervisor: Prof. Sergio Frasca

Co-supervisor: Prof. Piero Rapagnani

Coordinator: Prof. Roberto Capuzzo Dolcetta

Deputy Coordinator: Prof. Pasquale Mazzotta

SAPIENZA
UNIVERSITÀ DI ROMA

An enhanced sensitivity procedure for continuous gravitational wave detection: targeting the Galactic Center

Scuola di dottorato Vito Volterra

Dottorato di Ricerca in Astronomy, Astrophysics and Space Science – XXX Ciclo

Candidate

Ornella Juliana Piccinni
ID number 1340503

Thesis Advisor	Co-Advisor
Prof. Sergio Frasca	Prof. Piero Rapagnani

A thesis submitted in partial fulfillment of the requirements
for the degree of Doctor of Philosophy in Physics

October 2017

Thesis not yet defended

An enhanced sensitivity procedure for continuous gravitational wave detection: targeting the Galactic Center
Ph.D. thesis. Sapienza – University of Rome

© 2017 Ornella Juliana Piccinni. All rights reserved

This thesis has been typeset by LaTeX and the Sapthesis class.

Version: October, 31, 2017

Author's email: ornellajuliana.piccinni@uniroma1.it

Contents

Introduction **vii**

I Experimental detection of gravitational waves **1**

1 Gravitational waves **3**
- 1.1 Gravitational waves as a solution of the Einstein Field Equations . . 3
- 1.2 Gravitational wave emission 4
- 1.3 Gravitational waves sources and signals 5
- 1.4 Sources of continuous gravitational waves 6

2 The LIGO and Virgo experiments **9**
- 2.1 Gravitational wave interferometric detectors 9
- 2.2 Noise sources 10
- 2.3 The Data acquisition 11
- 2.4 Detector Characterization 12

3 Spectral noise investigations **15**
- 3.1 Spectral noise hunting 15
- 3.2 NoEMi: Noise frequency Event Miner 16
- 3.3 Spectral lines and couplings 16
  - 3.3.1 Lines in O1 and O2 in LIGO 17
  - 3.3.2 Lines around GW170814 in Virgo 17
  - 3.3.3 Lines around GW170817 in Virgo 18

II Data analysis for CW **21**

4 Continuous GW searches **23**
- 4.1 The signal model 23
- 4.2 Type of CW searches 24
  - 4.2.1 Targeted searches and narrow-band searches 25
  - 4.2.2 Directed searches 25
  - 4.2.3 All-sky searches 26
  - 4.2.4 Searches for CW in binary systems 26
- 4.3 The FrequencyHough transform 27

5 The Band Sampled Data collection 29
5.1 The Short FFT Database . . . 29
5.2 The method . . . 30
5.3 BSD creation . . . 31
5.3.1 The analytic signal and its reduced form . . . 34
5.3.2 Data cleaning . . . 35
5.4 Hetherodyne correction . . . 36
5.5 Possible applications of the BSD framework . . . 37
5.6 Test with simulated signals . . . 38
5.6.1 Software injections . . . 38
5.6.2 Hardware injections . . . 39

6 Directed search method based on BSD data 43
6.1 Multi-Doppler correction . . . 43
6.2 Peakmaps . . . 45
6.3 Hough maps . . . 47
6.4 Candidate selection . . . 48
6.4.1 Coincidences . . . 50
6.5 Candidate Follow-up . . . 51
6.6 Sensitivity estimation . . . 57
6.6.1 Peaks probability . . . 57
6.6.2 Hough number count probability . . . 58
6.6.3 Peaks threshold . . . 58
6.6.4 Hough counts threshold . . . 59
6.6.5 A formula for the sensitivity . . . 60

III Astrophysics application 61

7 The Galactic Center search 63
7.1 The Galactic Center area . . . 63
7.1.1 GC neutron star population . . . 65
7.2 Motivation for a GC search of CW signals . . . 66
7.3 The BSD Galactic Center search setup . . . 66
7.4 Choice of the parameter space . . . 67
7.4.1 Frequency grid . . . 67
7.4.2 Spin-down grid . . . 68
7.4.3 Sky grid . . . 70
7.4.4 Final parameter space . . . 71
7.5 Results . . . 72
7.5.1 Candidate selection . . . 72
7.5.2 Candidate coincidences . . . 74
7.5.3 Candidates follow-up results . . . 77
7.6 Sensitivity of the search . . . 83

A The *cont* and *tfstr* structures 89

B Few BSD header functions 91

C Instrumental lines removed for the search 97

Introduction

The recent announcement by the LIGO and Virgo Collaborations of the direct detection of gravitational waves started the era of gravitational wave astrophysics. Up to now there have been five confirmed detections (GW150914, GW151226, GW170104, GW170814 and GW170817). Each of the GW events detected so far, shed light on multiple aspects of gravity. The first four events were due to the coalescence of a binary black hole system. August 17th 2017 marked the beginning of the so-called Multi-Messenger astronomy: the binary neutron star merger GW170817 has been observed almost simultaneously by LIGO and Virgo interferometers and several telescopes in space and on Earth, which detected the electromagnetic counterpart of this event (first as a short gamma-ray burst, GRB 170817A, and then in the visible, infra-red and X-ray bands).

These last two years of great scientific discoveries would not have been possible without the constant work of generations of scientists all around the world. This worldwide scientific and technological effort, culminated in the first direct observation of gravitational waves in September 14th 2015, has been awarded with the 2017 Nobel Prize in Physics to Rainer Weiss, Barry C. Barish and Kip S. Thorne. August 2017 has been also *the* month for the Advanced Virgo detector located near Pisa in Italy, which joined the two LIGO interferometers in the second observational scientific run (O2) of the Advanced detector Era.

Commissioning and detector characterization activities required a lot of effort and manpower to reach the sensitivity level and stability needed for the detections. In fact, detector characterization activities continue also during data taking, providing important data quality information to data analysis groups.

Although in few years several important results have been obtained, this is just the beginning. Indeed there are several other potential sources of gravitational waves not yet detected. In particular, the search for continuous gravitational waves, which are very weak but long and persistent signals, is a very active field. The most probable sources of continuous waves signals are rapidly rotating asymmetric neutron stars, both isolated or in binary systems.

In this thesis I will summarize my 3 years PhD work done in the Rome Virgo group. The main subject is the search for gravitational waves signal emitted by isolated non-axisymmetric rotating neutron stars. After a short introduction to gravitational waves and to the principles of detection (Chapters 1 and 2), in Chapter 3 I will talk about my contribution to detector characterization activities, performed during Virgo commissioning and science runs. I will describe the role played by a spectral lines monitoring tool, called NoEMi (Noise Event Miner), developed by the

Rome group in 2010, which I have been responsible for, during these 3 years. NoEMi has been used through O1 and O2 Observational runs and in the commissioning phase of LIGO and Virgo detectors. It has been also used for Virgo data validation of the two gravitational wave events GW170814 and GW170817 and it is currently used for the post-commissioning identification of instrumental lines in both LIGO and Virgo data.

The second part of the Thesis is dedicated to the new data analysis framework I have developed in the context of continuous gravitational wave searches. It consists of a novel organization of the data, the so-called Band Sampled Data collection, and of several functions needed to efficiently operate on the data itself. This framework dramatically improves the flexibility in data handling, allowing the user to select and manipulate data in a very efficient way, by properly taking into account the characteristics and the needs of the specific type of search she/he is doing. Overall it results in better computational performance (which, at fixed available computing resources, means better search sensitivity) and immediate adaptability to different kinds of search or, even, to different portions of the same multi-step analysis pipeline.

To test the capability of this new framework, a complete pipeline for directed searches of continuous waves signals has been developed using the BSD framework. The pipeline has been applied to a real gravitational wave search (Part III), pointing to the Milky Way central region for which a large number of unknown neutron stars are expected to exist. The results of this search, done using the last observational run (O2) of the LIGO detectors, didn't show any evidence of the presence of continuous wave emission from the few inner parsecs of our Galaxy. Interesting limits on the minimum detectable strain and ellipticity of the sources have been placed. This is the first directed search for continuous waves signals performed within the Virgo Collaboration and the first LIGO-Virgo O2 directed search toward the Galactic center.

The BSD framework developed in this thesis project will become the core of all CW searches of the Rome Virgo group. Furthermore, it represents a great starting point for the development of different types of searches, like that for long transient signals that could be emitted by the post-merger remnant of GW170817.

Part I

Experimental detection of gravitational waves

"It doesn't matter how beautiful your theory is, it doesn't matter how smart you are. If it disagrees with experiment, it's wrong."
Richard Feynman during a lecture (1964)

Chapter 1

Gravitational waves

Predicted in 1916 by Albert Einstein on the basis of his theory of General Relativity [40], gravitational waves (GW) were detected for the first time by the LIGO and Virgo Collaborations in 2015, almost 100 years after their theoretical prediction [7]. The first signal, detected by the Advanced LIGO detectors on September 14th 2015, was due to the inspiral and coalescence of two black holes (of $\sim 36 M_{\odot}$ and $\sim 29 M_{\odot}$ respectively) [11]. Several theoretical expectations about the nature of gravitational waves have been confirmed by the detections, as explained in [17, 8, 9, 12, 7]. In particular the two tensor polarization nature of GW has been probed thanks to the presence of the Virgo detector [18]. In the following sections the main properties of GWs in the context of General Relativity will be discussed. Standard textbooks about General Relativity can be found in [44, 66, 87] while for the part concerning GW and its detection see [60, 84] .

1.1 Gravitational waves as a solution of the Einstein Field Equations

Gravitational waves are ripples in the curvature of space-time that are generated in principle by any massive body with a time-variable quadrupole moment. The connection between the source mass-energy distribution and space-time curvature is given by the Einstein Fields Equations (EFE):

$$R_{\mu\nu} - \frac{1}{2} g_{\mu\nu} R = \frac{8\pi G}{c^4} T_{\mu\nu} \tag{1.1}$$

where $g_{\mu\nu}$ is the metric tensor, which describes the space-time, $R_{\mu\nu}$ is the *Ricci curvature tensor*, while R is the *scalar curvature* and is defined as the trace of the Ricci tensor. G and c are, respectively, the gravitational constant and the speed of light in vacuum. The right hand side of Eq. 1.1 depends on $T_{\mu\nu}$, the stress-energy tensor that represents the energy density of the source which produce the curvature. One of the possible solutions of Eq. 1.1 can be obtained using the *weak field limit* of the metric tensor $g_{\mu\nu}$, for which the metric is approximated as the sum of a flat Minkowski metric plus a small perturbation $h_{\mu\nu}$. In this limit, and properly exploiting the gauge freedom, the Einstein equations can be approximated as linear equations:

$$\begin{cases}\Box\bar{h}_{\mu\nu} = -\frac{16\pi G}{c^4}T_{\mu\nu} \\ \partial_\mu \bar{h}^\mu_\nu = 0\end{cases} \quad . \tag{1.2}$$

where the traceless tensor perturbation $\bar{h}_{\mu\nu} = h_{\mu\nu} - \frac{1}{2}\eta_{\mu\nu}h^\lambda_\lambda$ has been used. The solution of Eq. 1.2 in vacuum ($T_{\mu\nu} = 0$) tells us that the perturbation of a flat space-time propagates as a plane wave traveling at the speed of light; these are the gravitational waves, predicted by Einstein's theory of gravity.

The simplest solution of the wave equation in vacuum is a monochromatic plane wave:

$$\bar{h}_{\mu\nu} = \Re\{A_{\mu\nu}e^{ik_\alpha x^\alpha}\} \tag{1.3}$$

where $A_{\mu\nu}$ is the wave amplitude and k_α is the wave vector. If we consider a wave vector $k_\mu = (\omega, 0, 0, k)$, with $c = 1$, which lies along the z-axis, using the *Transverse-Traceless gauge* (T-T), in which $\bar{h}_{\mu\nu} = h_{\mu\nu}$, the solution of the linearized EFE in vacuum, 1.2, is given by:

$$h_{\mu\nu} = \begin{pmatrix} 0 & 0 & 0 & 0 \\ 0 & h_+ & h_\times & 0 \\ 0 & h_\times & -h_+ & 0 \\ 0 & 0 & 0 & 0 \end{pmatrix} e^{ikz - i\omega t}, \tag{1.4}$$

where h_+ and $h_\times$ are the amplitudes of the two independent polarizations of the gravitational wave. That is, a gravitational wave has only two physical degrees of freedom, which correspond to the two possible polarization states on the plane orthogonal to the direction of propagation of the wave. The two polarization patterns differ by a rotation of 45 degrees around the z-axis. If we want to quantify the effect of a gravitational wave we need to study the induced relative motion of at least two particles. For two particles at distance L_0 at the time $t = 0$, the effect of a gravitational wave traveling orthogonally to the pair, is to change their relative distance proportionally to the amplitude of the wave:

$$\delta L(t) \propto L_0 h(t) \tag{1.5}$$

If we consider a ring of free falling test particles in space, their relative position changes for a gravitational wave impinging orthogonally to the ring plane, as shown in Figure 1.1.

1.2 Gravitational wave emission

We use equation 1.2 in order to estimate the waveform emitted by a physical system described by the stress-energy tensor $T^{\mu\nu}$. For doing this we use the so-called *slow-motion approximation* i.e., we consider the region occupied by the GW source much smaller than the wavelength of the emitted gravitational radiation $\lambda_{GW} = \frac{2\pi c}{\omega}$, which is reasonable for astrophysical bodies [66].

Using the conservation law satisfied by the stress-energy tensor, $T^{\mu\nu}_{,\nu} = 0$, it is possible to express the emitted waveform through the quadrupole moment tensor of the source which is defined as:

$$q^{kj}(t) = \frac{1}{c^2}\int_V T^{00}\left(t, x^i\right) x^k x^j d^3x \quad k, j = 1, 3 \tag{1.6}$$

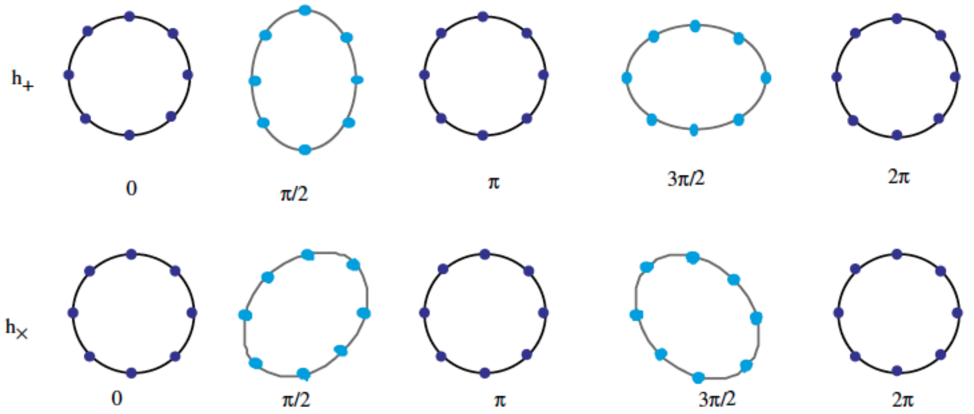

Figure 1.1. Illustration of the effect of a gravitational wave on a ring of test masses according to the two polarization modes h_+ and $h_\times$. The circle lays on the plane transverse to the direction of propagation of the wave.

Thus, the solution of (1.2) in the T-T gauge, can be written as:

$$\begin{cases} h_{\mu 0} = 0 & \mu = 0..3 \\ h_{ik}\left(t, r\right) = \frac{2G}{c^4 r}\left[\frac{d^2}{dt^2} Q_{ik}^{TT}\left(t - \frac{r}{c}\right)\right] \end{cases} \tag{1.7}$$

Here $Q_{ik}^{TT} = P_{ikmn} q^{mn}$ is the transverse-traceless part of the quadrupole moment (1.6), where P_{ikmn} is the transverse-traceless projector and r is the distance between the source and the observer. Equation 1.7 describes the time-dependent waveform emitted by the source. Since $\frac{G}{c^4} \simeq 8 \times 10^{-50} \frac{s^2}{g\, cm}$, sources of potentially detectable GW can only be large massive bodies with strong accelerations like astrophysical compact objects, as neutron stars and black holes. Moreover, it is clear from Eq. 1.7 that in order to produce gravitational waves a certain degree of asymmetry is needed. This happens with non-axisymmetric rotating stars, non-spherical gravitational collapses or in the coalescence of massive bodies.

1.3 Gravitational waves sources and signals

Gravitational waves sources can be roughly divided in four main categories: compact binary coalescences (CBC), unmodeled transients (burst), continuous waves (CW) and stochastic gravitational-wave background (SGWB). For a detailed description of the main GW sources see [83]. Here we briefly review the main features of the different categories of GW sources.

- **Coalescing binaries:** compact binary systems, made of neutron stars or black holes, emit a well modeled gravitational wave signal. The amplitude and the frequency of the signal (called *chirp*) increase in time as the two objects spiral-in, until they merge producing a remnant which nature depends on the characteristics of the initial bodies and, in particular, the total mass and angular momentum: a black hole, a temporary neutron star which later collapses to a black hole, a stable neutron star. Considering the portion of the signal within the sensitivity band of Earth-based interferometric detectors, CBC signals are transient, with duration from a fraction of a second to a few minutes. Typically, matched filtering with large template banks is used to search for these signals. When the binary system contains at least one neutron star, the coalescence is expected to produce also electromagnetic radiation, as it has been confirmed by GW170817 [19, 16].

- **Bursts signals:** are expected to be produced for instance by supernova explosions. These signals are short-lived and difficult to model. Gravitational wave bursts can, in principle, be detected looking at localized excess power in the time-frequency domain. Many gravitational wave burst sources are expected to produce observable emission in more traditional channels, like electromagnetic and neutrino [13, 21]. It should be mentioned that algorithms used for unmodeled searches can, in fact, be able to detect also well known signals, if strong enough. For instance, the first GW event, GW150914, has been first detected by a 'burst' on-line pipeline [10].

- **Continuous waves:** the main sources for continuous waves signals are fast spinning asymmetric neutron stars (NSs), isolated or in binary systems. These are expected to emit a long-lived signal and with a well defined waveform: a nearly sinusoid with frequency slightly varying over times much longer than the observational time. Matched filtering can be applied to search for such signals when the source parameters are known with high accuracy [90], [15], otherwise less sensitive semi-coherent searches must be done. A more detailed discussion of CW signals will be done in the next section.

- **Stochastic background:** a stochastic gravitational wave background can arise from cosmological sources such as inflation, cosmic strings or primordial GW from the Big Bang and also from the superimposition of the signals emitted by astrophysical objects (CBC, Supernovae, NS) [82]. This signal is long-lived and stochastic in nature. Gravitational waves searches have placed constraints on the cosmological stochastic gravitational wave background stronger than the indirect limits provided by the Big Bang Nucleosynthesis and microwave background [14, 23].

1.4 Sources of continuous gravitational waves

For a detailed review of continuous gravitational waves sources see references [56], and Section 2.5 in [83]. Here we will briefly give an overview about the possible sources of continuous gravitational waves, focusing on isolated neutron stars. For a review of the current knowledge about NSs masses, radii and equation of state see [71]. Neutron stars are very compact objects, with mass around one solar mass and radius of about 10 km, formed after the gravitational collapse of massive ($M > 8M_\odot$) progenitor stars (see Table 1.1). The majority of known neutron stars are pulsars, which emit a beam of electromagnetic radiation due to the different inclination of the magnetic axis with respect to the spin axis. This radiation is observable when

Table 1.1. Comparison between physical properties of NSs and the Sun. $\rho_0 = 2.8 \times 10^{14}$ $\mathrm{g\,cm^{-3}}$ is the *normal nuclear density*, the mass density of nucleon matter in heavy atomic nuclei.

	Neutron Star	Sun
Mass M	$\sim 1.4 M_\odot$	$M_\odot = 1.989 \times 10^{33}\,\mathrm{g}$
Radii R	$10\,\mathrm{km}$	$6.96 \times 10^5\,\mathrm{km}$
Mean density $\bar{\rho} \simeq 3M/(4\pi R^3)$	$(2-3)\rho_0$	$1.408\ \mathrm{g\,cm^{-3}}$
Central density	$(10-20)\rho_0$	$1.622 \times 10^2\ \mathrm{g\,cm^{-3}}$
$E_{grav} \sim GM^2/R$	$5 \times 10^{53}\,\mathrm{erg}$	$3 \times 10^{48}\,\mathrm{erg}$
Surface gravity $\sim GM/R^2$	$2 \times 10^{14}\ \mathrm{cm\,s^{-2}}$	$28 \times 10^5\ \mathrm{cm\,s^{-2}}$

the beam emitted along the magnetic axis, points toward the Earth. The existence of neutron stars, first proposed by W. Baade and F. Zwicky in 1934 [32], has been confirmed by the first observation of pulsars in 1967 by J. B. Burnell and A. Hewish [46].

The most likely detectable sources of CW signals are galactic non-axisymmetric neutron stars with rotational periods of $10^{-2} - 10^{-3}$ s. Several mechanisms have been proposed for the asymmetry: residual crustal defects produced by the rapid cooling of the nascent neutron star [49]; deformation induced by a large internal magnetic field or due to a non-axisymmetric distribution of magnetic field energy inside the crust [75]; excitation of r-mode instabilities damped by internal viscosity of rotating neutron stars [50]. Another promising target of CW searches are accreting neutron stars in Low Mass X-ray Binaries (LMXBs) systems. Typically those neutron stars have millisecond rotation periods and the quadrupole mass deformation could be due to the asymmetric accretion of material from the companion. As can be seen from Figure 1.2, obtained using the Australia Telescope National Facility (ATNF) pulsar database described in [61], the majority of the known millisecond pulsars are in binary systems.

The structure of a neutron star is not well defined yet. The detection of GWs emitted by neutron stars, will help to improve our knowledge of these compact objects [70]. In the prototypical case of a neutron star rotating around one of its principal axis of inertia, the gravitational wave amplitude h_0 is [51]:

$$h_0 = \frac{4\pi^2 G}{c^4} \frac{I_{zz} f^2}{r} \epsilon \tag{1.8}$$

where $f = 2f_{rot}$ is the gravitational wave frequency emitted by the source, I_{zz} is the moment of inertia with respect to the rotation axis, and r is the distance. The ellipticity is defined as $\epsilon = \frac{I_{xx} - I_{yy}}{I_{zz}}$ which is the fractional difference among the moments of inertia in the rotation plane. For a neutron star at a distance of 1 kpc, spinning at 500 Hz and assuming a "canonical" value for the moment of inertia of 10^{38} kg m^2 and an ellipticity of 10^{-6}, which is approximately the maximum value foreseen for a standard neutron star structure, the amplitude of the GW signal at the detector is about $4 \cdot 10^{-25}$. A theoretical upper limit to the signal amplitude, called *spin-down limit*, can be computed equating the gravitational wave luminosity to the rotational energy loss of the star: $L_{GW} = \frac{32G}{5c^5} \Omega^6 \epsilon^2 I^2 = -\dot{E}_{rot}$, with $\Omega = 2\pi f$. This

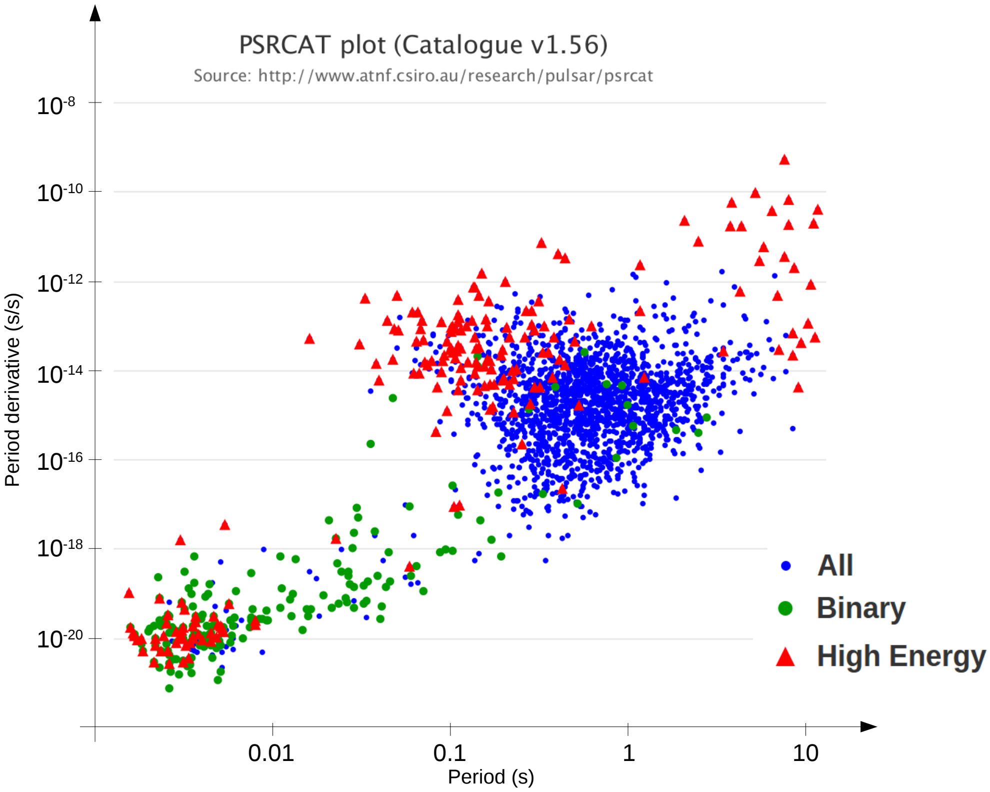

Figure 1.2. Period derivatives and period (s) measured for known radio pulsars (blue dots). Green dots are pulsars found in binary systems; radio pulsars with high energy pulsation are labeled with red triangles. Credit to the online ATNF Pulsar Database [31].

corresponds to the assumption that all the observed star spin-down, expressed by the time derivative of the rotation frequency, is due to the emission of gravitational waves:

$$h_0^{\mathrm{sd}} = \left(\frac{5}{2} \frac{G I_{zz} \dot{f}_{\mathrm{rot}}}{c^3 d^2 f_{\mathrm{rot}}} \right)^{1/2} = 8.06 \times 10^{-19} \frac{I_{38}^{1/2}}{d_{\mathrm{kpc}}} \sqrt{\frac{|\dot{f}_{\mathrm{rot}}|}{f_{\mathrm{rot}}}}, \tag{1.9}$$

being I_{38} the star moment of inertia in units of 10^{38} kg m^2 and d_{kpc} the distance of the source in kiloparsecs.

Chapter 2

The LIGO and Virgo experiments

2.1 Gravitational wave interferometric detectors

LIGO (Hanford H1 and Livingston L1) and Virgo detectors are the two main gravitational wave observatories that successfully concluded their second observational run of the Advanced detector era, on August 25th 2017. Based on a modified Michelson interferometer respectively with 4 km and 3 km long arms, these detectors can measure space-time deformations induced by passing gravitational waves by monitoring the relative variation of the light optical path in the two arms. The displacements that need to be measured are of the order of 10^{-18} m.

In order to improve their sensitivity, the initial LIGO and Virgo interferometers have been upgraded from 2010 to 2014. The main upgrades include a signal recycling mirror added at the output "dark" port, an increase of the laser power and of the test masses and changes in the interferometer readout and control systems, allowing to reach a sensitivity in the second science run O2 of 3-10 times better than the initial detectors (depending on the frequency band), which corresponds to an increase of the volume of the observable universe of 30-1000 times.

The detector basic optical configuration is a power-recycled and signal-recycled Michelson interferometer with a Fabry-Perot resonant cavity in each arm, as shown in Figure 2.1. The pre-stabilized laser pumps the light into the detector input mode cleaner system, which defines the laser position and light mode, before passing it to the power recycling stage. The power recycling mirror increases the effective laser power, forming a resonant cavity between the Michelson and the laser source. After the power recycling mirror, the laser is equally split by the Beam Splitter (BS) which sends the light to each interferometer arm. The test masses distance and position are controlled in such a way to set the light inside each cavity in a resonant condition (this corresponds to an increase of a factor about 100 in the light optical path). The light is recombined once again at the beam splitter and eventually passes through the Signal Recycling Mirror (SRM). The SRM allows to improve the detector frequency response to specific range of astrophysical signals[1]. Finally the light goes into the Output Mode Cleaner and the final interference can be measured by the photo-detector system. For a detailed description of the interferometer design, materials and degrees of freedom choices, see [3, 26]; the status of the advanced LIGO detectors during the first observational run can be found in [62].

---

[1] In fact the SRM system has not been yet implemented in Virgo detector.

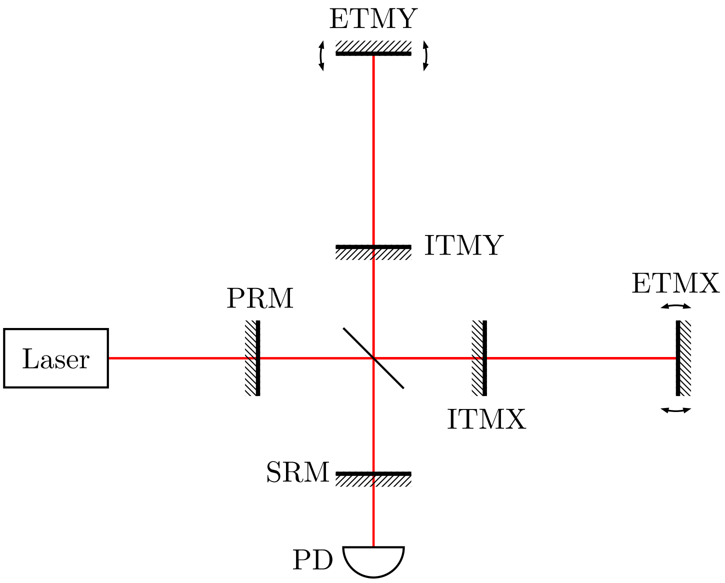

Figure 2.1. Simple optical configuration scheme of a power-recycled and signal-recycled Michelson interferometer with Fabry-Perot resonant cavities: the laser beam is split equally by the beam splitter and the two beams recombine each other to the photo-diode (PD). The resonance between the Power-recycling mirror (PRM) and the rest of the interferometer, increases the power laser. Two Fabry-Perot cavities at each arm are created between the input test masses (ITMX and ITMY) and the relative End Test masses (ETMX and ETMY). Eventually, an extra mirror (SRM) is added as a signal recycling at the output port.

Currently the LIGO interferometers have been running at the mid-design sensitivity (corresponding to a binary neutron star inspiral range of $60 - 100$ Mpc) while Virgo was at its early design sensitivity ($25 - 30$ Mpc) as shown in Figure 2.2. The BNS inspiral range is defined as the volume- and orientation-averaged distance at which a coalescence of a pair of $1.4M_{\odot}$ neutron stars gives a matched filter signal-to-noise ratio of 8 in a single detector as defined in [41].

2.2 Noise sources

The interferometer sensitivity is determined by different noise sources acting at different frequencies as discussed in [91, 1], see Fig. 2.3. At frequencies higher than about 300 Hz the main contribution to the noise level is given by the shot noise. The shot noise is related to the quantum nature of the laser photons and in particular to the statistical fluctuations in detected photon arrival rate. At intermediate frequency, say between 40 Hz and 300 Hz, thermal noise is the main noise source, associated to the thermal fluctuations of the various mirror components and, in particular, the mirror suspension wires and internal modes of the mirror coatings. Frequencies below about 40 Hz are dominated by the environmental seismic noise, of natural (wind,

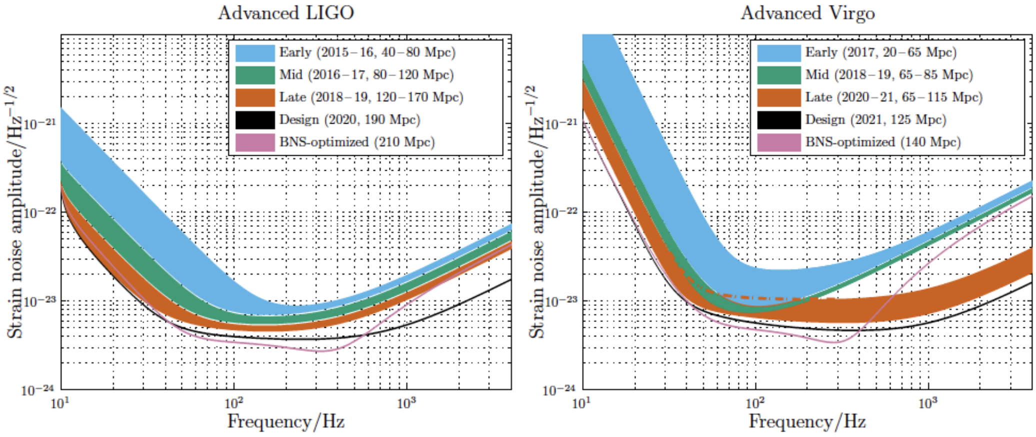

Figure 2.2. LIGO and Virgo design sensitivities as a function of the frequency.

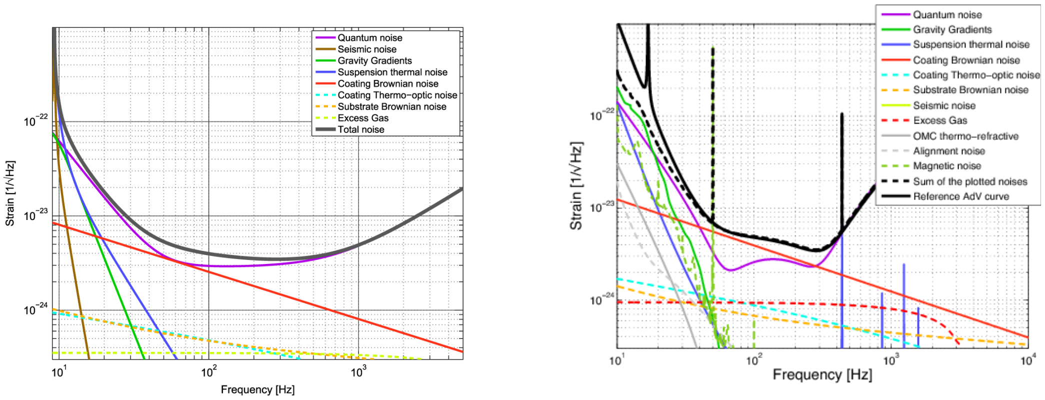

(a) Advanced LIGO at 190 Mpc BNS range. **(b)** Advanced Virgo at 125 Mpc BNS range.

Figure 2.3. Principal noise sources for Advanced LIGO and Advanced Virgo.

sea, etc.) or anthropogenic origin. Below about 10 Hz the sensitivity of the detectors rapidly worsens due to the fundamental seismic noise of the ground (the so-called "seismic wall"). To reduce these and other sources of noise, all the interferometer components are mounted in a ultra-high vacuum system on seismically isolated platforms.

2.3 The Data acquisition

The goal of the Data Acquisition System is to provide different data streams for both long-term storage on disk or tapes and online investigations such as noise and data quality studies, as well as commissioning. Each interferometer produces a calibrated time-series data stream, known as $h(t)$, along with thousands of time-series from auxiliary channels, which monitor the behavior of the instrument and its environment. The auxiliary channels data include interferometer sensing and control, detector sub-systems and environmental-monitoring channels. Data is collected with sample rates ranging from 1 to 32.000 Hz, depending on the channel. For each channel data is reduced (decimation, compression, image processing, etc) for an immediate use by online processes. All the different data streams are stored on disk as *frame files* using a specific file format, called *gravitational wave experiment data format* (.gwf) [55].The $h(t)$ stream, which contains the reconstructed GW strain channel and data-quality flags and is the main channel for data analysis, is also stored in frame files. In figure 2.4 is reported the status of the main Virgo channel for the Observational run O2. The duty cycle in this run was $\sim 85\%$.

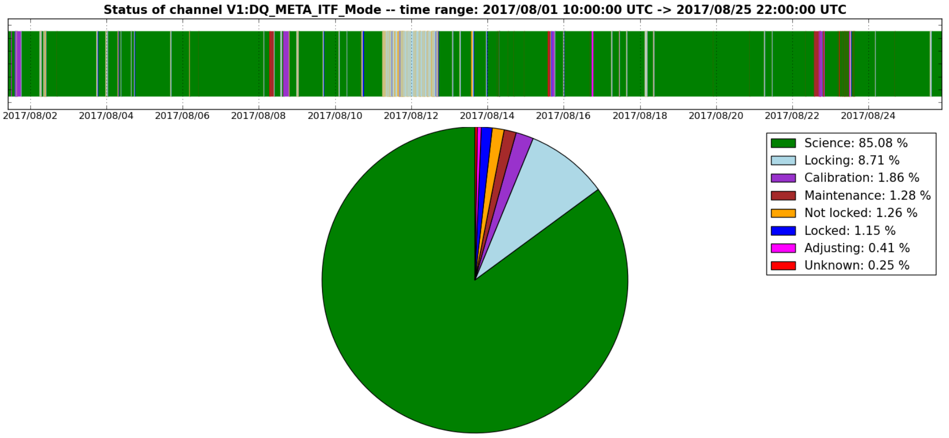

Figure 2.4. O2 duty cycle for Virgo detector. Data has been in working in stable condition the 85% of the time.

2.4 Detector Characterization

During data taking a lot of effort is done to characterize the detector behavior. Since these instruments are designed to be very sensitive to small space-time perturbations produced by a passing gravitational wave, they are at the same time sensitive to several disturbances not produced by a GW signal. This important task of studying the detector, and its noise characterization, is carried out by the Detector Characterization group (DetChar). The DetChar group covers every aspect of the data quality ranging from live monitoring of the detector's status to the production of event vetoes. DetChar groups works with the commissioning team[2] to find out any cause which affect the detector sensitivity and provides feedback to the data analysis groups and commissioning team.

Noise analyses shifts, using several monitoring and investigation tools, are carried out during runs by DetChar experts and volunteers, providing feed-back to the commissioning group. The tools developed for DetChar analysis checks data from the main channel, but also looks for noise clues in the auxiliary channels. The ensemble of environmental noise sensors, placed at critical points around the detector is called the Physical and Environmental Monitor (PEM) system as shown in figure 2.5. The PEM system includes seismometers, accelerometers, magnetometers, microphones and radio receivers, all those instruments meticulously monitor the interferometer behavior and its environment and are used to detect disturbances that can couple to the gravitational wave channel.

---

[2] before the scientific run, a commissioning run starts where multiple test on the interferometer sub-systems are performed

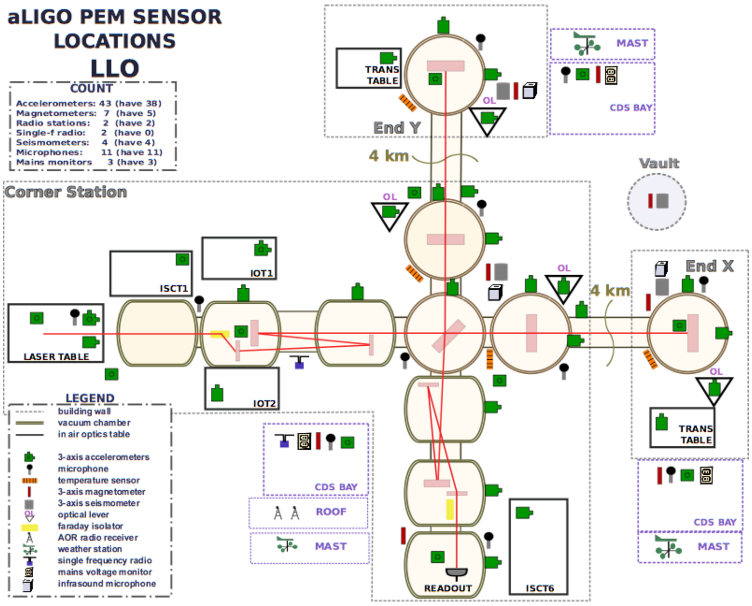
aLIGO PEM SENSOR LOCATIONS
LLO
COUNT
Accelerometers: 43 (have 38)
Magnetometers: 7 (have 5)
Radio stations: 2 (have 2)
Single-f radio: 2 (have 0)
Seismometers: 4 (have 4)
Microphones: 11 (have 11)
Mains monitors 3 (have 3)
Corner Station
TRANS TABLE
End Y
4 km
OL
MAST
CDS BAY
Vault
End X
4 km
ISCT1
IOT1
LASER TABLE
IOT2
TRANS TABLE
ROOF
READOUT
ISCT6
LEGEND
building wall
vacuum chamber
in air optics table
3-axis accelerometers
microphone
temperature sensor
3-axis magnetometer
3-axis seismometer
optical lever
faraday isolator
AOR radio receiver
weather station
single frequency radio
mains voltage monitor
infrasound microphone

Figure 2.5. The Physical and Environmental Monitor (PEM) system at L1 site.

The DetChar group also provide fundamental information to the data analysis search groups defining Data Quality flags. Basically DQ definitions tell search groups which data segment is validated as "science". Science segments correspond to time periods when the detector is locked and working in stable conditions. Data segments presenting huge noise disturbances, due to detector malfunctioning or very bad environmental conditions, are removed and labeled as non-science. The role of the DetChar group is crucial in particular when a GW is detected. Indeed, short-duration noise events in the time domain, called *glitches*, can mimic transients GW signals, while spectral noise lines in the strain-amplitude spectral density can be confused with CW signals. These noises have multiple origins: mechanical resonances, power harmonics, calibration injections, environmental mechanisms, electronics, magnetic fields and so on. For the first category of noise (glitches) which limits mainly Burst or CBC searches, a veto system which discards background events has been developed and many veto optimization tools generate search-specific rejection rules for transient searches. More information about the transient veto system can be found in [88]. For persistent signals time glitches are not a big problem, since the sensitivity of CW and stochastic searches is affected mainly by narrow-band noise features, like spectral lines. This aspect will be discussed in detail in the next section.

Chapter 3

Spectral noise investigations

3.1 Spectral noise hunting

One of the noise hunting tasks of the DetChar group, which impacts all the CW searches, is the identification and mitigation of the sources of the spectral lines present in the data. A line is a disturbance that affect CW searches mimicking a real gravitational wave signal or reducing the sensitivity at specific frequencies. Roughly speaking, there exist two main kind of spectral lines: stationary and non-stationary. The stationarity of a line is quantified by the time dependence of the amplitude and frequency. A stationary line has a constant (or slowly variable) frequency and is persistent in time. A proper stationary line is easy to catch up since, given its persistent nature, the line is present all over the run. There are some lines that simply disappear during a certain period re-appearing at later times. This can happen for example as a device is switched off and on. Wandering lines, unlike stationary ones, can move along the frequency band, sometimes following a periodicity or randomly. Lines showing patterns or periodicities are due to instrumental noise, such as those having a cycle of minutes or hours which can be connected to the temperature variations of a room or be caused by other external factors. Sometimes, when there is a correlation with one of the auxiliary channels, such as one of the PEM sensors, the line is clearly identified as an artifact and its astrophysical origin is discarded. Generally speaking the "shape" of a line in the spectrum is also a clue for its origin, very narrow lines are associated to calibration injections or if they are present in combs[1] those are often caused by digital devices clocks, while "bumps" are typically due non stationary sources. Lines associated with mechanical resonant modes of the mirrors or suspensions, like the violin modes, have a typical Lorentzian shape. Finally, electric devices such as air conditioning cooling fans, vacuum pumps, water pumps, resonant modes of optical benches or other interferometer benches, up to Wi-Fi signals can produce noise lines and need to be quickly identified and mitigated when possible. There are also lines introduced on purpose into the detector, for instance calibration lines and even simulated CW signals, the so-called *hardware injections*, useful for testing the analysis pipelines.

---

[1] a comb is formed by a group of lines separated by a fixed frequency interval. A comb of lines is a peculiar case of lines harmonics

3.2 NoEMi: Noise frequency Event Miner

The detector characterization team uses several investigation and monitoring tools to identify spectral lines. The different tools have been developed by several people in the collaboration. Those tools typically identify lines looking for excess of power in the power spectrum, spectrograms or their variation (like peakmaps in the case of NoEMi) and compute coherences between the main and auxiliary channels in order to help the line source identification. One tool called NoEMi (Noise frequency Event Miner) [24], developed by the Rome Virgo group, has been used in previous Virgo runs VSR2/VSR4, as well as in both LIGO detectors during O1 (in L1 and H1), and LIGO and Virgo detectors in O2. Moreover, it has been routinely used also in the various commissioning and engineering runs. Moreover, NoEMi has been adapted for CW search purposes other than the line identification and has been used for the creation of the SFDB files, as will be mentioned in section 5.1. NoEMi has been developed to analyze data running daily on the $h(t)$ channel and a set of auxiliary channels. It identifies lines and finds coincidences between the $h(t)$ channel and the list of auxiliary ones. Furthermore a line tracking algorithm follows the lines over time, catching in particular wandering lines. The daily results, including the time frequency plots (see Figures 3.1,3.2) of all the monitored channels and the list of found lines, have been incorporated to VIM (Virgo Interface Monitoring) [45],which is the Virgo pages providing archived and online status about each Virgo detector's sub-system, about online processing and about online detchar analyses. A dedicated section in VIM shows the line tracking of the lines from the beginning of the run (as an example see Fig 7.12). Noemi infrastructure lies on a MySQL database where all the time-frequency events and lines are stored and can be used by the line tracking or for offline analysis. A detailed description of NoEMi basics can be found in [24].

3.3 Spectral lines and couplings

All the identified lines are registered and removed during the search. The main sources and coupling mechanisms for spectral lines will be briefly discussed in this section. Broadly speaking, there exists different line categories that can be divided in two main families: intrinsic lines and noise lines. Intrinsic lines are well known lines produced by the main components of the interferometers. Among those lines there are violin modes (with their harmonics), all the mechanical resonances, calibration and control lines and the main power line (60 Hz for LIGO and 50 Hz for Virgo) and its harmonics. Is not possible to eliminate those lines, thus it is necessary to exclude from the analysis the most affected frequency regions[2]. Generic noise lines have different possible origins like seismic, or magnetic, or digital devices, or sidebands of some intrinsic line. Some lines are produced as a consequence of a coupling with vibration noise. For example, if the vibration of lenses is periodic, the scattered light can produce a noise line visible in the dark fringe channel. Another important coupling which produces lines is the angular jitter noise, which adds to the beam when the interferometer optics vibrate. Another type of noise coupling generating spectral noise, is given by the magnetic noise. In particular low frequency EM fields couple directly into the detector bandwidth, while higher frequencies are disturbed by radio-frequency EM fields. Also actuators used to control the mirror positions, which are made of magnets, can be disturbed by magnetic field gradients, generating an unusual mirror displacement. Digital noise lines is another family of spectral noise. Those lines are very narrow (less than 1 mHz of width) and are multiples of fundamental frequencies. Usually they are originated by digital systems in the detector such as some lines generated by air conditioning cooling fans or internal clocks of surrounding devices. Finally a few words about the sidebands lines, which are often visible around intrinsic lines. They are probably due to some non-linear coupling of the line with interferometer components. Sidebands are visible around strong and persistent lines such as calibration ones.

---

[2] sometimes broad frequency bands must be excluded from the analysis, since forests of lines having the same source pollute large frequency bands as in the case of violin modes.

Line monitoring requires a constant and patient work. Several tests are done during commissioning runs, including massive switch off of devices, moving of sensors, and also animal hunting from time to time[3]. Line hunting is a difficult task, especially when lines are not stationary, like combs which may disappear or get smaller without apparent reason, or due to a sudden growth of the noise level which can hide previously present lines, or due to the establishment of some unknown coupling mechanism and so on.

3.3.1 Lines in O1 and O2 in LIGO

Lines status in O1 was not one of the best. The low frequency band, up to 130 Hz, was dominated by several combs among which the family of 1Hz combs (tracked down to timing cards) with 0.5 Hz off-set, polluted the spectrum of both L1 and H1. Higher frequencies of H1 were dominated by 16-Hz harmonics, and sporadic odd 8-Hz harmonics, while a mix of 22.7 Hz and 25.6 Hz harmonics was found in L1. DetChar investigation found that the H1 16 Hz comb was due to Output Mode Cleaner length dither; while in L1 22.7/25.6-Hz lines was also due to Output Mode Cleaner length dither. Reducing dither amplitude reduces the comb.

The line status of O2 in LIGO detectors is still a work in progress, but likely the same features of O1 data will be found again in O2.

3.3.2 Lines around GW170814 in Virgo

In the frequency range of the gravitational wave event GW170814 there are several strong lines, some of which have a known origin. Most of these lines are persistent across the full day around the event (and in general across the full O2 run) and have a constant frequency. There is one slightly wandering line (a doublet in fact), around 80 Hz, that is very weak before the event and becomes stronger around 1 p.m. GMT, about 2 hours and half after the event, see Figure 3.1. Clearly it has nothing to do with the event.

---

[3] e.g. ravens

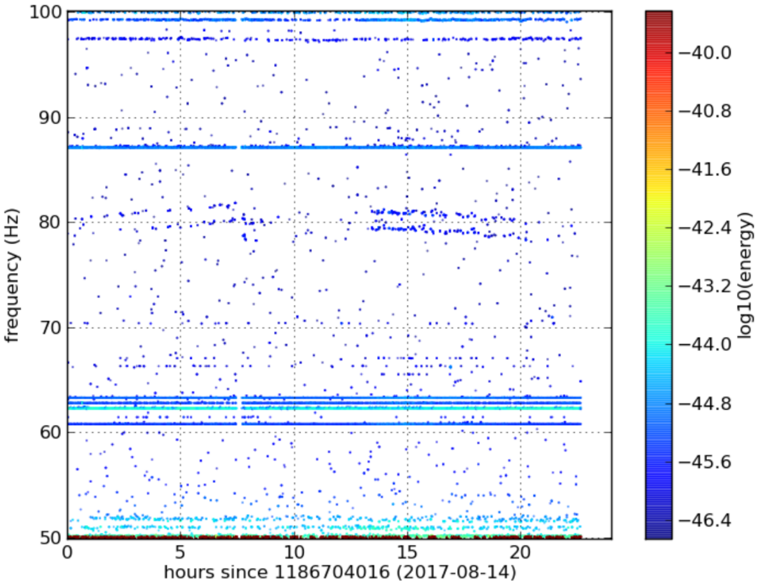

Figure 3.1. Time-frequency plot taken from the daily summary page of NoEMi of the main strain Virgo channel and around the frequencies of GW170814 event.

3.3.3 Lines around GW170817 in Virgo

The situation is similar as for the other event. In fact the doublet at 80Hz seems to rise up at nearly the same time, 20 minutes after the event in this case, see figure 3.2. This line appeared for the first time in Aug. 12th and show-up intermittently

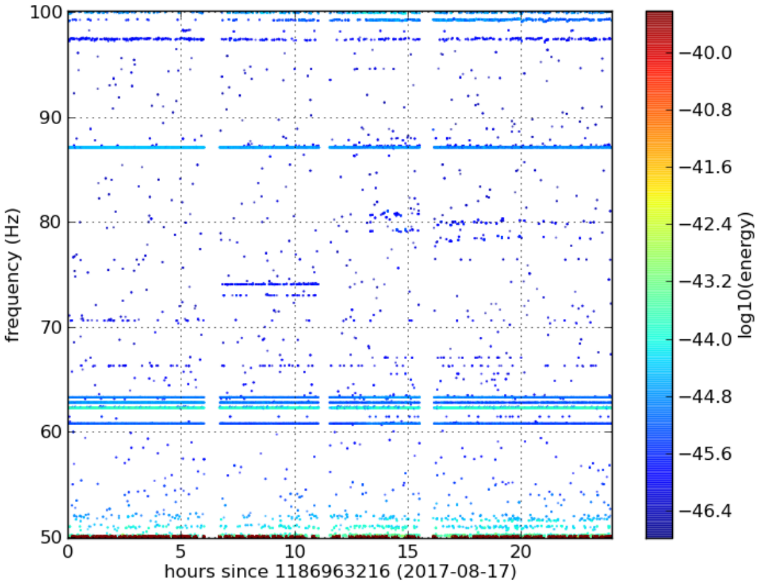

Figure 3.2. Time-frequency plot taken from the daily summary page of NoEMi of the main strain Virgo channel and around the frequencies of GW170817 event.

in NoeMi until the end of the run, see next figure 3.3 for e.g. Aug. 21th.

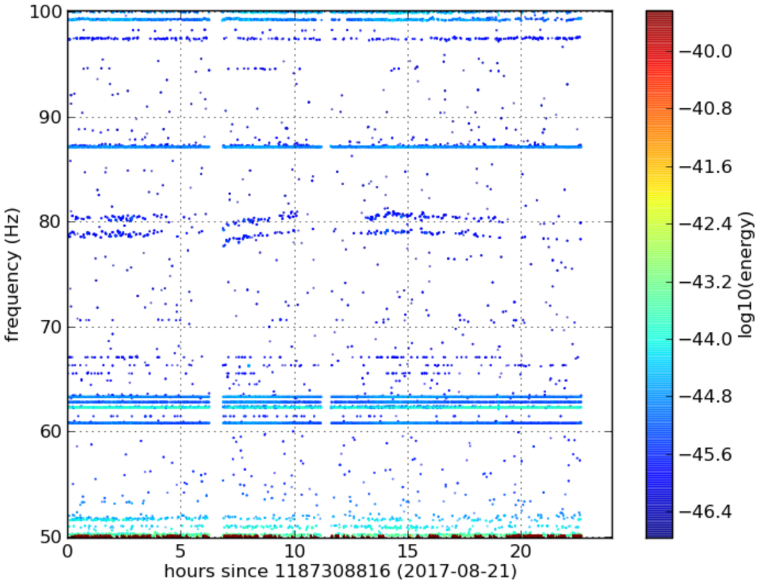

Figure 3.3. Time-frequency plot taken from the daily summary page of NoEMi of the main strain Virgo channel. The doublet around 80 Hz reappeared few days after the last events with the same features.

Part II

Data analysis for CW

"You don't have to learn lots and lots and lots of facts; you just learn a few key things, and if you really got hold on them, then you can apply and build and develop from those."

An Interview with Jocelyn Bell-Burnell by K.M. Weatherall (1995)

Chapter 4

Continuous GW searches

4.1 The signal model

The expected strain amplitude at the detector site, for a quadrupolar GW signal emitted by a non-axisymmetric neutron star steadily spinning around one of its principal axis, is [29]:

$$h(t) = H_0 \left(H_+ A^+(t) + H_\times A^\times(t) \right) e^{j(\omega(t)t + \Phi_0)} \tag{4.1}$$

where taking the real part is understood and $\omega(t)$ is the time dependent angular frequency while Φ_0 is an initial phase. The emitted signal frequency f_0 at a given time t_0, is related to the star rotational frequency by $f_0 = \frac{\omega(t_0)}{2\pi} = 2f_{rot}(t_0)$. The complex amplitudes H_+ and $H_\times$ are given respectively by:

$$H_+ = \frac{\cos 2\psi - j\eta \sin 2\psi}{\sqrt{1+\eta^2}} \tag{4.2}$$

$$H_\times = \frac{\sin 2\psi + j\eta \cos 2\psi}{\sqrt{1+\eta^2}} \tag{4.3}$$

where ψ is the polarization angle, defined as the counter-clockwise angle between the polarization ellipse semi-major axis and the source celestial parallel. The parameter η, which is given by the ratio of the polarization ellipse semi-minor to semi-major axis, indicates the degree of polarization of the GW, assuming values in the range $[-1, 1]$ ($\eta = 0$ for a linearly polarized wave, $\eta = \pm 1$ for a circularly polarized wave). The time dependent functions $A^+(t)$, $A^\times(t)$, are the detector response to a passing GW and depend on the source position, the detector location and its orientation on the Earth as:

$$A^+(t) = a_0 + a_{1c}\cos(\Omega_\oplus t) + a_{1s}\sin(\Omega_\oplus t) + a_{2c}\cos(2\Omega_\oplus t) + a_{2s}\sin(2\Omega_\oplus t) \tag{4.4}$$

$$A^\times(t) = b_{1c}\cos(\Omega_\oplus t) + b_{1s}\sin(\Omega_\oplus t) + b_{2c}\cos(2\Omega_\oplus t) + b_{2s}\sin(2\Omega_\oplus t) \tag{4.5}$$

where the coefficients are explicitly dependent on the source declination, the detector latitude and azimuth. The detector response produce a splitting of the signal power among the five angular frequencies ω_0, $\omega_0 \pm \Omega_\oplus$ and $\omega_0 \pm 2\Omega_\oplus$, where $\Omega_\oplus$ is the Earth sidereal angular frequency.

The strain amplitude in Eq. 4.1, is equivalent to a more standard notation for $h(t)$ (see [51]), where the gravitational wave amplitude h_0 can be obtained from H_0 using the following relations:

$$H_0 = h_0 \sqrt{\frac{1 + 6\cos^2\iota + \cos^4\iota}{4}} \tag{4.6}$$

$$\eta = \frac{2\cos\iota}{1+\cos^2\iota} \tag{4.7}$$

where ι is the inclination angle of the star's rotation axis with respect to the line of sight.

The angular frequency in Eq. 4.1 is a function of time and depends on both the intrinsic rotational frequency and the frequency derivatives of the neutron star (spin-down factors). Due to the Doppler effect, the signal frequency at the detector $f(t)$ is related to the emitted frequency f_0 by the well-known non-relativistic approximation

$$f(t) = \frac{1}{2\pi}\frac{d\Phi(t)}{dt} = f_0(t)\left(1 + \frac{\vec{v}\cdot\widehat{n}}{c}\right) \tag{4.8}$$

where $\vec{v} = \vec{v}_{orb} + \vec{v}_{rot}$ is the detector velocity in the Solar System Barycenter (SSB), sum of the Earth's orbital and rotational velocity, while $\widehat{n}(\alpha, \delta)$ is the versor pointing at the source position in equatorial coordinates.

Due to the rotational energy loss of the star, consequent to the emission of gravitational radiation (and possibly also electromagnetic radiation), the emitted signal frequency slowly decreases with time. This spin-down effect can be described by a Taylor series expansion:

$$f_0(t) = f_0 + \dot{f}_0(t - t_0) + \frac{\ddot{f}_0}{2}(t - t_0)^2 + \ldots \tag{4.9}$$

where $[\dot{f}_0, \ddot{f}_0, \ldots]$ are the so called spin-down parameters. There are also other smaller relativistic effects, namely the Einstein delay and the Shapiro delay, which may play a role for long coherence times.

4.2 Type of CW searches

As previously discussed in Chapter 1, neutron stars both isolated or in binary systems could emit a long-lived quasi-monochromatic signal called continuous waves. Several searches for those systems have been carried out during the last observational runs of the LIGO and Virgo detectors.

Depending on the information available about the source parameters (source position, signal frequency and its time derivatives) different search methods have been developed. Broadly speaking, CW searches can be divided in four main categories: *targeted* in the case of signals emitted by known pulsars (i.e. with rotational parameters and sky position very well known); *narrow-band* searches, in the case of stars with slightly uncertain frequency and spin-down; *directed* for NS at specific known locations but with unknown frequency and spin-down (e.g. searches pointing to the Galactic Center or to supernova remnants); blind *all-sky* searches for neutron stars (isolated or in binary systems) with no electromagnetic counterpart. Currently other CW search methods are being developed to look for transients CW signals (mainly due to NS r-modes emissions or NS glitches).

The data analysis techniques of the previously mentioned searches would be characterized by the search sensitivity, its robustness towards instrumental noise and uncertainties and by its total computational cost.

For instance, coherent methods, based on matched filtering, can be used to gain signal-to-noise ratio in targeted searches, which are characterized by a good sensitivity and a low computational cost. On the other hand, when less or no information about the source is available, like in the case of all-sky searches, hierarchical methods have been developed in order to explore a large volume of the source parameter space. As it will be explained in the next section, this type of analysis is computationally bounded.

In between those two extreme cases in terms of sensitivity and computational cost are placed the narrow-band and the directed searches.

We will briefly review the main features and observational results obtained so far for each of the mentioned searches, while in the next section we will describe in more detail some concept used in hierarchical (or incoherent searches) which will be used in the developed pipeline described in Chapter 6. A recent review of the latest observational results and methods can be found in [73] and [56].

4.2.1 Targeted searches and narrow-band searches

Matched filtering is a signal processing linear filter which optimally maximizes the signal-to-noise ratio (SNR) in presence of noise. This is obtained by cross-correlating the data with signal templates. The template is built from the known source parameters (position and rotational parameters), which must be known with high accuracy. This type of search is often referred as coherent search, since it is possible to apply the Doppler and spin-down corrections (plus other minor relativistic effects) over long times. Although this is a very sensitive method, its computational cost explodes when a big number of parameters is investigated, hence it is feasible only for a very small range of parameter values (as in the case of narrow-band searches).

The 90% confidence level sensitivity of this type of search scales with the observation time T_{obs} and detector power spectral density at the frequency f:

$$h_{0_{min}}(f) \approx 10\sqrt{\frac{S_n(f)}{T_{obs}}} \tag{4.10}$$

the numeric coefficient corresponds to a false alarm probability of 1%. The latest results for those type of searches can be found in [90] and [15].

4.2.2 Directed searches

In directed searches the only parameter we assume as known is the sky position of an interesting astrophysical object or a specific region in the sky. For this searches this parameter can be assumed as well known or at least known with a very small uncertainty. It is possible to extend this type of search for a wider sky region simply repeating the analysis for a closer sky position, although in that case the computational time will be too high. Those type of searches can be performed using coherent methods only if the range of frequency and spin-down to be searched for is relatively small.

Potential sources of those searches are central compact objects found in supernova remnants or the so-called "unidentified" Fermi-LAT sources, most of which are plausibly neutron stars. Other potential sources for directed searches are well localized region in the sky like nuclear globular clusters and the Galactic center region.

Few interesting directed searches have been performed using different pipelines, in particular the last Galactic Center search used S5 LIGO data [2]. Other targets of directed searches for isolated neutron stars are: the one pointing to the supernova remnant Cas A [97] and other young supernova remnants [4], the Orion Spur [6] and the Globular cluster NGC 6544 [20].

4.2.3 All-sky searches

While targeted and narrow-band searches can be performed using optimal methods, based on matched filtering, this is not possible in directed searches and especially in blind all-sky searches, where the volume of the parameter space to be investigated is huge, making a full coherent search unfeasible. To face this problem, *hierarchical methods*, based on the alternation of coherent and incoherent steps, have been developed. This allows to drastically reduce the computational load of the analysis at the cost of a sensitivity loss. It should be mentioned that, although the sensitivity of those searches is lower (compared to the case of full coherent searches), this is a more robust method against unpredictable signal phase variations during the observation time.

In typical hierarchical searches, the full data set is divided in several shorter segments which are properly processed and then incoherently combined (semi-coherent search). On this combined data potentially interesting candidates are selected at this stage and are eventually followed up if they are interesting ones. As widely discussed in [93],[57], different methods for blind all-sky searches have been developed for this purpose.

The sensitivity of a blind all-sky search depends on several search setup parameters as the choice of thresholds for candidate selection and the set of the parameter space (for further details see Sections 6.6).

4.2.4 Searches for CW in binary systems

Most of the observed millisecond pulsars are in a binary system. Accreting neutron stars in low-mass x-ray binaries, like Scorpius X-1 or XTE J1751-305, see e.g. [64], are typical CW search targets. As briefly mentioned in Chapter 1, for such kind of sources the gravitational wave signal is complicated by the intrinsic Doppler effect, and depends on the binary system Keplerian parameters and eventually by irregularities in the rotation rate, driven by the matter accretion rate. Significant effort is being done in order to develop pipelines suitable for such kind of complicated signals. The most sensitive searches up to date have been recently conducted on LIGO O1 data [22].

4.3 The FrequencyHough transform

The generic Hough transform was born as a data processing techniques for robust pattern identification in digital images. In CW searches it is used to map points in the time/frequency plane which follow the pattern expected from a signal into the signal parameter space.

In current CW searches different "flavors" of the Hough transform exist. For instance, in the version of Hough transform used in the Einstein@Home hierarchical search [89], for each fixed value of the frequency and frequency derivative(s) a map between the time and frequency plane and the source position is built.

In the FrequencyHough implementation instead [5, 30], the map is done between the time-frequency plane and the source frequency and spin-down plane for any fixed sky position.

This a linear mapping between the detector time/source Doppler corrected frequency plane into the source intrinsic frequency/spin-down plane. Indeed we can write the Doppler corrected frequency of a signal at the detector as $f = f_0 + \dot{f}_0(t - t_0)$ which can be inverted as:

$$\dot{f}_0 = \frac{f_0}{(t-t_0)} + \frac{f}{(t-t_0)} \tag{4.11}$$

The FrequencyHough map is constructed by a Doppler corrected time-frequency peak-map (see Sec. 6.2), for which each point in the input plane $(t - t_0, f)$ is transformed into a straight line in the $(f_0, \dot{f}_0)$ Hough plane, with slope $-\frac{1}{(t-t_0)}$. Due to the discretization of the frequency in the input plane[1], each peak will be transformed into a stripe rather than a single line. Calling δf_H the frequency bin of the input plane, the spin-down values will range between :

$$-\frac{f_0}{t-t_0} + \frac{f - \delta f_H/2}{t-t_0} < \dot{f}_0 < -\frac{f_0}{t-t_0} + \frac{f + \delta f_H/2}{t-t_0} \tag{4.12}$$

In each bin of the frequency/spin-down plane touched by a stripe the number count is increased by one. In Chapter 6, we will describe a new directed search pipeline which relies on the robustness provided by this semi-coherent method.

---

[1] As will be clear in following sections, the input of the Hough map i.e. the peak-map is built looking at the maximum values in the equalized spectrum, which is built from a finite chunk of data which introduce a discretization in frequency.

Chapter 5

The Band Sampled Data collection

5.1 The Short FFT Database

Up to now all the CW searches performed in the Rome group rely on a collection of FFTs (called Short FFT Database - SFDB) [28]. Each FFT in the SFDB is built from chunks of calibrated data of a given fixed duration. The criteria used for the choice of the FFT length is related to the Doppler modulation, in particular the length should be such to contain all the power of an hypothetical Doppler modulated signal within a single frequency bin. In particular, the configuration used in the last CW searches [90],[5], consists of four SFDB databases which parameters are listed in Table 5.1. Each database covers up to a certain maximum frequency and for each band the correspondent FFT length is shown on the 3rd column. The sampling time used for each database is given by $\frac{1}{2f_{max}}$ where f_{max} is the maximum frequency covered in the database. The SFDB files are created from NoEMi [24], which has been used to speed up and automatize the production of those files.

Table 5.1. SFDB database configuration parameters.

Frequency band (Hz)	Sampling time (s)	FFT duration (s)
0-128	3.9×10^{-3}	8192
0-512	9.8×10^{-4}	4096
0-1024	4.9×10^{-4}	2048
0-2048	2.4×10^{-4}	1024

This configuration has been chosen, as discussed in [28], as a trade off between the computational load and the sensitivity of a generic blind all-sky search. Although this can be a good choice for that particular case, for analyses like the narrow-band, directed or in targeted searches this is not the best solution. For instance, in targeted searches, a coherent analysis of the full data set[1] can be done, thus the choice in Table 5.1 would be not optimal. Indeed in this case the data in the SFDB must be properly combined before applying barycentric corrections in order to use the signal long coherence time, complicating the analysis. In semi-coherent searches (like all-sky and directed searches), the fixed length of the FFTs generally does not correspond to an optimal length, on the basis of the expected signal properties. This affects also the follow-up of candidates in all-sky searches, in which the feasible number of follow-up is strongly limited by the current SFDB architecture (as will be clear in section 6.5).

---

[1] it means that the maximum FFT length we can use is the total observational time

In this work we want to present a solution which will replace the current SFDB database. This is a new and flexible data framework, which overcomes some of the limits of the current SFDB architecture, allowing to simplify analysis pipelines, making them more sensitive, and significantly reducing their computational load. This means an increase of the search sensitivity at fixed computational cost. As it will be clear in the following, the key point of this new framework is that very efficient Doppler and spin-down corrections can be done on the data, and in particular the corrected time series can be produced "on-the-fly", depending on the analysis being done.

5.2 The method

The new data framework which is called *Band Sampled Data* collection (BSD) [78], consists in a set of band-limited time series, down-sampled and partially cleaned from disturbances. Each time series is contained in a file (called BSD file) covering a frequency band of 10 Hz and spanning one month of data. The data contained in the BSD files are in the form of *reduced-analytic signals*, which in mathematics and signal processing, means it is a complex-valued time series with no negative frequency component [42, 92]. The differences between the classical analytic signal and its correspondent reduced-analytic form, will be clarified in Sec. 5.3.1. The sampling frequency of a reduced-analytic signal can be as small as 10 Hz for a 10 Hz band. For semi-coherent searches, the time duration of the data chunks to be incoherently combined can be chosen adaptively for each frequency band, see Fig.5.1, rather than being fixed. Barycentric and spin-down corrections are applied by an heterodyne technique, consisting in multiplying the data by a phase shift factor, as will be described in detail in section 5.4. The entire procedure of BSD production is computationally cheap and fast. As an example, the total disk usage for the production of a full set of BSD files, covering 4 months, 1024 Hertz and 2 antennas, is about 260 GB, while the total creation time is less than 1 day on an old CPU E5410 @2.33GHz. Within this new framework the data handling is very simple, easily allowing to use the data also for searches of other gravitational wave signals, like short transients. In fact, different file *configurations* can be chosen, depending on the specific analysis one wants to do. For instance, for all-sky or directed searches, which are based on a semi-coherent approach, a suitable configuration could consist of a set of files covering a band of, say, 10 Hz and 1 months of data. For targeted or narrow-band searches, on the other hand, for which a full-coherent analysis is done over a very small frequency band, a better choice would be building the BSD file over, e.g., 1 Hz and covering the full observation time of the data. In the case of searches for long transients signals, characterized by a very strong frequency

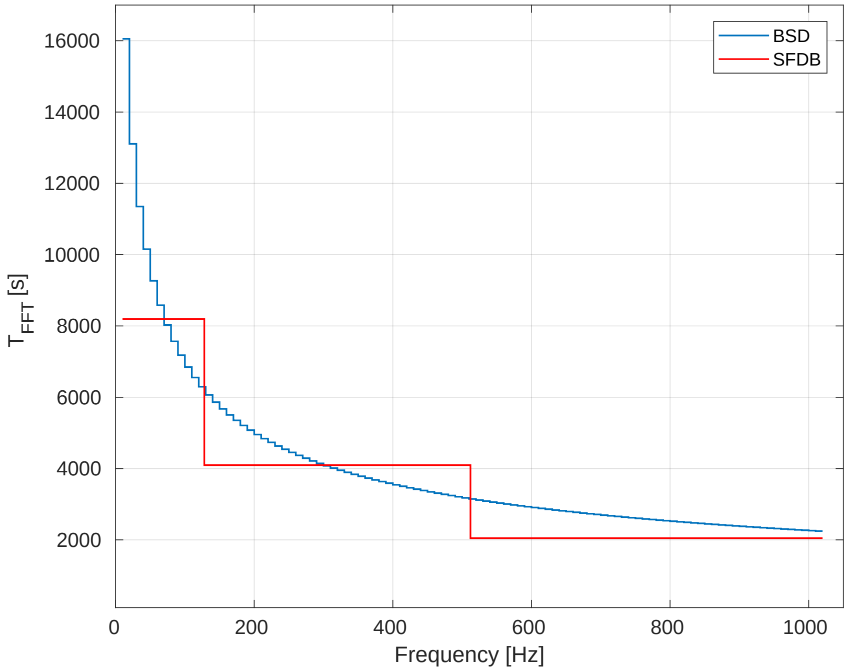

Figure 5.1. Comparison between the FFTs duration used in the SFDB architecture (red) and the suggested FFTs duration in BSD files (blue). The duration of FFTs is significantly enhanced especially at lower frequencies with a maximum enhancement factor of ~ 2 at the lowest frequency band.

variation in time, a reasonable choice could be building files which cover hundreds of Hertz in frequency and a few minutes, or even seconds, in time.

In order to allow a simple handling and processing of the data for the different types of analysis, several MATLAB functions have been developed as reported in Appendix B. The standard BSD file covers a band of 10 Hz and 1 month of data. Starting from this setting it is possible to extract a sub-band which covers more than 1 month of data or join more frequency bands for a shorter time span as shown in Figure 5.2. Making a comparison with the SFDB architecture (Table 5.1), the BSD collection can be seen as a database made up of a multitude of sub-databases (the BSD files) each with a suggested FFT duration per each 10 Hz frequency band as shown in Figure 5.1.

5.3 BSD creation

In this section we will focus on the practical construction of the new BSD database. Starting from the collection of FFTs (SFDB), the range of frequency between 10 and 1024 Hz is split in bands of given width Δf_{BSD}. For each selected band of each FFT the following steps are applied, see Fig. 5.3:

- compute the inverse Fourier transform and subsample to the inverse of the band width (e.g. with a sampling time of $\frac{1}{\Delta f_{BSD}}$ seconds);

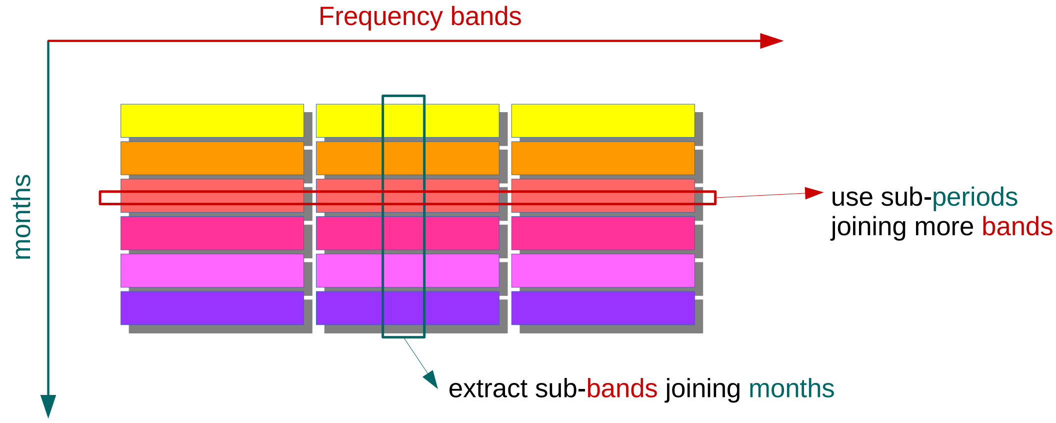

Figure 5.2. The Band Sample Data collection as a database of sub-databases. Data handling functions allows a smart use of the data in a very efficient way.

- creation of the *reduced-analytic signal* (see 5.3.1);
- remove the first and the last quarter of the time domain series, in order to avoid redundancies due to the overlapping in time (by half) of the FFTs[2].
- store this piece of data stream into the BSD file (buffer)

These operations are repeated for all the FFTs contained in the SFDB file and the whole process is iterated for all the frequency bands until the entire detector band is covered. The number of SFDB files to be used for the creation of a single BSD clearly depends on the BSD time span; for the standard BSD configuration we have chosen 1 month of data. More details about the BSD preparation are given in Sec. 5.3.1 and 5.3.2.

In order to reduce the Input/Output bottleneck when the FFTs in the SFDB are accessed for reading, the procedure works on several bands simultaneously (generally up to 10), depending on the RAM available.

Processed data is stored in a versatile format, called *gd*, implemented in the MATLAB-based software *Snag*[3]. A BSD file contains the data stored in the gd format, plus extra informations about the data, stored in a structure called *cont*. This data auxiliary structure contains among all information, the starting time of the BSD (in MJD - Mean Julian Date), defined as the time of the first sample of the gd; the initial frequency of the band; the band width covered by the file; the velocity and the position (in units of c) of the detector in the Solar-System-Barycenter frame and the reference time of those values; the detector data structure; the run name; the calibration version of the used data; and other minor information that can be found in appendix A.

---

[2] FFTs are interlaced by half in SFDBs

[3] Snag website: http://grwavsf.roma1.infn.it/snag/default.htm

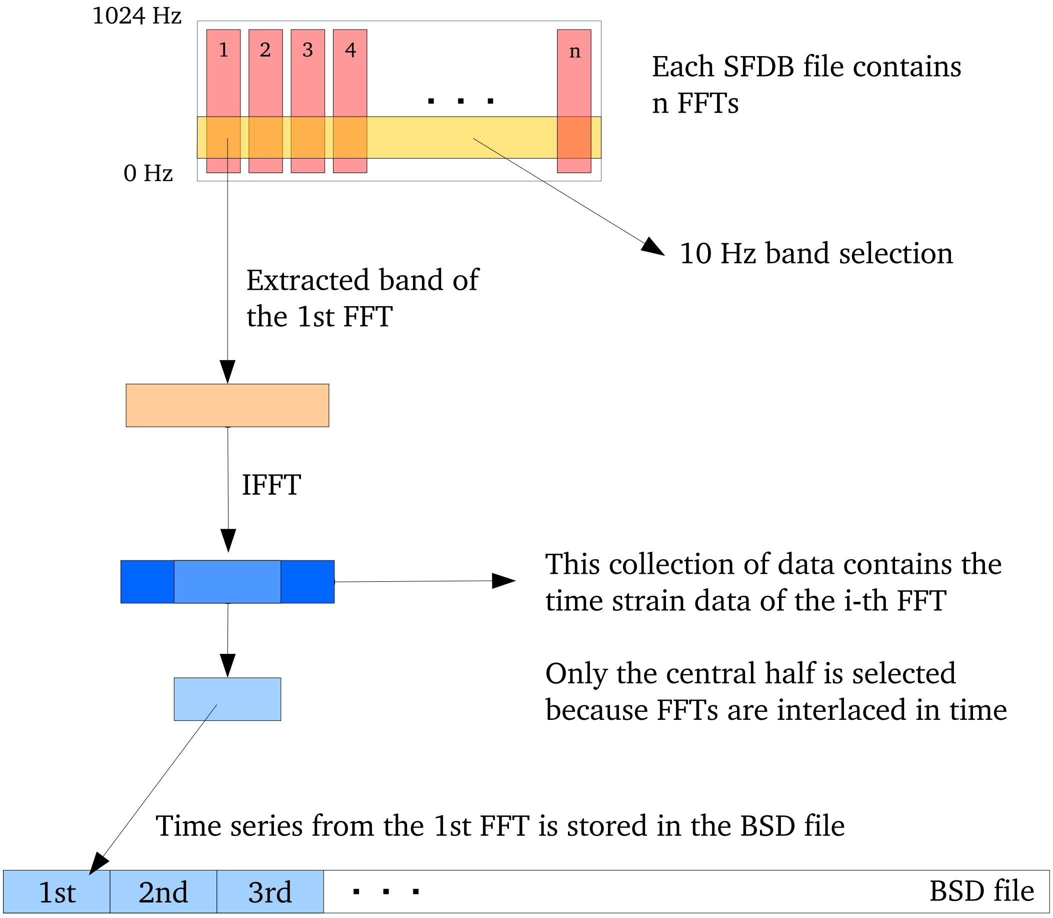
1024 Hz
0 Hz
1
2
3
4
n
. . .
Each SFDB file contains n FFTs
10 Hz band selection
Extracted band of the 1st FFT
IFFT
This collection of data contains the time strain data of the i-th FFT
Only the central half is selected because FFTs are interlaced in time
Time series from the 1st FFT is stored in the BSD file
1st
2nd
3rd
. . .
BSD file

Figure 5.3. BSD preparation scheme. BSD files are created from the SFDB files which contain a number n of FFTs (pink blocks). For each frequency band of, e.g., $\Delta f_{BSD} = 10$ Hz (yellow block) extracted from a FFT (orange), data is inverse Fourier transformed (blue + light blue block), and a central part is selected (light blue) and stored in the BSD file.

5.3.1 The analytic signal and its reduced form

In this section we discuss in more detail the type of data stored in the time series of the BSD. The data consists in a complex time series, sampled at the inverse of the bandwidth. The data we actually store in the BSD goes under the form of a slightly different version of the classical analytic signal, but is still a complex-valued time series with no negative frequency components [42].

Generally speaking, in an analytic signal the real and imaginary parts are real-valued functions related to each other by the Hilbert transform. In particular, given a real valued function its analytic representation can be built adding, as its imaginary part, the Hilbert transform of the initial function. In formulas, if $g(t)$ is a real valued function of t, its analytic representation is given by:

$$A(t) = g(t) + i\mathcal{H}[g(t)] \tag{5.1}$$

where $\mathcal{H}$ is the Hilbert transform operator.

Since the Fourier and the Hilbert transform are related by $\mathcal{F}\{\mathcal{H}[g(t)]\}(f) = (-i\text{sign}(f)) \cdot \mathcal{F}\{g(t)\}(f)$ the Fourier transform of an analytic signal will be given by:

$$\mathcal{F}\{A\}(f) = \begin{cases} X(0) & f = 0, \\ 2X(f) & f > 0, \\ 0 & f < 0. \end{cases} \tag{5.2}$$

where $X(f) = \mathcal{F}\{g(t)\}(f)$ is the Fourier transform of the real-valued function $F(t)$. From the Hermitian symmetry of the Fourier transform, in the analytic representation of a signal, the negative frequency components of the Fourier transform can be discarded, with no loss of information.

From the point of view of signal construction, in a standard analytic signal the sampling frequency is equal to that of the original real valued signal, i.e. at least two times the maximum frequency of the band, as required by the Nyquist theorem. In fact, our data are sampled exactly at the maximum frequency of the band, after shifting it to 0 Hz, e.g. at 10 Hz, if the data covers a band of 10 Hz, see Fig. 5.4. Such signal is called (in this context) *reduced-analytic*, because the sampling frequency is half the one used for analytic signals. This is a common technique used in signal processing which goes under the name of complex envelope or complex baseband. However there exist a perfect equivalence between the analytic signal and the reduced-analytic signal: indeed the reduced-analytic signal can be obtained taking only the odd time samples of an analytic signal. By using appropriate normalization factors a reduced-analytic signal with the following properties can be built:

- the amplitude (in time) of the complex reduced-analytic signal is half as for the starting real data.
- the power spectrum of the reduced-analytic signal is the same as for the real data.

A specific MATLAB function has been developed to check this equivalence which converts the reduced-analytic signal in its real version using the correct sampling

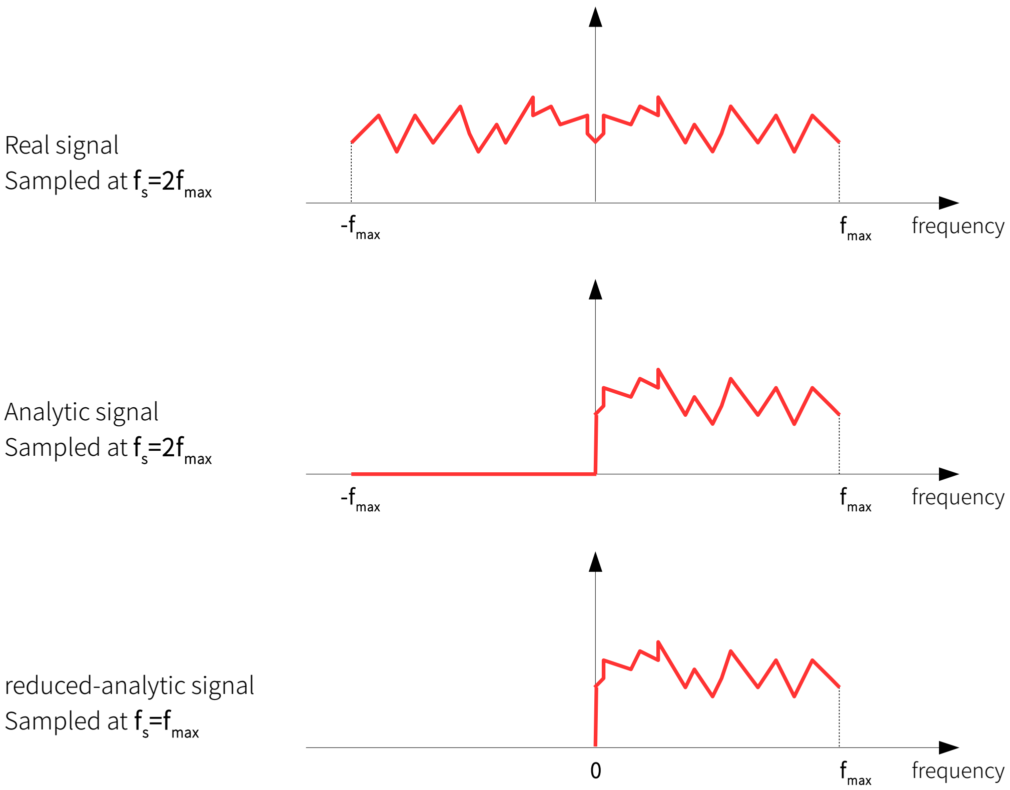

Figure 5.4. The Fourier transform of real valued function would appear with both positive and negative frequency components, which are symmetric around zero due to the Hermitian symmetry. The sampling frequency in this case should be (as required by the Nyquist theorem) at least twice the maximum frequency $f_s = 2f_{max}$, in order to avoid aliasing. In the analytic representation of a real-valued function, the negative frequency components are set to zero, while the sampling frequency will be the same as in the real-valued case. Our data is built discarding the negative-zero component of a classical analytic signal and it is sampled exactly at the maximum frequency of the positive band (the sampling will be half the sampling frequency used for the analytic signal). A perfect equivalence exists between the analytic and the reduced-analytic signal.

frequency. We decided to set the power spectrum equal to the original data, since we study our data better in the frequency domain (e.g. using Fourier transforms) rather than in time domain.

5.3.2 Data cleaning

BSD data are cleaned using various techniques. First, the short FFTs database used to build the BSD are vetoed for non-science segments (i.e. data corresponding to time segments when the detector was not locked or not working properly are set to zero) and subject to a cleaning step where big, short duration time disturbances are removed [28]. A further cleaning step is applied to the BSD data, which again consists in zeroing large time-domain disturbances which appear after band extraction. This is simply done by excluding samples above a given threshold. The threshold is taken, after a study based on real detector data, as $\theta_{thr} = 10 \times m_l$ where m_l is a sort of

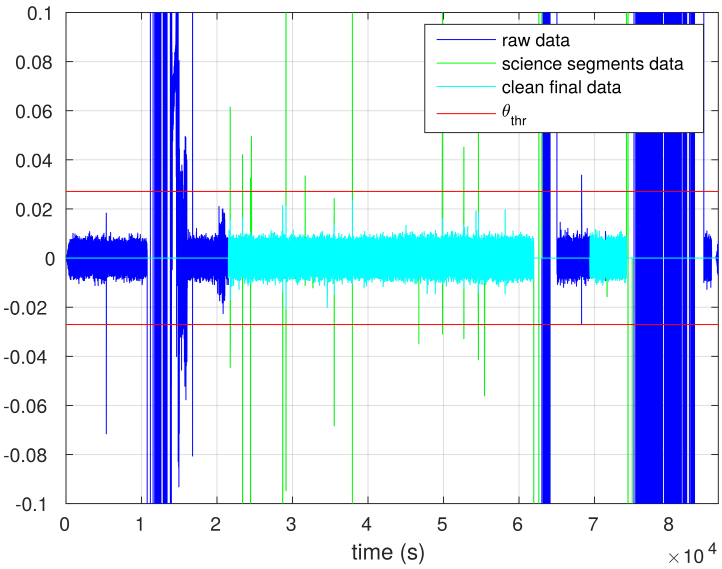

Figure 5.5. Time strain data (in units of 10^{-20}) before any cleaning is shown in blue. The selection of science data is done directly during SFDB construction (green). On this a further cleaning step is performed and residual large time-domain disturbances higher than a given threshold θ_{thr} (computed by Eq. 5.3) are put to zero (light blue: final cleaned data).

median level of our data and is evaluated from non zero samples $y_{t_{i;\bar{0}}} : \{y(t_i) \neq 0\}$ as:

$$m_l = \sqrt{\text{median}(Re(y_{t_{i;\bar{0}}}))^2 + \text{median}(Im(y_{t_{i;\bar{0}}}))^2} \qquad (5.3)$$

As an example, for O1 data the fraction of data excluded with this choice is around 2% for Livingston detector and 1% for Hanford, see Fig. 5.5. This is by purpose a *conservative* cleaning: with this threshold choice we are sure we are not excluding useful data. Furthermore, the threshold is chosen using the median rather than the mean value, in this way big disturbances counts as much as normal data without biasing the noise level. An extra cleaning procedure which deletes the more persistent lines and apply a time-frequency filter, built adaptively to the data, can be also applied, see Sec.XIII in [30], and [25]. This second cleaning informations are stored in the auxiliary time-frequency structure (see Appendix A).

5.4 Hetherodyne correction

A CW signal is modulated mainly by the Doppler shift and by the intrinsic spin-down of the source, as described in Sec.4.1. Such effects must be properly corrected in order to increase signal detectability. There exist many techniques to correct a CW signal. One standard technique is a data re-sampling, consisting in a re-definition of the time variable. Although the re-sampling has the advantage of being independent of the frequency, it can be computationally expensive for higher frequencies, for which the sampling time needed in order to have an enough accurate correction, should be quite low, which means that the number of samples in the phase correction we need to compute would be huge.

Heterodyne correction is more suitable for the BSD architecture. Let us assume that the frequency and spin-down parameters for a given source $[f_0, \dot{f}_0, \ddot{f}_0, \ldots]$ are known at the reference time t_0.

The signal phase shift due to the source spin-down can be written as (from Eq. 4.9)

$$\phi_{sd}(t) = 2\pi \cdot \int_{t_0}^{t} \left[\dot{f}_0 \cdot (t' - t_0) + \frac{1}{2} \ddot{f}_0 \cdot (t' - t_0)^2 + \ldots \right] dt' \tag{5.4}$$

From Eq. 4.8 the Doppler frequency shift is given by

$$\Delta f_{Dopp} = f_0(t) \left(\frac{\vec{v} \cdot \hat{n}}{c} \right) \tag{5.5}$$

the corresponding phase factor is:

$$\phi_d(t) = 2\pi \int_{t_0}^{t} f_0(t') \frac{\vec{v} \cdot \hat{n}}{c} dt' \approx \frac{2\pi}{c} \cdot p(t) \cdot f_0(t) \tag{5.6}$$

where $p(t)$ is the position of the detector in the SSB, obtained with a cubic polynomial interpolation from auxiliary data stored in the BSD file for each sample. In this way, using the position of the detector instead of the velocity, we don't need to explicitly integrate the velocity in time. In practice, the signal frequency f_0 in Eq. 5.6 is assumed to be constant at the value it would have, at the given reference time, after the spin-down correction. The final phase factor, containing both the Doppler and the spin-down terms is simply the sum of the two phases:

$$\Phi_{corr}(t) = \phi_d(t) + \phi_{sd}(t) \tag{5.7}$$

The effect of the Doppler shift and spin-down can then be corrected by multiplying the data by the exponential factor $e^{-j\Phi_{corr}(t)}$:

$$y(t) = [h(t) + n(t)]\, e^{-j\Phi_{corr}(t)} \tag{5.8}$$

where $h(t)$ is the strain amplitude of a GW signal in the detector, while $n(t)$ is the detector noise. In this way an hypothetical signal becomes monochromatic unless some residual modulations $\delta\Phi = \omega(t)t + \Phi_0 - \Phi_{corr}(t)$ which haven't been taken into account (e.g. second order spin-down, or slightly wrong position parameters of the source). After the correction there is still an amplitude modulation due to the non-uniform antenna pattern, which spread the signal power at five frequencies, as described in Sec. 4.1.

5.5 Possible applications of the BSD framework

Among the possible applications of the BSD framework, the most intuitive one is for targeted searches. Since the informations about the frequency and spin-down of the source are known, one can extract a narrow frequency band around the expected f_0, from the BSD database and build a single BSD file spanning the entire run. On this

BSD one can apply the heterodyne correction and matched-filtering, similarly to what is currently done.

The same procedure can be used in the follow-up stage of any CW search. Indeed this is a big improvement in the follow-up of candidates of semi-coherent searches. In particular, as in the follow-up stage we are interested in looking for an increase of the significance in a small region of the parameter space around the candidate, we can simply use the data around that particular candidate extracting a BSD sub-band and perform on this small volume a new incoherent search, using a longer coherence time, which implies a more accurate parameter estimation. This application is widely described in Sec. 6.5.

Another application that can be developed is a quick look tool for example to search for persistent lines or combs in the spectrum, especially using the cleaning information in the auxiliary time-frequency structure, like the persistency histogram for the identification of lines before correcting the time series.

In chapter 6 we will describe a brand new pipeline for directed searches of CW signals based on BSD.

5.6 Test with simulated signals

In this section we discuss some tests of the BSD framework, done using both software simulated signals (in condition of no-noise) and the so-called hardware injections, which are CW signals directly injected in the detector during science runs, through the coil drivers used to control the mirrors.

5.6.1 Software injections

For test purposes we have created a digitized discrete time series in the standard "frame" format (the typical file format used for the raw time series of the interferometers data as in Sec. 2.3) containing only signal without noise. From the "frames" we created the SFDB and the BSD for 1 month of data. We created a total of 4 signals, each in at least 2 out of 3 detectors (2 LIGOs and Virgo) as in table 5.2. The parameter of those simulations are exactly the same to the one used in hardware injections called "pulsar n" as in table 5.3.

Table 5.2. Pulsars injection frames produced for each detector marked with X.

Injection name	LIGO Hanford (O1)	LIGO Livingston (O1)	Virgo (VSR4)
Pulsar 2	X	X	
Pulsar 3	X		X
Pulsar 5		X	X
Pulsar 8	X	X	

As a verification that the procedure to produce BSD does not introduce any artifact, we have verified that the data written in the frame was coincident with the data stored in the BSD comparing the time series using the same sampling frequency. Moreover, we have used these fake signals to verify the scaling factors between the reduced-analytic signal and its real conversion, as stated in Sec. 5.3.1. These were in agreement with the results of a theoretical calculation, namely that the complex time amplitudes were half those of the real data, while in the spectrum we recovered the same amplitudes between the data in the frames and in the BSD.

Table 5.3. Parameters used for the construction of the injection frames. The reference time is MJD 52944.

Injection name	f_0 (Hz)	$\dot{f}_0$ (Hz/s)	$(\alpha,\delta)^\circ$	$\cos\iota$	ψ (°)
Pulsar 2	575.163573	-1.37×10^{-13}	(215.26, 3.44)	-0.92	77.3949
Pulsar 3	108.8571594	-1.46×10^{-17}	(178.37, -33.44)	-0.08	25.4390
Pulsar 5	52.80832436	-4.03×10^{-18}	(302.63, -83.84)	0.46	-20.85
Pulsar 8	194.3083185	-8.65×10^{-9}	(351.39, -33.42)	0.074	9.7673

We have also verified that the Doppler and spin-down correction procedure works properly, as shown in Fig. 5.6.

5.6.2 Hardware injections

Another verification step was done using the data (O1) from the two interferometers H1 and L1, where we tried to recover the so-called hardware injections, i.e. injected fake signals in the interferometer data, used by all the pipelines to test the robustness of their procedures. Ten hardware injections have been considered. Here we have reported a couple of examples of the application of the heterodyne corrections to the data where an HI is present.

We must say that in order to correct the signal we used the exact frequency of the injection, which is the main reason why we can easily see the 5 vectors in the spectrum. A further development of the method, which consists in a correction of a given signal using different parameters, will be discussed Section 6.1.

As shown in Figures 5.7 and 5.8, the 5-vectors typical shape is clearly visible. The peaks amplitudes depend on the source location and the modulation is given by the detector response.

Table 5.4. Table of recovered parameters mismatch for four hardware injections. The value of ψ recovered for the pulsar 2, is badly estimated due to the injection polarization which is nearly circular, hence in this case is ψ is ill-defined. This estimates have been done on 1 month of data, in a joint H1, L1 analysis.

Injection name	ϵ_{H_0}	ϵ_η	ϵ_ψ	coherence
Pulsar 2	0.9684	-0.0500	-0.4065	0.9895
Pulsar 3	1.0490	0.0013	-0.0031	0.9941
Pulsar 5	0.9588	0.0192	-0.0043	0.9856
Pulsar 8	0.9636	-0.0050	-0.0089	0.9916

In table 5.4 we report the ϵ_{H_0}, ratio of the estimated and injected amplitude, ϵ_η the normalized relative error on η, ϵ_ψ which is the normalized relative error on the estimated parameter ψ and the degree of coherence which characterize the "detection" reliability (See [29]). These estimates have been done using only 1 month of O1 data

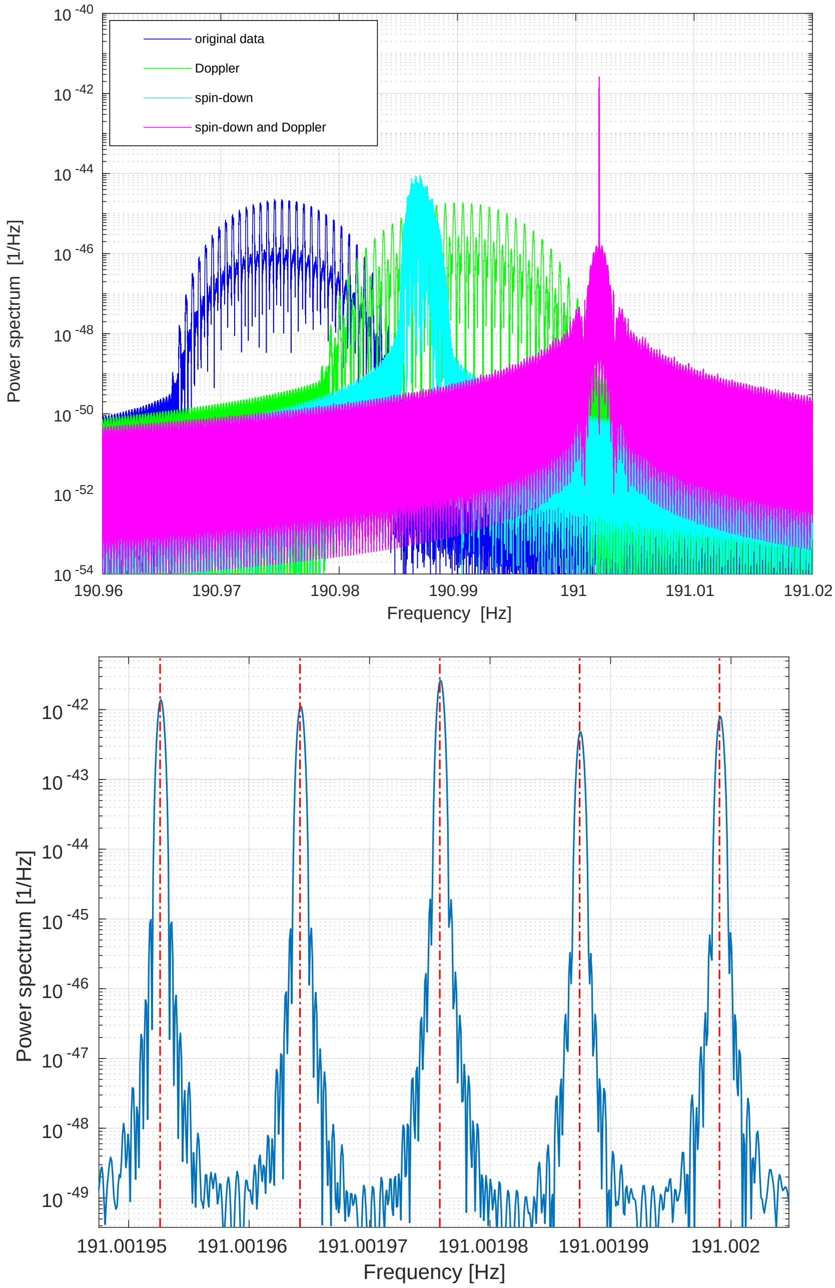

Figure 5.6. Upper plot: power spectrum of a software simulated signal with the same parameters as the hardware injection called pulsar 8, which parameters are shown in Tab. 5.3. Blue: original data from BSD; green: data corrected using the phase factor ϕ_d for the Doppler; cyan: data corrected using the phase factor ϕ_{sd} for the spin-down; (magenta): data corrected using the total phase factor $\phi_{sd} + \phi_d$. Bottom plot: zoom of upper plot. Vertical red lines indicates the expected position of the five frequency components produced by the sidereal modulation.

over a frequency band of 10 Hz. This is the result obtained from a joint parameter estimation combining the results from each detector. The parameter estimation can be improved using BSD spanning a longer amount of data (more than just 1 month).

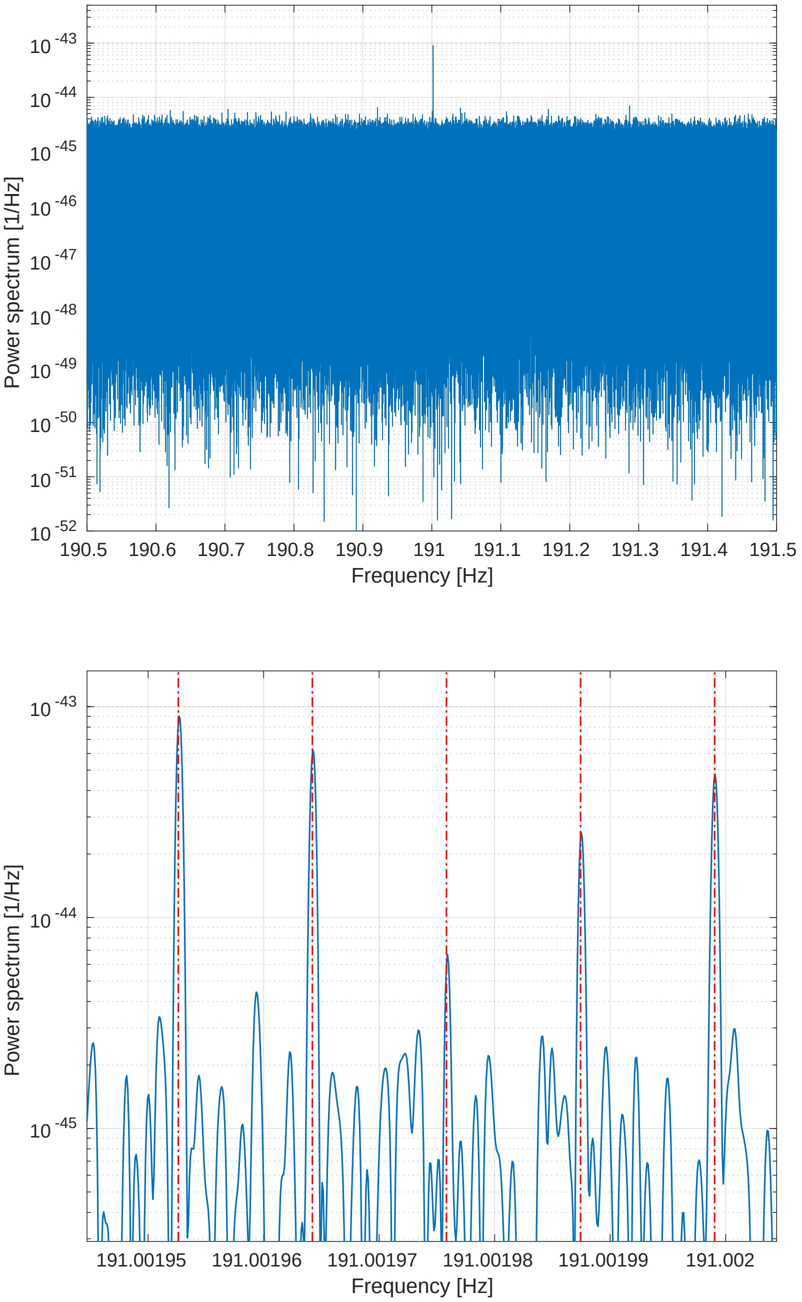

Figure 5.7. Spectrum of O1 LIGO Hanford data after the application of the heterodyne correction using parameters of hardware injected signal called pulsar 8. Bottom plot shows a zoom around the frequency of the injection. The signal shows the typical split of the signal power due to the sidereal motion of the detector. The dashed lines identify the theoretical frequencies of the sidereal peaks. The spectrum has been obtained starting from a BSD covering 1 Hz and 1 month.

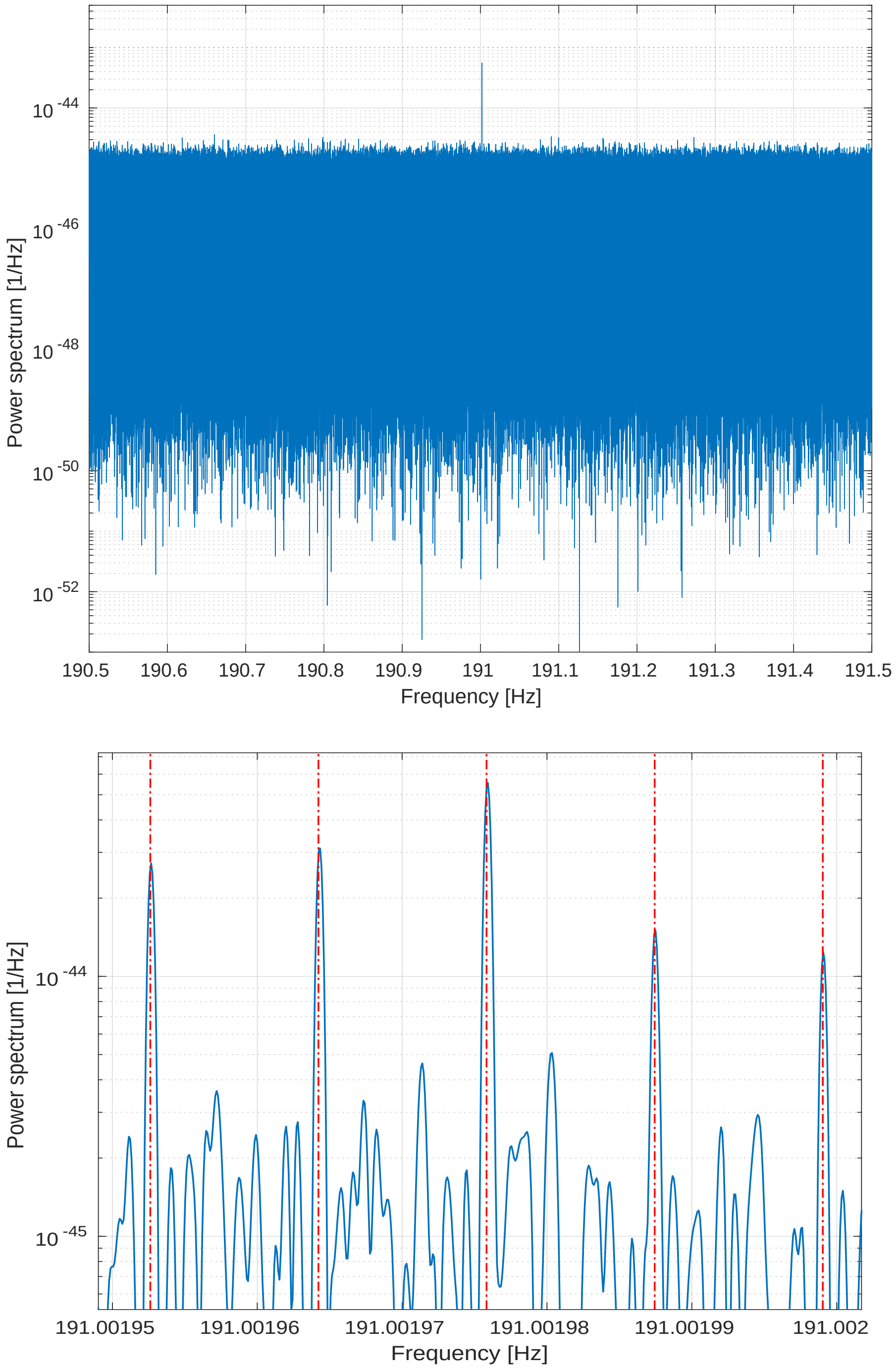

Figure 5.8. Spectrum of O1 LIGO Livingston data after the application of the heterodyne correction using parameters of hardware injected signal called pulsar 8. Bottom plot shows a zoom around the frequency of the injection. The signal shows the typical split of the signal power due to the sidereal motion of the detector. The dashed lines identify the theoretical frequencies of the sidereal peaks. The spectrum has been obtained starting from a BSD covering 1 Hz and 1 month.

Chapter 6

Directed search method based on BSD data

We developed a new directed search pipeline adapting into new BSD architecture, some well established concepts and procedures, such as the use of *peakmaps* and *Hough maps* for the selection of candidates (See [28],[27],[74],[53]). In particular the pipeline has been developed trying to obtain a good sensitivity with a very low computational cost of the search. As explained in Sec. 4.2, these two features are in opposition to each other, since the use of longer integration times (required to enhance the sensitivity of a given search), requires higher computing power.

We find a trade-off between those two constraints and in particular, since the available computational power is limited, we use some tricks to make a productive use of it, enhancing in a clever way the coherence time of our FFTs (and consequently also the sensitivity). When a signal is corrected or partially corrected, the maximum FFT length can be increased. In directed searches (See 4.2.2), the only parameter we know is the sky position of our source or a given sky region. For this reason, since we don't have any clue about the frequency and spin-down parameters $(f_0, \dot{f}_0, ...)$, Eq. 5.8 can't be used.

In Figure 6.1, the basic elements used in this pipeline are shown. The starting point are the BSD in the standard format file of $\Delta f_{BSD} = 10$ Hz and 1 month of data, to which a modified version of the heterodyne correction is applied. In this way we partially correct the Doppler effect as will be explained in the next section. Using this partially corrected time series, a new set of peak-maps is built, using longer FFTs as discussed in section 6.2. Those peak-maps will be the input files of the FrequencyHough transform from which the most significant candidates will be selected as described in sections 6.3, 6.4. A new follow-up procedure will be widely described in section 6.5. Finally, in Sec. 6.6 we will provide a theoretical formula for the search sensitivity.

6.1 Multi-Doppler correction

As explained in section 5.4, the classical heterodyne phase correction can be applied only if we have some information about the frequency and the rotational parameters of the source. Since this information is not available in directed searches, we need

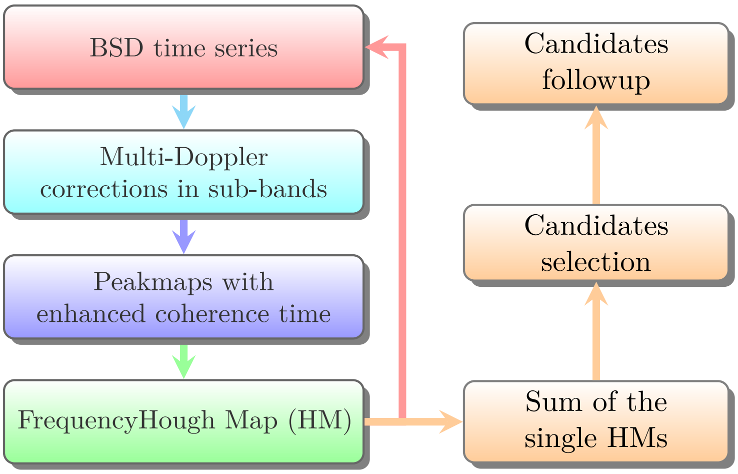

Figure 6.1. Scheme of the directed pipeline search. In this semi-coherent search we make use of the FrequencyHough transform as incoherent step.

to implement an alternative way to correct at least the Doppler effect. A modified heterodyne method has been developed for the purpose. The method, which is summarized in Figure 6.2, consists in applying an heterodyne correction in each 1 Hz band of the starting 10 Hz band BSD. In order to do so we go back in the frequency domain with a Fourier transform of the time series of the BSD. On this data we select the 1 Hz $i-$th band, simply multiplying the Fourier transform of the data $Y(f)$, with a step function (rectangular window) M_i equal to 1 in the selected frequency band and 0 outside. On the selected data we then apply the inverse Fourier transform (IFT) obtaining $y_i(t)$. On this sub-time series we apply a phase correction equal to:

$$\phi_i(t) = \frac{2\pi}{c} \cdot p_{\hat{n}}(t) \cdot f_i \tag{6.1}$$

where $p_{\hat{n}}$ is the position of the detector in the Solar System Barycenter reference frame, projected along a chosen sky direction $\hat{n}$ which can be the position of a known source, or one of the possible sky directions where we expect to find at least one source; f_i is the central frequency of the i-th sub-band. The corrected sub-time series will be simply

$$y_i'(t) = y_i(t) \cdot e^{-i\phi_i(t)} \tag{6.2}$$

The corrected final time series, valid for the entire 10 Hz band is given by the sum of all the $y_i'(t)$:

$$y_{MD} = \sum_{i=1}^{10} y_i(t) \cdot \mathrm{e}^{-i\phi_i} \tag{6.3}$$

Of course this correction won't be equally valid for all the signals contained in the 1 Hz band. In fact there will be a residual Doppler effect which increases the farther the signal frequency is from the central frequency f_i. For this reason an hypothetical signal will be only partially corrected.

This partial correction anyway is good enough that we are allowed to increase the coherence time (FFT length) by a proper factor (see next section).

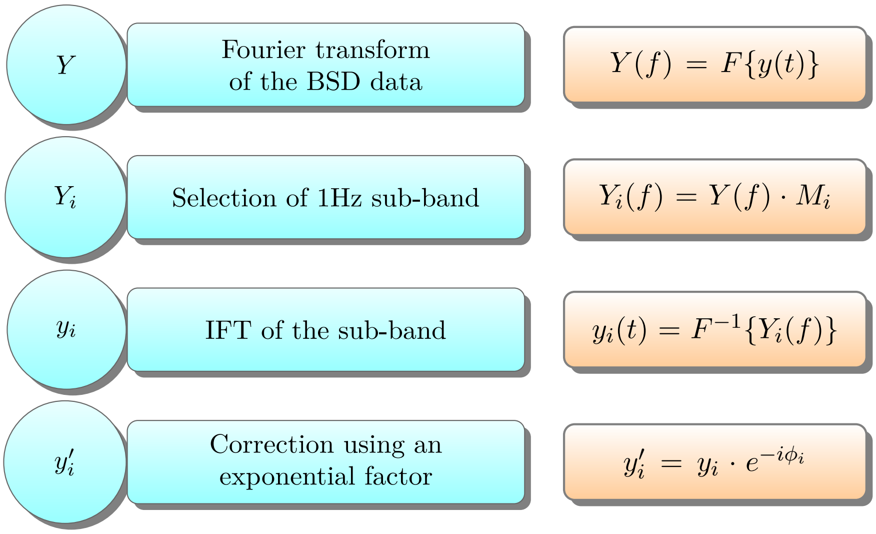
Y
Fourier transform of the BSD data
$Y(f) = F\{y(t)\}$
Y_i
Selection of 1Hz sub-band
$Y_i(f) = Y(f) \cdot M_i$
y_i
IFT of the sub-band
$y_i(t) = F^{-1}\{Y_i(f)\}$
y_i'
Correction using an exponential factor
$y_i' = y_i \cdot e^{-i\phi_i}$

Figure 6.2. Steps used for the Doppler effect demodulation

This procedure can be applied on a generic number of sub-bands even smaller than 1 Hz in the 10 Hz band, and this will decrease the residual Doppler effect in each sub-band. However we can't increase too much the number of sub-bands because the computational time to repeat the correction for many bands, will affect the total computational cost of the search. Furthermore as a marginal effect, when we deal with Fourier transform of the data, together with band extractions, several border effects can rise up, hence this can in principle affect the sensitivity of the search. This partial correction is applied to a single BSD time series, covering 1 month of data, and is repeated for each 10 Hz band.

6.2 Peakmaps

Following the scheme used in [5], the production of peak-maps is the first step of our hierarchical procedure. A peak-map is a collection of the most significant time-frequency peaks. Details about peak-map construction can be found in [28]. Here we briefly recall that a peak is selected when the following relation holds:

$$\mathcal{R}(i,j) = \frac{S_{P;i}(f_j)}{S_{AR;i}(f_j)} > \theta_{thr} \tag{6.4}$$

where $S_{P;i}(f_j)$ is the square modulus of the $i-$th FFT, also known as periodogram, and $S_{AR;i}(f_j)$ an auto-regressive average spectrum estimation. The ratio is computed for each $j-$th frequency bin of a given FFT. Each pair (i,j) made by the i-th initial time of a selected FFT and the corresponding $j-$th frequency bin is a peak. The threshold θ_{thr} has been chosen equal to 2.5 and a peak is selected only if it is a local maxima. This choice has been set accordingly to what is done in [5], as in this way we are less sensitive to spectral disturbances which usually (can) span more than a single frequency bin. If all the peaks are selected instead of local maxima only, the number of peaks will be prohibitive from a computational point of view while this choice significantly lowers the computational cost of the analysis. The peaks selection is a crucial point since if a peak is not selected at this stage, it will never be recovered. The threshold used for peaks selection will affect the final sensitivity of the search as will be discussed in section 6.6

As an example in Figure 6.3 are shown the time frequency peaks distribution while the color-bar is the logarithm of $\mathcal{R}(i, j)$ (defined in 6.2).

In the case of very strong signal (as for the pulsar 3) are present in the data, it is possible to found traces of it in the peak-maps as shown in figures 6.3.

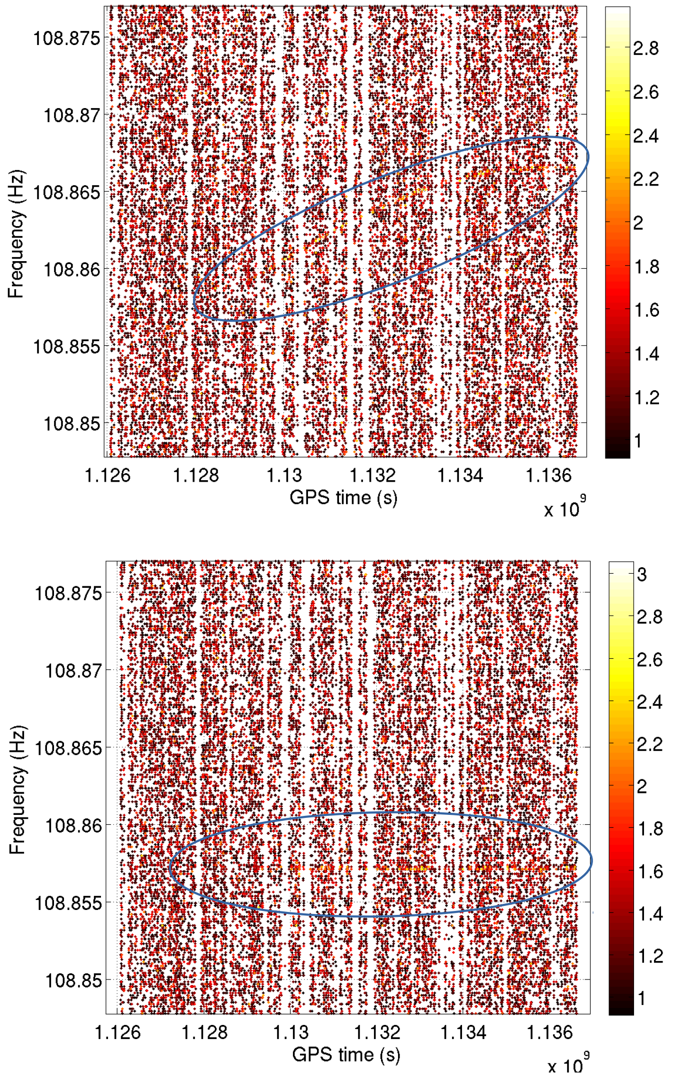

Figure 6.3. A peak-map is a collection of time-frequency peaks which are local maxima on the equalized spectrum. Those plots show an example of time-frequency peak around the hardware injection pulsar 3. In the upper plots is shown the peak-map before correcting the injection with the heterodyne. Before correction, the signal occupy several frequency bins in the nearby frequencies (see the faint curve inside the blue oval). After the correction (lower plot) the curved line became a straight line placed at the expected frequency of the hardware injection. The color-bar is the logarithm of $\mathcal{R}(i, j)$.

Since we have partially corrected our time series, we can choose a longer coherence time, with a first gain in sensitivity. This means, on the other hand, to increase the number of parameters investigated in the search, since, as will be explained in the next sections, the coherence time is related to the parameter space volume.

The new set of FFT has a length 4 times longer than the default (see Fig. 5.1). This number has been set empirically on the base of the available computational power. The new peak-maps are created for each BSD file on 1 month and 10 Hz. From this peak collection the FrequencyHough will be constructed as described in the next section. All the selected peaks at this stage will contribute to the Hough number count even if they are due to noise. Peaks probability are computed as discussed in Section 6.6.

6.3 Hough maps

For each peak-map spanning 1 month of data and 10 Hz we build the corresponding FrequencyHough (FH) map. The FH map is built for a single sky position since the starting peak-map has been corrected for the Doppler using $p_{\hat{n}}$. As described in section 6.5, it is possible to implement a modified FH map, which is built from several peak-maps corrected for different sky positions. In the practical application of this pipeline for sake of simplicity we used as FH input a peak-map corrected for a single sky point. It is possible to estimate the sky portion covered by a single sky bin, if we consider the maximum spreading due to the Doppler as:

$$\Delta f_{Dopp} \sim 2 \times 10^{-4} f_{max} \tag{6.5}$$

where f_{max} is the maximum frequency of a given band.

The Doppler effect will spread a signal in a number of frequency bins equal to:

$$N_{Dopp} = \frac{\Delta f_{Dopp}}{\delta f} \tag{6.6}$$

where δf is the frequency bin width (which is the inverse of the FFT time duration see Eq. 6.9a).

The sky size associated to the sky position (λ_0, β_0) is:

$$\Delta\lambda = \frac{1}{\mid N_{Dopp} \cos\beta_0 \mid} \tag{6.7}$$

$$\Delta\beta = \frac{1}{\mid N_{Dopp} \sin\beta_0 \mid} \tag{6.8}$$

This is a general evaluation which can be used for the estimation of the sky patch covered by a search like the one described in chapter 7.

If we are analyzing a certain number of months, we can operate in 2 ways: we can produce a "big" peak-map spanning the total amount of time we are analyzing (e.g. 4 months but a narrow frequency band), or we can sum up the single FH maps from the monthly based peak-maps. The most convenient way, from a computational point of view, is to proceed with the second option. This operation does not affect the sensitivity of the search nor introduce artifacts in the analysis, since the Hough transform is a linear operation, thus we are allowed to sum up single FH maps as long as they are referred to the same reference time.

The resolution of this map is given by the FFT length (T_{FFT}) used in the peak-map construction step. In particular the "natural" grid in the frequency and spin-down will be given by:

$$\delta f = \frac{1}{T_{FFT}} \tag{6.9a}$$

$$\delta \dot{f} = \frac{1}{2 T_{obs} T_{FFT}} \tag{6.9b}$$

where T_{obs} is the observational time. As described in reference [30], we keep the over-resolution factor in frequency (K_f) since it is convenient and it does not imply an increase of the computational cost of the search. The spin-down bin is given by Eq. 6.9b using a certain value for T_{obs} (observational time) which is set accordingly to the search we want to do.

As shown in Figure 6.4 as an example using the HI pulsar 3, we can clearly see a large number count close to the injection position in the frequency/spin-down plane. Both plots have been built using the same resolution steps; the difference lies in the way the signal has been corrected. For plot (a) we used the Multi-Doppler corrections (no spin-down), while in plot (b) the signal has been corrected using the exact parameters of the source, including the spin-down. The maximum number count are respectively 82 and 78 as can be seen from the color-bar values; this difference is compatible with noise fluctuations. As can be intuitively understood, when the signal is corrected using all the parameters we know, the maximum number count will be centered at the frequency/spin-down position of the source, while it will be slightly shifted when we use only the sky position (as in this case).

6.4 Candidate selection

The most significant candidates are selected on the final Hough map, sum of the monthly Hough maps. A fixed number of candidates N_{cand} is selected, based on a ranking on the Hough number count, in each 10 Hz band (Δf_{BSD} the band of the BSD file). As shown in Figure 6.5, firstly we select all maximum number counts per each Hough frequency bin over the entire spin-down range. At this stage the number of selected candidates will be equal to the total number of Hough frequency bins $N_f = \frac{\Delta f_{BSD}}{\delta f_H}$ (δf_H in this case will be $\frac{\delta f}{K_f}$ where the over-resolution factor should be taken into account). On a second step, the selected candidates are divided in frequency sub-bands which width is equal to $\frac{\Delta f_{BSD}}{N_{cand}}$. For each sub-band the frequency/spin-down-bin with the maximum number count is selected. In this way the number of candidates selected will be equal to N_{cand}

This procedure has been used also in the last all-sky search using the Frequency-Hough transform [5]. This is a very robust candidate selection technique as discussed in [30], which permits a nearly uniform final distribution of selected candidates over the frequency. Indeed if a line or a disturbance is present in the data, this can occupy several nearby bins in frequency and spin-down, in this case we will not be blinded by the presence of the disturbance.

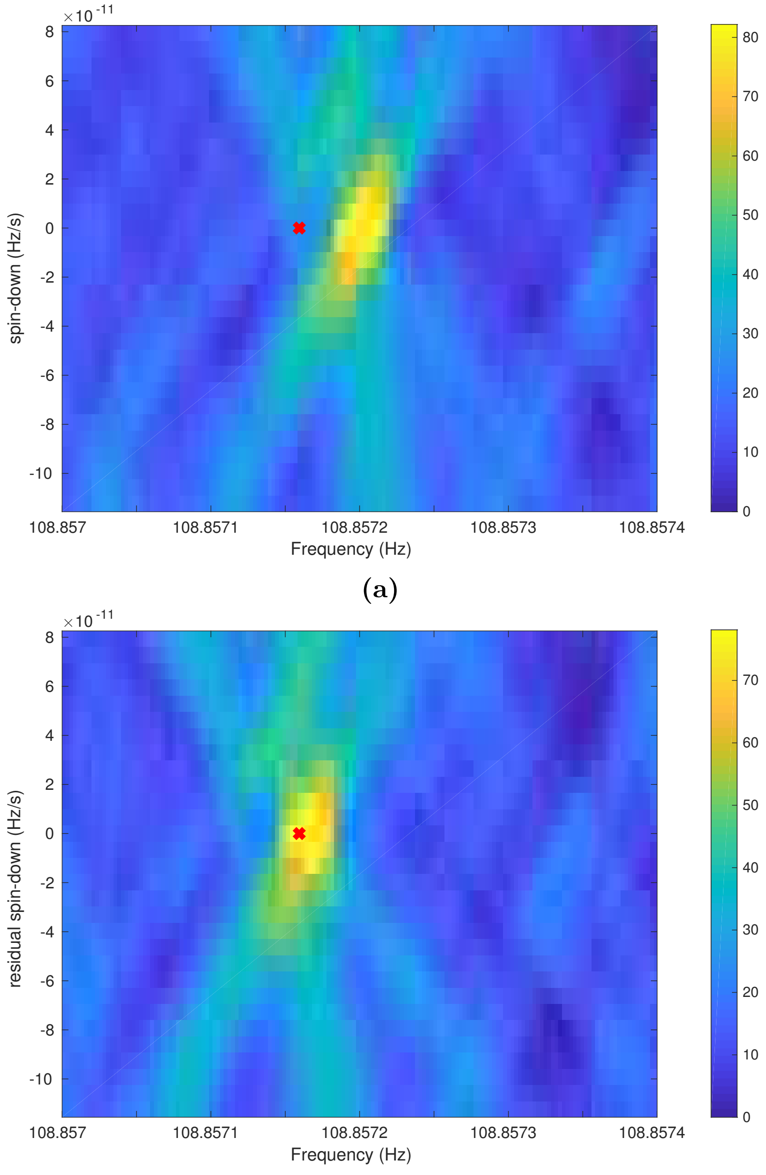

(a)

(b)

Figure 6.4. Example of HM using the Multi-Doppler approach (a), and the targeted one (b). The signal is well visible in both HMs even if the parameters in plot(a) are not exactly centered at the correct source frequency and spin-down position (red cross), is still close enough to be detected as a candidate. This plot has been done using 1 month of O2 C01 calibrated data of Hanford detector. The (b) plot shows the residual spin-down factor, since we have already corrected the signal for the spin-down; on the contrary (a) plot is corrected only for the Doppler with Multi-Doppler corrections. The spin-down of this injection is small thus we don't see a big difference between the (a) and (b) spin-down parameters

A further step in this screening phase, consists in the selection of a second round of candidates. Those "second order" candidates are picked (per sub-band) in a region far from the "first order" candidates, and equal to ±8 frequency bins, after removing

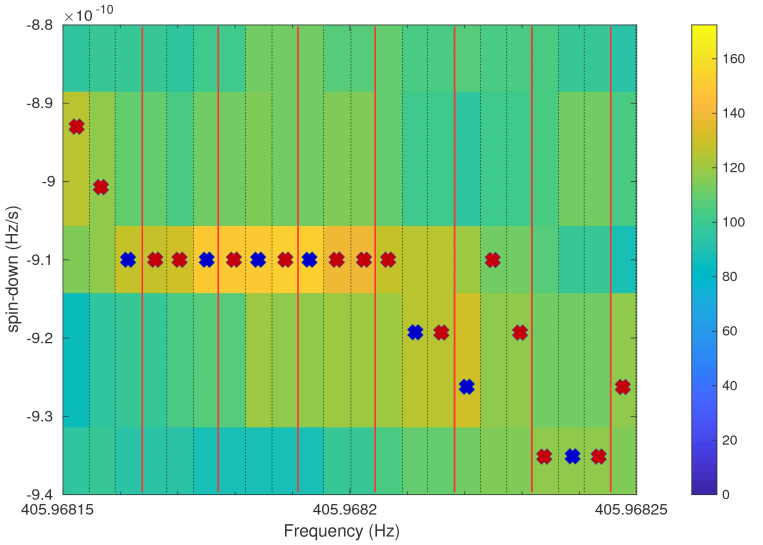

Figure 6.5. Candidate selection procedure. Each dashed vertical line is a frequency bin. The red/blue cross are the correspondent position in the spin-down of the maximum number count for that particular frequency bin. Once the candidates have been selected one per each frequency bin, the entire band is divided in order to obtain a certain number of final candidates. In this scheme as an example, the sub-band width on which the final candidates are selected, is of 3 frequency bin. Among the 3 previously selected candidates only the one with the higher number count will survive (blue crosses).

a region of ± 4 frequency bins around the "first order" selected candidate.

With this procedure, the final number of selected candidates will be $\sim 2N_{cand}$ per each Δf_{BSD} band, and if a big disturbance or an hardware injection is present, we will obtain only 1 candidate (the first order one) in the sub-band.

6.4.1 Coincidences

In order to reduce the false alarm probability, the final set of candidates obtained from a previously analyzed dataset, is compared to a second set of candidates produced by the analysis of the data belonging to a different detector or a different time span (different run). Coincidences among the two sets of candidates are done because if a signal is really present it should produce a candidate with similar parameters also in a second dataset. Since CW signals are persistent in time, this criteria can be applied also for a pair of (or more) datasets spanning different time periods, although this is true only if the two datasets have a comparable sensitivity. Candidate parameters are defined by source frequency, celestial coordinates and its first spin-down parameter.

It can be shown that, in the assumption of Gaussian noise, the expected number of coincidences between two datasets will be:

$$N_c = \frac{N_{c1}N_{c2}}{m} \tag{6.10}$$

where m is the total number of cells in the parameter space computed as $m = \sum_i^{N_{band}} m_i$ with $m_i = n_{fi} \times n_{sdi}$ the number of cells investigated for each 10 Hz band, given by the number of frequency bins times the number of the spin-down cells.

In order to do coincidences, we choose a coincidence window around the candidate parameters. The window size is chosen as a trade-off between the number of final candidates we are able to follow-up (which is strictly connected to the computational power available), and the need to not discard real signal candidates that can appear with slightly different parameters in the two datasets, due to noise fluctuation.

The choice of few bins per each parameter is a standard reasonable one. The number of expected coincidences in equation 6.10 is a function of the coincidence window, this number will doubled also when the "second order" candidates are selected.

On the coincident candidate a follow-up is done in order to reject it as a signal. In the next section we will describe a follow-up procedure based on [30], adapted for the BSD framework.

6.5 Candidate Follow-up

A first glimpse on the data around coincident candidates can suggest which of them has a non-gravitational origin. In particular it is very useful to take a look at NoEMi pages (a line monitoring software already described in Chapter 3), to discard candidates coming from known lines (this step can be done also before coincidences). For candidates not coincident with known noise lines, a follow-up procedure is applied. In this section we describe a follow-up procedure using BSD and based on an improved semi-coherent method. The standard idea behind a generic follow-up is to analyze the data over small volume, usually the same used for coincidences. This stage eventually can increase the detection confidence and better estimate the candidate parameters.

The computational cost of the follow-up affects the number of candidates we can follow-up, and at the end it will indirectly have an impact on the search sensitivity.

In Figure 6.6 the main blocks of the follow-up procedure, which we now describe, are shown.

1. Band extraction and 2. correction of the time series

As shown in Figure 6.6, the first step is a frequency band extraction from BSD. For each candidate we want to follow-up, a frequency band large enough to contain the Doppler and spin-down variations, is extracted from BSD files around the candidate. The resulting BSD will contain a time series of a small frequency band ($\sim$ 1 Hz) and covering the total time of the search and sampled at the inverse of the bandwidth. On this sub-band we apply the barycentric and spin-down corrections using standard heterodyne phase corrections as in Section 5.4 using the rotational parameters of the candidate $(f_0, \dot{f}_0, \alpha, \delta)$.

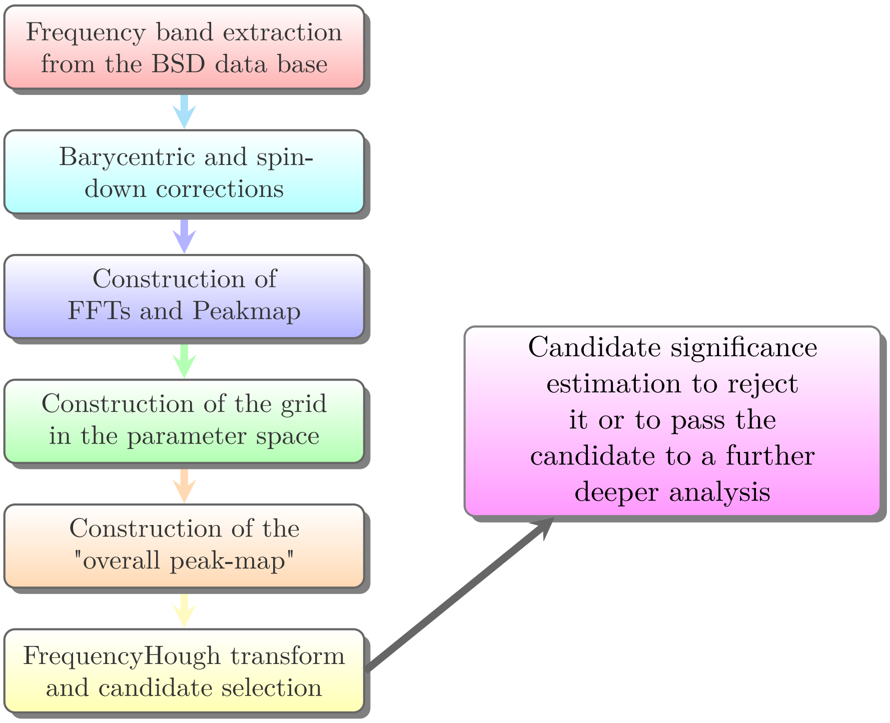
Frequency band extraction from the BSD data base
Barycentric and spin-down corrections
Construction of FFTs and Peakmap
Construction of the grid in the parameter space
Construction of the "overall peak-map"
FrequencyHough transform and candidate selection
Candidate significance estimation to reject it or to pass the candidate to a further deeper analysis

Figure 6.6. Scheme of the follow-up. All these steps are repeated for each candidate.

3. Construction of FFTs and Peakmap

Since we have corrected the time series, similarly to what happen in the first stage of the search, we can build a set of FFTs ($\sim \times 10$) longer than the one used for the peakmap construction in section 6.2. We will have a resulting peakmap corrected for the sky position of our directed search, which covers the full observation time since we have extracted a short frequency band. Enhancing the coherence time permits a gain in the signal to noise ratio of $\sqrt{\frac{T_{FFT_{new}}}{T_{FFT}}}$ thus this is a crucial step in order to increase our detection confidence.

4. Grid in the parameter space

The size of the follow-up volume can be set in terms of number of bins of the coarse grid. We call coarse bin the resolution used in the initial search (the initial bin sizes). Usually this volume corresponds to few coarse bins in frequency, spin-down and sky. Generally speaking for directed searches the number of sky bins used in the follow-up stage is equal to the initial number, since this is the only parameter we assume as known. Eventually this sky patch can be refined.

Frequency and spin-down A grid in the parameter space is built, centered at the candidates parameters and such to cover the follow-up volume. The new refined grid steps are:

$$\delta f_{ref} = \frac{\delta f}{\gamma} = \frac{1}{T_{FFT_{new}}} \tag{6.11a}$$

$$\delta \dot{f}_{ref} = \frac{\delta \dot{f}}{\gamma} \tag{6.11b}$$

with $\gamma = \frac{T_{FFT_{new}}}{T_{FFT}}$ as the enhancing factor. The number of refined spin-down bins we want to investigate can be set in terms of coarse bins $n_{\dot{f}_{coarse}}$ as:

$$n_{\dot{f}_{ref}} = 2\gamma n_{\dot{f}_{coarse}} + 1 \tag{6.12}$$

From which the resulting spin-down range will be: $\Delta \dot{f}_{fu} = n_{\dot{f}_{ref}} \cdot \delta \dot{f}_{ref}$

For the frequency, we select a small band around the candidate which width is given by the sum of (1) the estimate of the maximum variation in frequency in the spin-down range $\Delta \dot{f}_{fu}$, plus a contribute of (2) the residual Doppler (Δf_{sky}):

$$\Delta f_{fu} = 2 \left[T_{obs} \frac{\delta \dot{f}_{fu}}{2} \left(n_{\dot{f}_{ref}} + 1 \right) + \Delta f_{sky} \right] \tag{6.13}$$

where $\Delta f_{sky} = \max(|\delta v|) f_0$, δv is the Doppler residual velocity computed in 6.21 and f_0 is the candidate frequency at a given reference time t_0.

Sky grid A grid is built also in the sky in order to cover almost the same spot around the original search sky patch, but with a refined grid cell. In other words the initial sky spot (which is built from a single sky point as in Eq.6.7 and 6.8) is divided in a refined sky grid. The mini-sky cell of the grid will have the following fixed size:

$$\Delta \lambda_{new} = \frac{1}{K_{sky} \mid N_{D_{new}} \cos \beta_0 \mid} \tag{6.14}$$

$$\Delta \beta_{new} = \frac{1}{K_{sky} \mid N_{D_{new}} \sin \beta_0 \mid} \tag{6.15}$$

where K_{sky} is the over resolution we want to have for the new grid. The new number of Doppler bins is estimated as

$$N_{D_{new}} = 2 \times 10^{-4} \cdot \frac{f_{cand}}{\delta f_{ref}} \tag{6.16}$$

In this way the λ_i coordinates of the new grid will all be separated by $\Delta \lambda_{new}$, as well as for β. The number of λ and β points in the new grid is a parameter we can arbitrarily choose, and is defined as:

$$n_\lambda = n_\beta = 2 \times d_{sky} \times K_{sky} + 1 \tag{6.17}$$

where d_{sky} is an enlargement factor in case we want to build a larger sky patch. As shown in Figure 6.7, we can see an example of a refined sky grid using a $K_{sky} = 4$ and $d_{sky} = 1.5$.

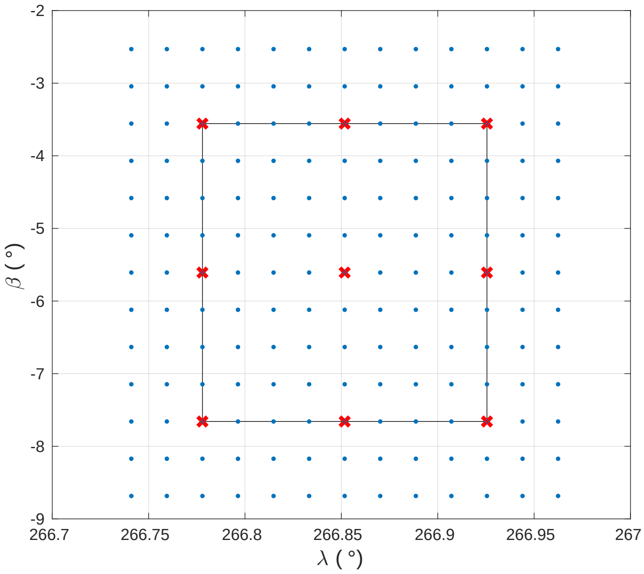

Figure 6.7. Example of sky grid using an enlargement factor of 1.5 and an over resolution of 4. The rectangle is the initial sky bin while blue dots are the new points of the refined grid. The distance between two red crosses is the original sky size.

5. Construction of the "overall peak-map"

Once the sky grid is ready, we can compute the "overall peak-map" which consists in a set of corrected peak-maps, each for a different sky point of the new sky grid. To do so we start from the peak-map corrected for the Doppler and spin-down, using the parameters of the candidate. From this we select all the peaks in the portion of parameter space set by the follow-up volume. Properly shifting those peaks, we can build a set of corrected peak-maps which will form the "overall peak-map".

This is a very convenient way to correct those peak-maps, rather than using the heterodyne which should be applied to the time series. Of course this method can't be applied to sky points too far away for the starting one, since if we don't correct with high precision the starting peak-map, we can have a "propagation" effect of the error, which will produce a set of peak-maps not properly corrected.

The time-frequency peaks are shifted as:

$$fp_{j;i} = fp_{0,i}\left(1 + \frac{\delta v(j,i)}{c}\right) + j \cdot \text{offset} \tag{6.18}$$

where fp_0 indicates the frequency of the peak in the starting peak-map. j is the index running on the sky position, i is the index of the time and the offset is a constant value used for the frequency separation of the peak-maps.

In order to compute δv with respect to the position (λ_c, β_c) of our candidate, we considered the residual velocities of the nearby points r_i as illustrated in figure 6.8

below.

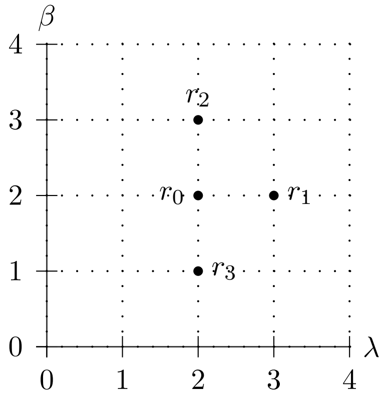

$$\begin{aligned} r_0 &\longrightarrow (\lambda_c, \beta_c) \\ r_1 &\longrightarrow (\lambda_c + 1^\circ, \beta_c) \\ r_2 &\longrightarrow (\lambda_c, \beta_c + 1^\circ) \\ r_3 &\longrightarrow (\lambda_c, \beta_c - 1^\circ) \end{aligned}$$

Figure 6.8. Sky directions for wich we compute the directional residual velocities.

For each point r_i we can compute the values dv_{s_i} which are defined as:

$$dv_{s_1} = \overline{v} \cdot \overline{r}_1 - v_s \tag{6.19a}$$

$$dv_{s_2} = \overline{v} \cdot \overline{r}_2 - v_s \tag{6.19b}$$

$$dv_{s_3} = v_s - \overline{v} \cdot \overline{r}_3 \tag{6.19c}$$

where $v_s = \overline{v} \cdot \overline{r}_0$ and $\overline{v}$ is the detector velocity vector in the SSB. Those values are the unitary differential velocities along the 3 directions λ, $\pm\beta$ (the last two can be different so we need to distinguish between the 2 verses).
Those variations are valid for a sky shift equal to $\pm 1^\circ$ in order to generalize this calculation for a random sky point which lies closer than $\pm 1^\circ$ to (λ_c, β_c) we can multiply them by the proper sky shift as:

$$dv_\lambda = (\lambda_i - \lambda_c)\, dv_{s_1} \tag{6.20a}$$

$$dv_\beta = \begin{cases} (\beta_i - \beta_c)\, dv_{s_2} & : \beta_i > \beta_c \\ (\beta_i - \beta_c)\, dv_{s_3} & : \beta_i \leq \beta_c \end{cases} \tag{6.20b}$$

The total residual Doppler velocity to be used in Eq. 6.18 can be computed as:

$$\delta v = dv_\lambda + dv_\beta \tag{6.21}$$

In figure 6.9 an example of overall peak-map is shown. Each stripe correspond to the original peak-map corrected for a given sky point in the refined grid.

6. Hough map and candidate selection

The overall peak-map is the input file of the Hough map. The resulting Hough map will be a collection of small FrequencyHough maps each corrected as described in the previous section and will appear as in Figure 6.10. From this multi-Hough map only the most significant candidate is selected. What we expect to see after the follow-up is an increase of the candidate significance, like the Hough number count or the critical ratio.

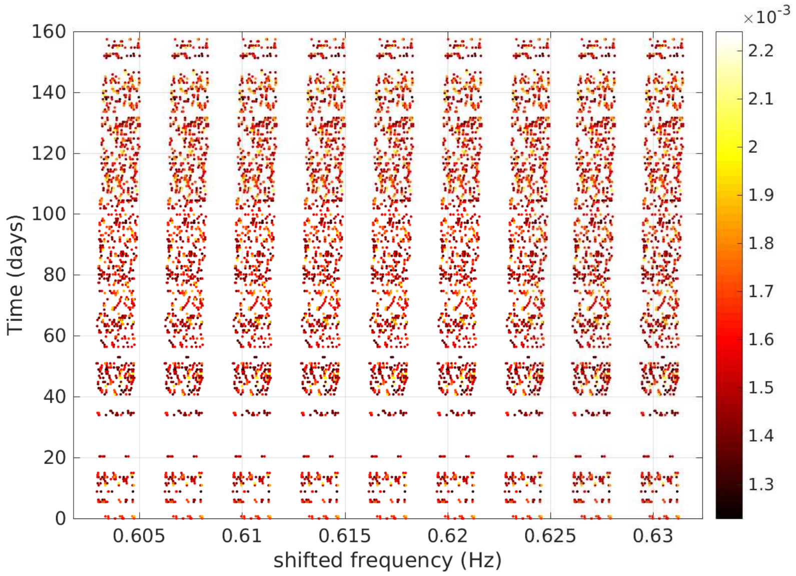

Figure 6.9. Example of an overall peak-map. In figure are clearly visible 9 "stripes". Each correspond to a corrected peak-map for a given sky point. The frequency on the x-axes is not a physical quantity. Colorbar indicates the peaks amplitude.

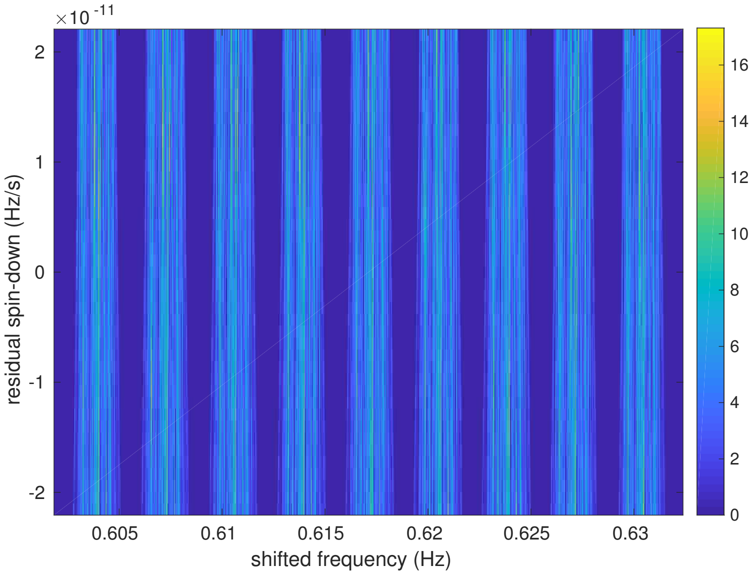

Figure 6.10. Example of the overall HM built from the overall peak-map as shown in figure 6.9. In figure are clearly visible 9 "stripes". Each correspond to the HM done on a corrected peak-map for a given sky point. The frequency on the x axes is not a physical quantity. Colorbar indicates the Hough number count. The spin-down range is set accordingly to cover few bins around the candidate.

From a practical point of view we can correct the starting peak-map using the parameter estimated for the loudest candidate in the follow-up stage. We can then do an histogram of the peak-maps searching for significant peaks and in particular compare this histogram with the one of the peak-map corrected using the parameters of the candidate before the follow-up stage.
For real GW signals we expect that the number of peaks around the candidate will increase after the follow-up.

6.6 Sensitivity estimation

As already mentioned in previous chapters, the final sensitivity of the search is strictly connected to the coherence time we used in the first stage of the analysis, and it will also depend on the thresholds we use for peaks and candidate selection. We define the sensitivity at a given confidence level Γ, as the minimum signal amplitude which will produce a candidate in a fraction at least equal to Γ among a set of repeated experiments. The sensitivity of a hierarchical semi-coherent search, can be computed under the assumption of Gaussian noise as discussed in [30].

6.6.1 Peaks probability

We want to briefly give some elements which are useful to compute the theoretical sensitivity of our search and underly the importance of the threshold for the selection of the peaks.
The probability of selecting a peak, which can be produced by noise ($\lambda = 0$) or by a real signal with spectral amplitude equal to λ[1], above a threshold θ and which is a local maxima can be written as:

$$P(\theta, \lambda) = \int_{\theta}^{\infty} p(x, \lambda) \left(\int_{0}^{x} p(x', \lambda) dx' \right)^2 dx \tag{6.22}$$

where the integral under round brackets is the probability that the selected peak is a local maxima (which implies that the two neighboring bins have a smaller value of $R(i, j)$ see definition Eq. 6.2).
The probability density of the spectrum is a normalized non-central χ^2 with 2 degrees of freedom and non-centrality parameter λ:

$$p(x; \lambda) = e^{(-x-\frac{\lambda}{2})} I_0(\sqrt{2x\lambda}) \tag{6.23}$$

where I_0 is the modified Bessel function of zeroth order (which has mean value $\overline{x} = (1 + \lambda/2)$ and variance $\sigma_x^2 = 1 + \lambda$).
For small $\lambda \ll x$ we can approximate it with:

$$p(x; \lambda) \approx e^{-x} \left(1 - \frac{\lambda}{2} + \frac{\lambda}{2} x \right) \tag{6.24}$$

In the case of gaussian noise the probability distribution is an exponential with mean value and standard deviation equal to 1, and this is clear if we substitute $\lambda = 0$ to

---

[1] $\lambda = \frac{4|\tilde{h}(f)|^2}{T_{FFT} S_n(f)}$, $\tilde{h}(f)$: signal Fourier transform, T_{FFT}: time baseline of the FFT, $S_n(f)$: detector noise spectral density (unilateral)

Eq. 6.23 or more simply in Eq. 6.24. If we compute Eq. 6.22 for the case of only noise $p_0 = P(\theta, 0)$ we obtain:

$$p_0 = e^{-\theta} - e^{-2\theta} + \frac{1}{3}e^{-3\theta} \tag{6.25}$$

If a signal λ is present this probability $P(\theta, \lambda)$ will turn out as:

$$p_\lambda \approx p_0 + \frac{\lambda}{2}\theta\left(e^{-\theta} - 2e^{-2\theta} + e^{-3\theta}\right) \tag{6.26}$$

From which is clear that the choice of the threshold θ affects the number of selected peaks. A big number of selected peaks has a direct negative consequence on the computational cost of the search, but at the same time this number can't be too low since if we miss a peak coming from an hypothetical signal at this stage, we won't be able to recover it in the following steps of the analysis.

6.6.2 Hough number count probability

The hough number count n in a given pixel is the result of a binary sum of 0 and 1 n_i as:

$$n = \sum_i^N n_i \tag{6.27}$$

where N is the number of FFT used for the map construction. Then n is a random variable with a binomial distribution for which the probability of having a number count n can be expressed as:

$$P_n(\theta; \lambda) = \binom{N}{n} \eta^n (1-\eta)^{N-n} \tag{6.28}$$

where η is the peak selection probability p_0 when no signal is present and p_λ when a signal is present. The mean and variance for this distribution are respectively

$$\mu = N\eta \tag{6.29a}$$

$$\sigma^2 = N\eta(1-\eta) \tag{6.29b}$$

The selection of candidates is based on the Hough number of count thus also the threshold we choose in this stage will affect the sensitivity of the search.

6.6.3 Peaks threshold

We can choose the threshold θ_{thr} for the peaks selection as that value that maximize the expected value of the statistical significance of the Hough number count in a given pixel. The variable which measures the statistical significance of a certain number count n with respect to the expected value in presence of noise alone is called Critical Ratio (CR) and is defined as:

$$CR = \frac{n - Np_0}{\sqrt{Np_0(1-p_0)}} \tag{6.30}$$

where, as shown in Eq. 6.29a, Np_0 is the number count mean value in presence of noise and $\sigma = \sqrt{Np_0(1-p_0)}$ is its standard deviation (Eq. 6.29b). In case a signal with spectral amplitude λ is present, the expected value of the CR becomes[2]

$$E[CR] = \mu_{CR}(\theta, \lambda) = \frac{N(p_\lambda - p_0)}{\sqrt{Np_0(1-p_0)}} \tag{6.31}$$

This is the function we want to maximize in order to choice the proper value of θ. As discussed in [30], the optimal choice for θ_{thr} is slightly less than 2.5 but a reasonable choice is at $\theta_{thr} = 2.5$ since it helps reducing by a factor of 2 the number of selected peaks in front of a sensitivity loss of $\sim 1\%$.

6.6.4 Hough counts threshold

Using the definition of the Hough number count probability P_n in Eq. 6.6.2 we can define the corresponding false alarm probability as:

$$P_{fa}(\lambda) = \sum_{n=n_{thr}}^{N} P_n(\theta_{thr}, 0) \tag{6.32}$$

where n_{thr} is the number count threshold we use for candidates selection. On the other hand the false dismissal probability will be:

$$P_{fd} = \sum_{n=0}^{n_{thr}-1} P_n(\theta_{thr}, \lambda) \tag{6.33}$$

Those equation can be computed analytically if we use the gaussian approximation of the binomial distribution P_n. In this way P_{fa} and P_{fd} can be written as function of the Hough number count threshold n_{thr}

$$P_{fa} = \frac{1}{2}\text{erfc}\left(\frac{n_{thr} - Np_0}{\sqrt{2Np_0(1-p_0)}}\right) \tag{6.34}$$

The last relation can be written in terms of a Critical Ratio threshold CR_{thr} which is the value of CR in Eq 6.30 when $n = n_{thr}$.
Using the gaussian approximation, the false dismissal probability becomes

$$P_{fd} = \frac{1}{2}\text{erfc}\left(\frac{Np_\lambda - n_{thr}}{\sqrt{2Np_\lambda(1-p_\lambda)}}\right) \tag{6.35}$$

where erfc is the complementary error function[3].
In this way we have a relationship between the n_{thr} and the false alarm probability and the false dismissal probability which is the complementary of the detection probability (P_d) as $P_d + P_{fd} = 1$.

---

[2] the expected value of the CR in presence of noise alone is equal to 0

[3] defined as $\text{erfc}(x) = \frac{2}{\sqrt{\pi}} \int_x^\infty e^{-t^2} dt$

6.6.5 A formula for the sensitivity

At this point we have all the ingredients to compute analytically the sensitivity of the search, assuming gaussian noise, based on the choice done on the thresholds. As mentioned at the beginning of the section, in order to talk about sensitivity we need to establish a degree of confidence (confidence level).
In fact the confidence level Γ is the detection probability, thus we can write it as a function of the false dismissal probability as $\Gamma = 1 - P_{fd}$ that can be simplified as:

$$\text{erfc}\left(\frac{n_{thr} - Np_{\lambda}}{\sqrt{2Np_{\lambda}(1-p_{\lambda})}}\right) = 2\Gamma \tag{6.36}$$

We can substitute in this last equation the expression of n_{thr} in function of the false alarm probability as in Eq. 6.34 and, using the analytical form of p_{λ} and p_0 (Eq. 6.26, 6.25), we can get the approximation of the minimum detectable spectral amplitude λ as:

$$\lambda_{min} \approx \frac{2}{\theta_{thr}}\sqrt{\frac{p_0(1-p_0)}{Np_1^2}}\left(CR_{thr} - \sqrt{2}\text{erfc}^{-1}(2\Gamma)\right) = \frac{\Lambda_1}{\sqrt{N}} \tag{6.37}$$

where $p_1 = e^{-\theta_{thr}} - 2e^{-2\theta_{thr}} + e^{-3\theta_{thr}}$. We can express the minimum detectable spectral amplitude in terms of the minimum detectable strain amplitude $h_{0_{min}}$ as

$$h_{0_{min}}^{\Gamma} \approx \frac{4.02}{N^{1/4}\theta_{thr}^{1/2}}\sqrt{\frac{S_n(f)}{T_{FFT}}}\left(\frac{p_0(1-p_0)}{p_1^2}\right)^{1/4}\sqrt{CR_{thr} - \sqrt{2}\text{erfc}^{-1}(2\Gamma)} \tag{6.38}$$

From this equation we can see that the minimum detectable strain amplitude for a given confidence level Γ will be a function of the frequency and will depend on the detector noise spectral density $S_n(f)$, which is a feature embedded in the data and is not search dependent, while the rest of the parameters $N, \theta_{thr}, CR_{thr}, T_{FFT}$, (and automatically p_0, p_1 which are functions of θ_{thr}) will be set accordingly to the type of search we are doing. In Section 7.6, we will use this formula to estimate the sensitivity for the directed search for the Galactic center.
For further details and or the complete calculations of the equations mentioned in this section see [30].

Part III

Astrophysics application

"Frankly, I jumped out of my chair the moment I saw what it meant. I have not the slightest doubt that you finally got the nucleus of our Galaxy!!"
W. Baade to J. L. Pawsey, as a reply to the mail containing the coordinates of the Galactic nucleus (1954)

Chapter 7

The Galactic Center search

In this chapter we discuss a case of study, applying the directed search pipeline, described in Chapter 6, to a real CW search. As mentioned in Sec. 4.2.2, a good candidate for a directed CW search is the Galactic Center (GC) region. A brief overview of the main components of the Galactic Center region is given in Sec. 7.1; the motivations for which the GC is a well suited target for those kind of CW searches are discussed in Sec. 7.2. In section 7.3 and 7.4, we will discuss about the setup and the choice of the parameters for this search. In section 7.5 we will show the main results of the search and an estimate of the search sensitivity is reported in section 7.6.

7.1 The Galactic Center area

The Milky Way galaxy is classified as a barred spiral galaxy according the Hubble classification criteria [47]. Its structure is composed by a nucleus surrounded by a central bulge and a thin disk formed by four main spiral arms [39]. Around the galactic plane, globular clusters orbit around, within the surrounding galaxy halo.
In 1950s two young radio astronomers J. G. Bolton and R. X. McGee, discovered the Galactic nucleus [63]. A previous work by H. Piddington, H. C. Minnett, identified a strong emitting source which lay close to the Galactic center they called Sagittarius A [79]. Only since 1974, after the discovery of a compact radio source deep within Sgr A, called Sgr A* [33], we are used to identify the Galactic center with the coordinates of Sgr A*.
Dynamical studies of the gas and matter, which are pulled into the center from the surroundings, is consistent with the presence of central super-massive black hole with a mass of 4 million solar masses [43], situated at 26.000 light years (8kpc) from Earth.
Although the central part of the Galaxy can't be observed in the visible spectrum, given the presence of large dust clouds, in addition to radio observations (e.g. VLA sky surveys [69]), infrared radiation (e.g. from the Spritzer Space Telescope with the GLIMPSE and MIPSGAL programs as in Sec. 5 of [94]), and high energy surveys (X-rays and γ-ray surveys from Chandra [48, 67], Fermi, H.E.S.S [38]), provide us a picture of the activities happening around the galactic central region (Figure 7.1).
The trace of of highly accelerated charged particles via non-thermal radio, X-ray and

γ-ray emission (synchrotron, bremsstrahlung, etc..) suggest the presence of cosmic accelerators such as Supernova remnants or Pulsar Wind Nebulae [35].
Figure 7.1 shows an infrared image from NASA's Spitzer Space Telescope of the Milky Way. The region shown in figure, spans 270 pc (horizontal) × 200 pc (vertical) around the Galactic center, old and cool stars are the blue dots, while massive stars and dust clouds are red. The bright spot at the center identifies the position of the super-massive black hole Sgr A*. The inner 50 pc central region of the Galaxy is often referred as the Sagittarius A complex. This area, as shown in Figure 7.2a, is composed by 3 main overlapping parts: the supernova remnant Sagittarius A East, which is the largest area; the spiral structure Sagittarius A West, located off-center within East; and finally the very bright compact source, Sagittarius A*, placed at the center of Sgr A West and hosting the super-massive black hole. The supernova remnant Sagittarius A East is a shell-like structure, located within few parsecs of the Milky Way's center. The overabundance of heavy elements in the Sagittarius A East region, suggest a supernova type II explosion of a massive star which took place $\sim$ 10.000 years ago. Figure 7.2b below is from the Very Large Array, and it shows that in the central few parsecs there is a rotating three-arm gas spiral structure (Sgr West), surrounding the central point source (Sgr A*), mainly composed by dust and ionized and atomic gas [54].
The coordinates of the point source Sgr A*, are (J2000.0)

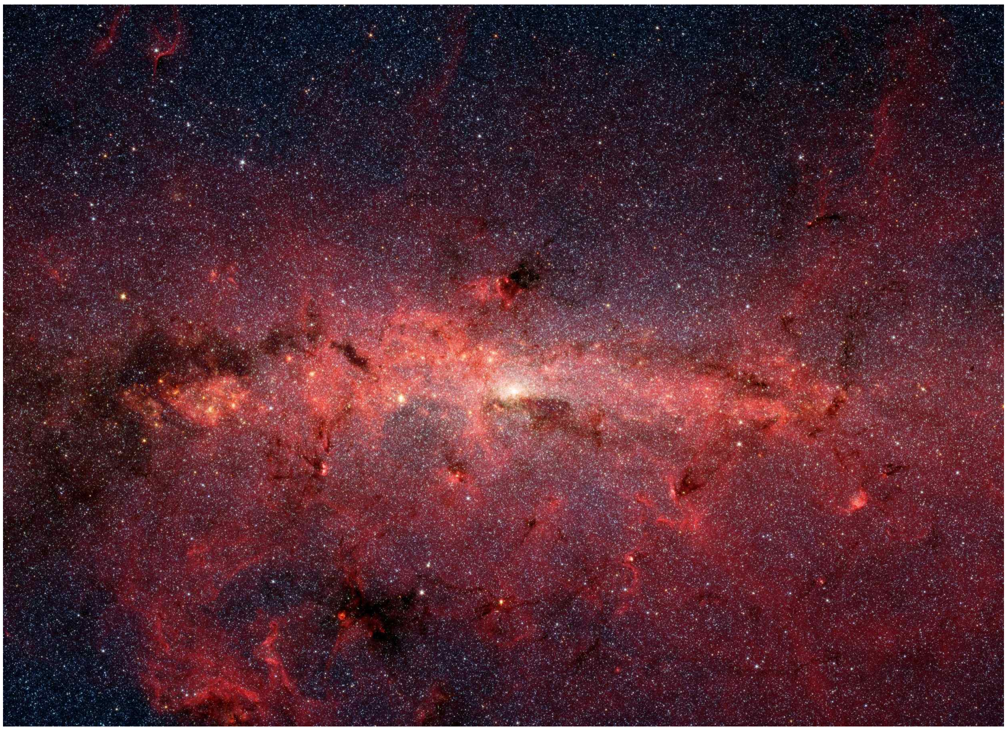

Figure 7.1. Infrared image from NASA's Spitzer Space Telescope of the Galactic Center region. Hundreds of thousands of stars are gathered around the center of the Milky Way. Credit: NASA/JPL-Caltech/S. Stolovy (SSC/Caltech)

$$\text{right ascension}\ (\alpha_{GC}) = 17\text{h}\,45\text{m}\,40.036\text{s}$$

$$\text{declination}\,(\delta_{GC}) = -29^\circ\,00'\,28.17''$$

and are coincident with the dynamical center of the Milky Way.

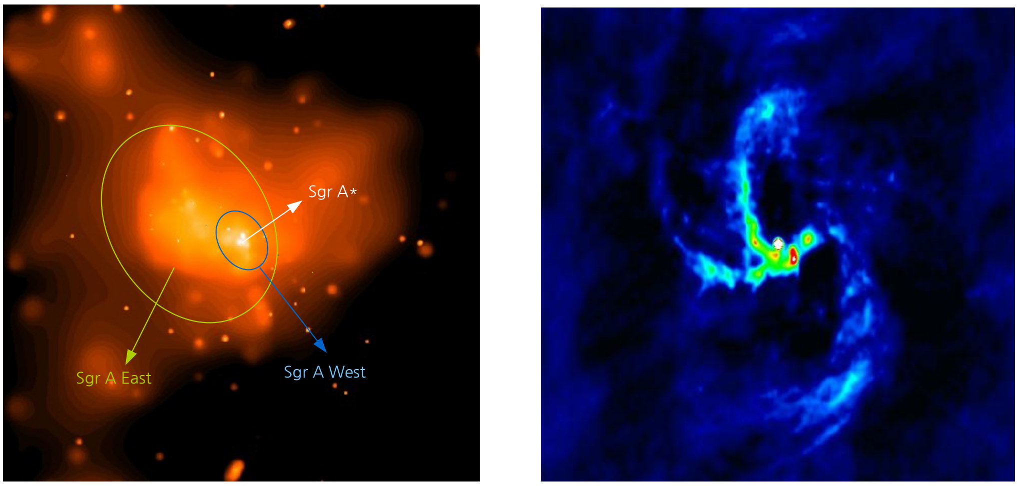

(a) Chandra X-ray image of 0.14° across the Sagitarius A area. Credit: NASA /Penn State /G.Garmire et al.

(b) NRAO VLA radio image of 0.0284° across Sgr A West. Credit: Roberts et al. NRAO / AUI / NSF

Figure 7.2. In the left picture the Sgr A East supernova remnant surrounds Sgr A*, the central black hole in the Galaxy. On the right a zoom on the Sgr A West mini-spiral.

7.1.1 GC neutron star population

The Galactic center region is known to contain a dense and luminous star cluster, along with the super-massive black hole, harboring very young and compact stars [86],[36],[95]. Recent results from X-ray surveys [67, 48], show the presence of point like sources such as the Cannonball pulsar candidate [76] (which support the SNR nature of Sagittarius A East), and several luminous X-ray binaries. Based on the large number of massive stars it is widely expected that the central parsec host a large neutron star population [77] ,[36], and in particular a big fraction is thought to be millisecond pulsars (MSP) [59, 58], the presence of which could explain the Galactic Center GeV excess measured by Fermi [34]. As discussed in a recent work [80], $O(100)$ pulsars are expected to emit in the Earth direction and an upper limit presence of $O(1000)$ MSPs is placed, which is compatible with the results found in [37]. This lack of pulsar detection in the central region of the Galaxy, is often referred as the "missing pulsar problem".

In addition to those classical pulsars, the Galactic Center region is potentially hosting several magnetars within a parsec from Sgr A*, as stated by [68] and further confirmed by the identification of the magnetar SGR J1745-2900 outburst in 2013 [81], [96]. This magnetar is the closest neutron star to a super-massive black hole ever detected, at a ~ 0.1 pc distance from Sgr A*.

For the aim of this work we are interested in the Galactic Center population of both electromagnetically silent neutron stars and pulsars. Given the high stellar density of the central cluster ($> 10^6 M_\odot\,\mathrm{pc}^{-3}$[65]), the galactic center region, restricted to the nearby area of the SMBH SgrA*, is a plausible target for a continuous gravitational wave search for signals emitted by asymmetric rotating neutron stars.

7.2 Motivation for a GC search of CW signals

From an astrophysical point of view, the GC region represents an open problem given the lack of detected pulsars, despite the fact that the number of expected sources is of the order of ~ 1000. The problem arises probably because of the scattering environment present in the GC, which makes it very difficult to detect pulsars using EM waves. In addition if we consider that there exist some detected magnetars close to the GC [96],[52], which are believed to represent a small fraction of all radio pulsars (at least in the rest of the Galaxy), this lack of normal pulsars is strange.

Present pulsars surveys are not able to detect a big part of the pulsar population in the GC, which is likely dominated by MSP. Those type of sources are likely to be formed in very dense stellar clusters, thus the GC dense stellar environment can produce those very fast spinning neutron stars.

Gravitational waves can potentially solve the problem, facing the problem of the "missing pulsars" at the GC. Indeed, since the gravitational wave interaction with matter is almost null, the GW emission from NSs in this region (both isolated and in binary systems), could be detected by current interferometers (especially in future scientific runs) and from future generation instruments such as the Einstein Telescope [85]. The detection of GW from isolated silent neutron stars, magnetars, accreting X-ray binaries and other neutron-star like systems, would provide crucial information on the structure and environment of the GC.

In particular the "interesting" galactic region is compacted in few pc around Sgr A*. For this reason, the search can be narrowed to a single sky point in our search grid (see sec. 7.4.3), given by the coordinates $(\alpha_{GC}, \delta_{GC})$. From a computational point of view, a directed search is less expensive than an all-sky search, but at the same time we can afford to explore a significant volume of the parameter space, bigger than the case of targeted or narrow-band searches (See Sec. 4.2). Finally, we picked the Galactic Center as a first benchmark of the new developed BSD framework, taking this application as a starting point for a future generalization to the case of blind all-sky searches.

The last directed search pointing to the Galactic Center, has been carried out using LIGO's fifth science run (S5), that occurred from 2005 through 2007 [2].

7.3 The BSD Galactic Center search setup

For this search we analyzed the first six months of Observational Run O2, C01 calibrated version, of the two LIGO interferometers (H1, L1). We used the standard BSD file format (10 Hz and 1 month), built as described in Chapter 5. The total number of BSD files used for this search is 708, spanning $N_{band} = 59$ frequency bands between 20 Hz and 610 Hz. The specific parameters used in this search are shown in Table 7.1 and Table 7.2. Since we need a sky position to start our directed search, we will point toward the direction of the super-massive black hole Sgr A*, assuming this sky point as the position of the Galactic center. The sky region spot corresponding to the sky bin at the position of Sgr A*, covers approximatively a radius ranging from 27 pc up to 123 pc (these approximate "radii" have been computed considering the number of frequency bins affected by the Doppler effect using the formulas 6.7, 6.8). The values reported in Table 7.3 have been obtained using the GC ecliptic coordinates $(\lambda_{GC}, \beta_{GC}) = (266.8517, -5.6077)^\circ$.

Table 7.1. Time spanned 6 months, frequency band investigates 600 Hz, and spin-down ($1.84 \cdot 10^{-09}$ Hz/s) band size investigated in this search.

Time	30.11.2016 h 15:17:03 to 01.06.2017 h 00:18:53
Frequency	$[20, 610]$ Hz
Spin-down	$[-1.8 \times 10^{-9}, 3.7 \times 10^{-11}]$ Hz/s

Table 7.2. Main parameters used: T_{coh} is the time baseline of the FFTs; N_{sd} number of spindown bins; we used the Sgr A* as sky position for our directed search analysis. The values of T_{coh} and N_{sd} are different for each 10 Hz band.

T_{coh}	$[52426, 11626]$ s
N_{sd}	$[500, 111]$ sd bins
Sky Sgr A*	RA(J2000) = 17h 45m 40.04s, Dec(J2000) = $-29^\circ\, 00'\, 28.1"$

7.4 Choice of the parameter space

In this search we are looking for continuous wave signals, coming from the Galactic Center direction. The sky point chosen is the sky position of Sgr A*. In this work we used a single sky cell, while the rest of the parameter space (frequency, spin-down), has been investigated using a parameter space grid.

In order to choose a proper setting, several constraints must be taken into account. First of all, a compromise between the sensitivity and the computational cost must be chosen.

Secondly, the choice of the parameter space must be taken as to maximize the chance of detection.

As explained in Sec. 4.2, in semi-coherent searches the parameter space is divided into smaller regions, and covered by a discrete template grid. In this section the main features of the parameter space setup, used for this particular case of study, are discussed.

7.4.1 Frequency grid

In this search the investigated frequency band ranges from 20 Hz to 610 Hz. This is the band where, given the sensitivity of the detector, we have the maximum chance of detection as discussed in [72]. We decide to discard the first 10 Hz frequency band covered by the detectors ([10-20] Hz), since data at such frequencies is very noisy and the sensitivity very poor. In general the most sensitive region of the detector band goes from 70 Hz to 200 Hz, and is usually referred as *bucket* region.

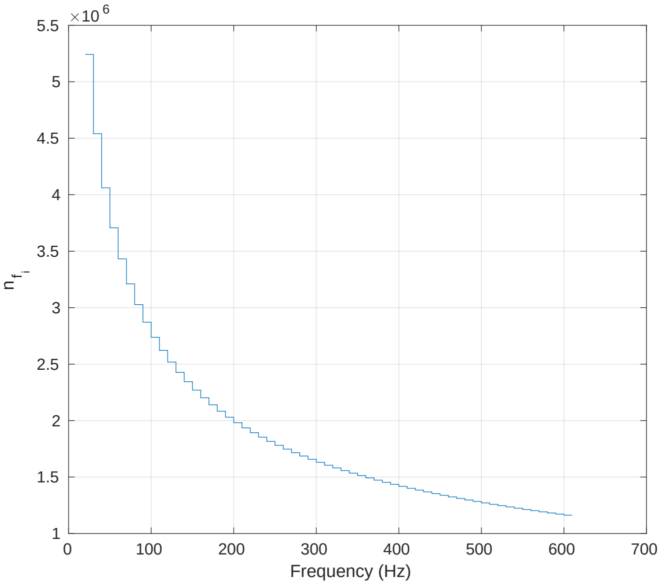

Figure 7.3. Number of frequency bins used for each 10 Hz frequency band between [20, 610] Hz. The maximum number of bins corresponds to an FFT duration of $T_{FFT} = 52426$ s with an over resolution factor $K_f = 10$.

The natural frequency bin step[1], is given by the inverse of the coherence time, which is the FFT duration T_{FFT}. For this search the FFT durations ranged from 52426 s at the lowest frequency to 11626 s for the band [600-610] Hz. The corresponding frequency bin steps are respectively 8.60×10^{-5} Hz and 1.91×10^{-5} Hz. An over resolution factor of $K_f = 10$ enters in the incoherent step of the analysis, as mentioned in sec. 6.3, increasing the number of frequency bins used in the search up to 5.2×10^6 for the band [20-30] Hz and 1.1×10^6 for the highest frequency band, as shown in Figure 7.3. The total amount of frequency bins (which is the sum of the bins used in each 10 Hz band) is:

$$N_f = \sum_{i=1}^{N_{bands}} n_{f_i} = 113655360 \tag{7.1}$$

where $n_{f_i} = K_f \frac{\Delta f_{BSD}}{\delta f} = 10 \times (10\,\mathrm{Hz})\, T_{FFT_i}$ is a function of the coherence time used in each band.

7.4.2 Spin-down grid

The spin-down resolution has been chosen considering the spin-down values which are typical for those kind of gravitational waves. The spin-down spans the interval $[-1.8 \times 10^{-9}, 3.7 \times 10^{-11}]$ Hz/s, where a small range of positive spin-down values $[0, 3.7 \times 10^{-11}]$ Hz/s has been included, in order to search for an eventually spinning up source. The maximum number of spin-down bins used is 500 for the frequency band [20-30] Hz (See Figure 7.4).

---

[1] Natural in the sense of the Fourier transform discretization.

A different choice would have been to fix the number of maximum spin-down bins (e.g. 500), for each band, with a consequent larger spin-down range covered at higher frequencies.

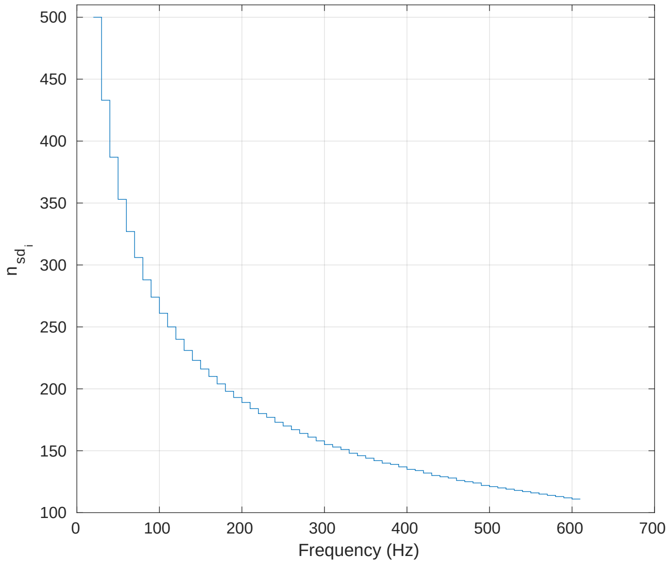

Figure 7.4. Number of spin-down bins used for each 10 Hz frequency with range [20, 610] Hz. The spin-down range covered is $[-1.8 \cdot 10^{-9}, 3.7 \cdot 10^{-11}]$ Hz/s. The highest value correspond to the maximum coherence time.

From a computational point of view the first option is better especially because rotating neutron stars with high spin-down values are less likely to exist.

A rough comparison of the two setup (setup I: fixed number of spin-down bins vs setup II: fixed spin-down range) can be done. The total number of parameters in the first setup is given by:

$$N_I = \sum_{i=1}^{N_{bands}} (n_{sd_i} \times n_{f_i}) = 2.5117 \times 10^{10} \tag{7.2}$$

In the second case, since $n_{sd_i} = 500$ for all the bands, $N_{II} = 500 \times \sum_{i=1}^{N_{bands}} n_{f_i}$; we can compute the ratio of the number of parameters:

$$\frac{N_{II}}{N_I} = \frac{500 \sum_i n_{f_i}}{\sum_i (n_{sd_i} \times n_{f_i})} = 2.26 \tag{7.3}$$

In the second setup the number of parameters used is larger by a factor of 2.26, which would correspond to a proportional raise in the computational cost of the search.

Having a limited amount of available resources, the setup I has been preferred against the setup II. The timing of the jobs using the setup I is shown in Figure 7.5.

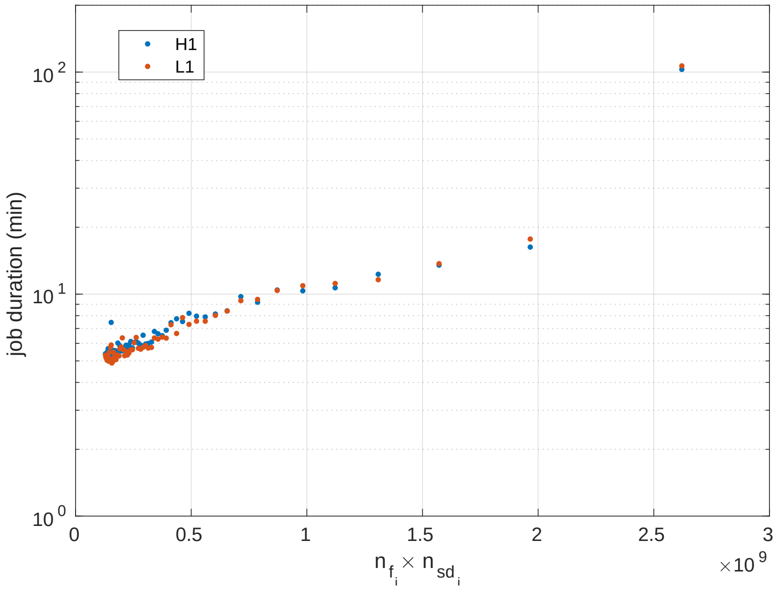

Figure 7.5. Timing of jobs vs number of parameters investigated for each 10 Hz band. The average job duration is 510 s (8.5 min). As can be seen from the plot, the job corresponding to the maximum value of the number of parameters, which correspond to the lower frequency band, is slightly off trend. Probably the job memory increased too much during the running, slowing the timing of the job.

7.4.3 Sky grid

As discussed in the previous section, a interesting number of potential sources of CW is located in the few inner parsecs of the Galactic Center. For this search a single sky bin is analyzed, centered at the position of Sgr A*. It is possible to roughly estimate how wide this sky bin is using Eq. 6.7, 6.8.
The values of $\Delta\lambda$ and $\Delta\beta$ computed for the sky coordinates $(\lambda_{GC}, \beta_{GC})$, are reported in Table 7.3.

Table 7.3. Values for $\Delta\lambda$, $\Delta\beta$ and R (see Eq. 7.4), computed for the minimum and the maximum frequency band covered in this search. A GC distance of $d_{GC} = 8$ kpc has been used to compute R which is an estimated "radius" for the sky patch covered by the search.

f_{max}	$\Delta\lambda$	$\Delta\beta$	R (at 8 kpc)
30 Hz	0.172°	1.75°	123 pc
610 Hz	0.038°	0.39°	27 pc

The estimated "radius" R has been computed as it is shown in Figure 7.6 with the following formulas:

$$R = \sqrt{R_\lambda^2 + R_\beta^2} \qquad \text{where:} \qquad \begin{aligned} R_\lambda &= d_{GC}\sin(\Delta\lambda), \\ R_\beta &= d_{GC}\sin(\Delta\beta). \end{aligned} \tag{7.4}$$

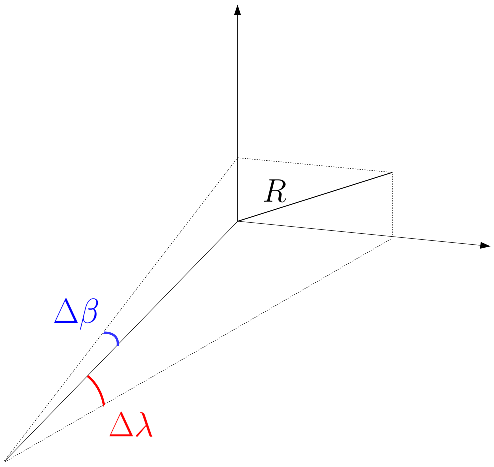

Figure 7.6. We can approximate the sky patch in $\Delta\lambda$ and $\Delta\beta$ as flat surface, since we are looking at the GC from our Earth position at $d_{GC} = 8$ kpc. In this way we can compute a *radius* around the center which defines a sort of distance far from the position of Sgr A*, in which we are potentially able to catch a signal.

This estimated radius does not take into account the direction between us and the sky point of Sgr A*; this means that we are in principle sensitive to all the signals coming from that direction, even if the emitting source is not located exactly at $d_{GC} = 8$ kpc.
As $R \gg 1$ pc a single sky patch is enough to cover the very central region of the Galaxy. In principle we could choose a bigger number of sky points, eventually narrowing down the rest of the parameter space. This second approach would bring us to a semi-directed search which, of course, can be easily implemented starting from this pipeline. For the purpose of this Thesis we are satisfied with a single sky patch.

7.4.4 Final parameter space

For each 10 Hz a final Hough map is obtained (as explained in Sec. 6.3), summing up the single Hough maps for each month, all referred to the same reference time t_0. Since we decided to cover a fixed range of spin-down values for each 10 Hz band, as already explained above, the maximum number of templates, is reached at the lowest frequency band, as can be seen in Figure 7.7.
An increase of the number of sky positions, keeping the same setup for frequency and spin-down grid, would have increased the computational cost of the search linearly. A different approach could have been applied, and it is similar to the one used in the follow-up stage of this search (explained in Section 6.5), where a smaller parameter space is explored, but many sky position around the candidate are investigated. It is clear that the optimal setup is strictly search dependent. For our purpose we wanted to search in a small sky region around the Galactic Center, with the possibility to explore a relatively wide frequency and spin-down range.

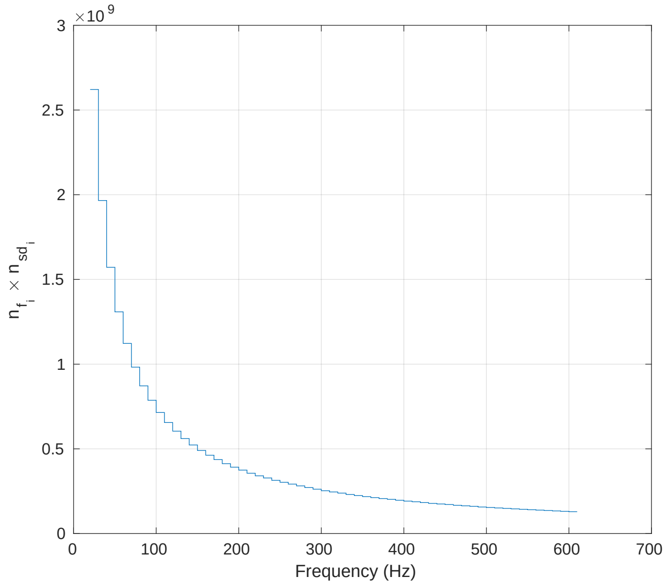

Figure 7.7. Total number of templates used for each 10 Hz frequency band between [20, 610] Hz. The maximum number of templates is $\sim 2.6 \times 10^9$ for the lowest frequency band.

7.5 Results

The 59 frequency bands have been analyzed using the pipeline described in Chapter 6, with a parameter space setup as described in previous sections. After the Hough transform has been computed for a given data set, covering 10 Hz and 6 months of data, we selected a first bunch of candidates.

7.5.1 Candidate selection

The resulting number of selected candidates is reported in Table 7.4. The number of "first order" candidates selected per each of the 59 frequency band is $N_{cand} = 300$, thus we have a number of candidates equal to $59 \times 300 = 17700$. This number has been chosen as a compromise between having a reasonable number of candidates to follow-up (in terms of computational load) and limiting the sensitivity loss due to the selection, which is higher the smaller is the number of candidates selected.
If we include also the "second order" candidates this number will be nearly doubled (See Table 7.4). The candidates are picked choosing the ones with highest significance on the FrequencyHough number count as mentioned in Section 6.4.

Table 7.4. Number of second order candidates and total number of "first order" plus "second order" (total) selected candidates for both datasets (L1,H1).

	2° order	Total
H1	17201	34901
L1	17247	34947

In Figures 7.8 we show the distribution in the spin-down/frequency plane of the selected candidates. Since we have fixed the number of candidates to select, we will have a concentration of candidates around small spin-down values in the lower frequency region, this effect is due to the annoying presence of combs of instrumental noise lines at lower frequencies.

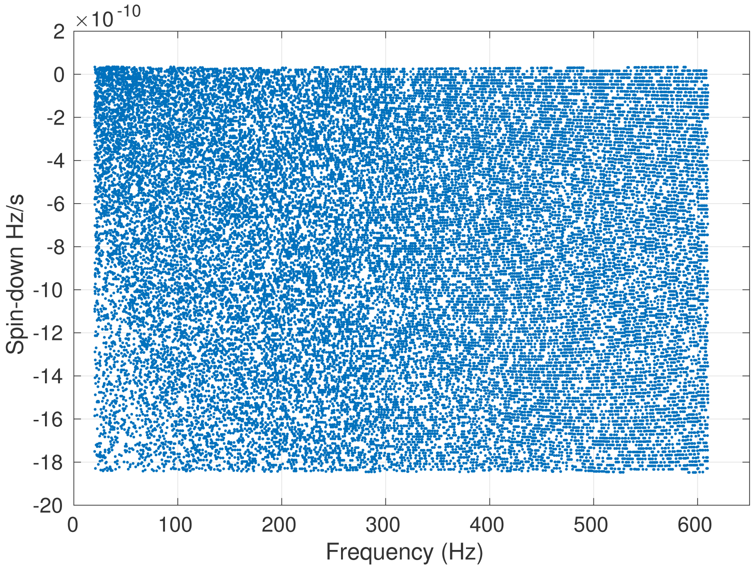

(a)

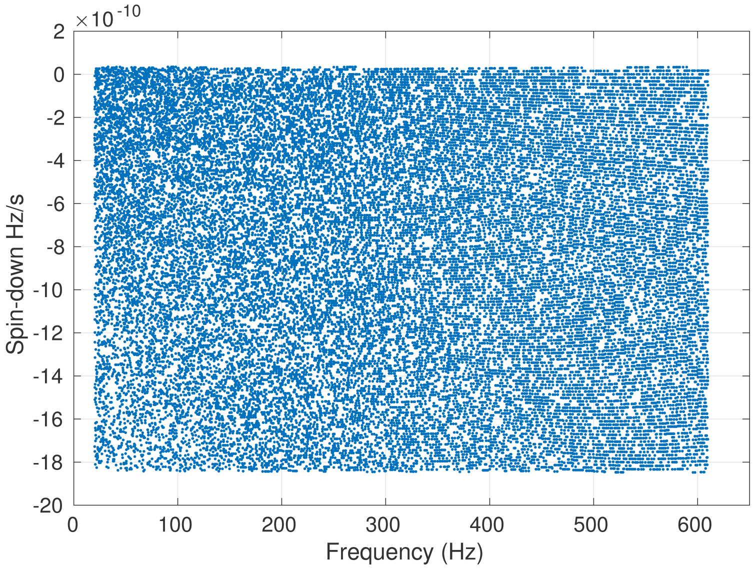

(b)

Figure 7.8. Distribution of the selected candidates over the spin-down/frequency plane. The accumulation of candidates with small spin-down and low frequency is due to the high pollution produced by noise lines and combs. A spectral line can appear as a CW signal with a zero or very small spin-down. **(a)** LIGO H; **(b)** LIGO L.

In Figures 7.9, candidate CR as a function of frequency is shown. Most of the observed high CR values correspond to known instrumental lines, like the 60 Hz power line and its harmonics. The lower part of the frequency band is polluted by the presence of several combs of lines, while regions around 300 Hz and 500 Hz also are very noisy bands because of the presence of suspension violin modes. The corresponding CR histograms are shown in Figures 7.10 and 7.11 where we can see that the mean value of the CR is around 5 in both detectors. Values of mean, median, mode and standard deviation are reported in Table 7.5.

Table 7.5. We report the main statistical parameters describing the CR distribution of the selected candidates computed from histograms in Figures 7.10,7.11. Here are reported the mean, median and standard deviation values of the distribution for both detectors.

	mean	median	mode	σ
H1	5.157	5.020	4.8	1.024
L1	5.125	5.019	4.8	0.863

7.5.2 Candidate coincidences

Following the procedure described in Section 6.4.1, we set the coincidence window equal to $d_c = 2$. Few coincident candidates survived (11) as reported in Table 7.6.

Table 7.6. Candidates survived to coincidences between the 2 datasets. Coincidence window used: $d_c = 2$. Some of those candidates are due to identified instrumental lines. Reference time is half of the run. We decided to discard from the list all the candidates showning a CR lower than a $CR_{thr} = 6.5$ (see Eq. 7.5).

candidates	Frequency (Hz)	spin-down (Hz/s)	CR	notes
cand 1	25.9975159	$-2.16 \cdot 10^{-10}$	8.13	to followup
cand 2	39.9960448	$6.51 \cdot 10^{-12}$	10.89	multiple of 10 Hz
cand 3	41.9959613	$-1,41 \cdot 10^{-10}$	7.90	to followup
cand 4	69.9952741	0	24.49	NoEMi line (H1)
cand 5	129.9923024	0	24.88	multiple of 10 Hz
cand 6	187.8227900	$-9,59 \cdot 10^{-10}$	5.03	$CR < CR_{thr}$
cand 7	274.8701237	$-1.55 \cdot 10^{-10}$	4.48	$CR < CR_{thr}$
cand 8	455.0785834	$-9.05 \cdot 10^{-10}$	4.70	$CR < CR_{thr}$
cand 9	499.2254261	$-6.44 \cdot 10^{-10}$	5.07	violin mode
cand 10	568.8886727	$-8.19 \cdot 10^{-10}$	4.92	$CR < CR_{thr}$
cand 11	593.0153869	$-1.22 \cdot 10^{-9}$	4.32	$CR < CR_{thr}$

Among those candidates some were easily discarded as produced by noise. In particular 2 out of 11 were due to known spectral lines, one produced by the suspension bench violin modes (cand 9), and the second one (cand 4), was discarded since a spectral line was present in the list of lines found by NoEMi (line monitoring tool described in Section 3.2) in one of the 2 detectors (H1). The line found by NoEMi (see Figure 7.12) has shown a coincidence with 2 auxiliary environmental channels the PEM_CS_MAG_LVEA_OUTPUTOPTICS_Z_DQ (70.6 %) and PEM_CS_MAG_LVEA_OUTPUTOPTICS_X_DQ (58.8 %), which are magnetometers (MAG) of the Physical Environmental Monitoring system (PEM), placed

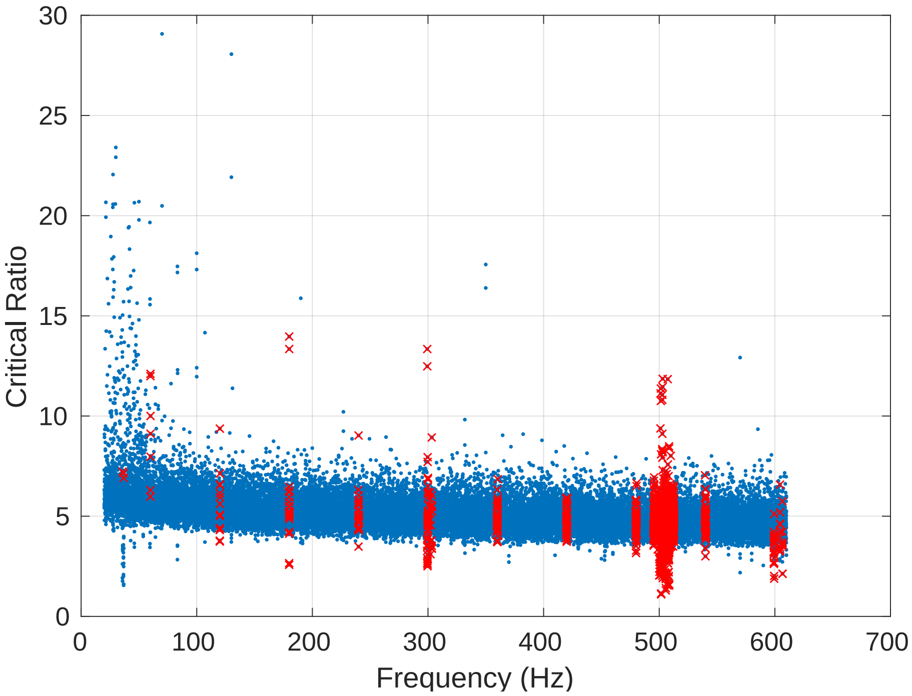

(a)

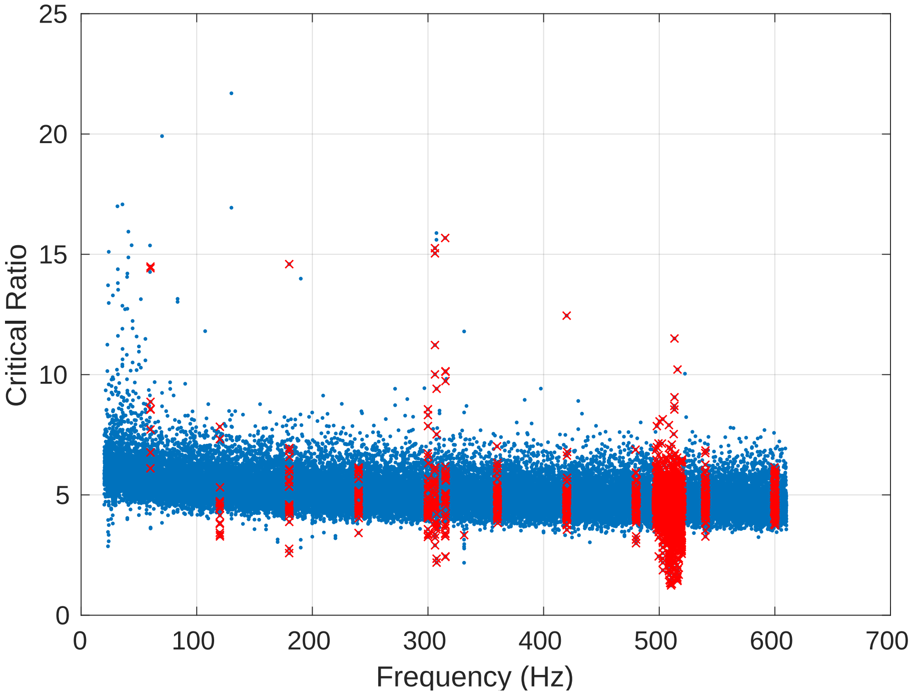

(b)

Figure 7.9. **(a)** LIGO H; **(b)** LIGO L. Distribution of the candidate significance (CR) in frequency. The most noisy bands present drops and jumps respect to the mean Critical Ratio value (5.157 for (a), 5.125 for (b)). The presence of lines which can mimic a CW signal, produces candidates with high CR. This feature is particularly evident at lower frequencies, where the data presents several instrumental lines and combs. Red × are the candidates correspondent to some well known instrumental lines. Candidates around ~ 300 Hz and ~ 500 Hz are due respectively to the beam splitter 1st harmonic violin mode and the suspensions 1st harmonic violin modes. The line observed around ~ 36 Hz in plot (a) is a calibration line. In both plots the 60 Hz power line and its harmonic are clearly present. The complete list of removed lines can be found in Appendix C.

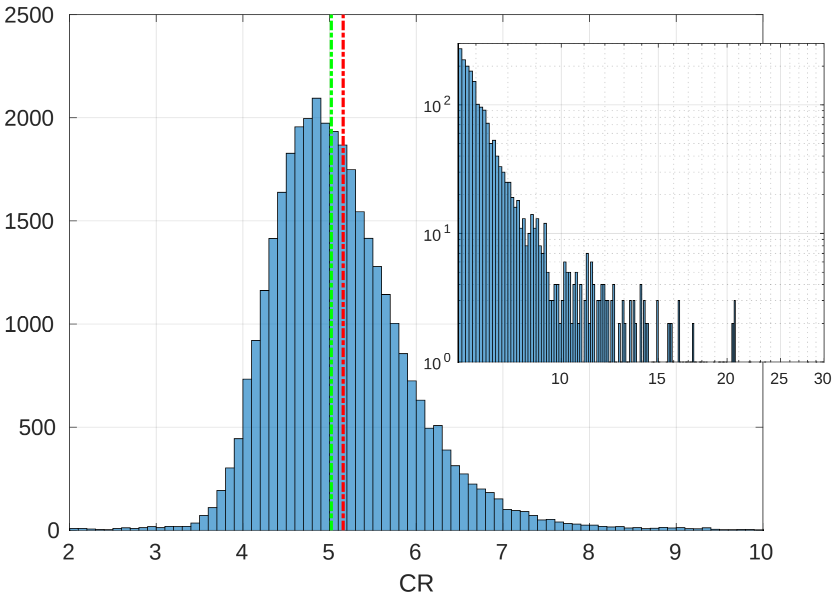

Figure 7.10. CR values distribution and zoom of the right tail of LIGO Hanford. Histogram bin width 0.1. The red dashed line is the mean, while the green one is the median.

in the (CS) Corner Station of the interferometer. Other 2 candidates (cand 2 and 5) were discarded since are close to a multiple of 10 Hz, probably hosting an instrumental line.

Once we have discarded those 4 candidates, another selection has been done, which consists in the selection of candidates with a CR bigger than a threshold CR_{thr}. This threshold has been set using the formula in Eq. 6.34.

We can invert Eq. 6.34 and plot the CR_{thr} as a function of the P_{fa} as shown in figure 7.13.

The P_{fa} corresponding to the selection of an average of one noise event above threshold is :

$$P_{fa} = \frac{1}{\sum_i (n_{sd_i} \times n_{f_i})} = 3.98 \times 10^{-11} \tag{7.5}$$

This brings to a value of the Critical ratio threshold of $CR_{thr} = 6.5$. Using this threshold we will keep only the candidates with a CR higher than this value, which correspond to select mainly the tail of the distribution in figure 7.10 and 7.11. With this threshold only 2 out of the starting 11 coincident candidates survived. It should be mentioned that the choice of the CR_{thr} is almost arbitrary. In particular this threshold is set in order to reduce the number of candidates to follow-up. In this case we wanted to focus only on the most significant candidates, but in other cases it is possible to avoid using it.

This selection on the CR could have been done before coincidences, and not after as we did. Anyway in terms of validity of the final result it doesn't have any effect.

Although no line has been found in coincidence with those two surviving candidates,

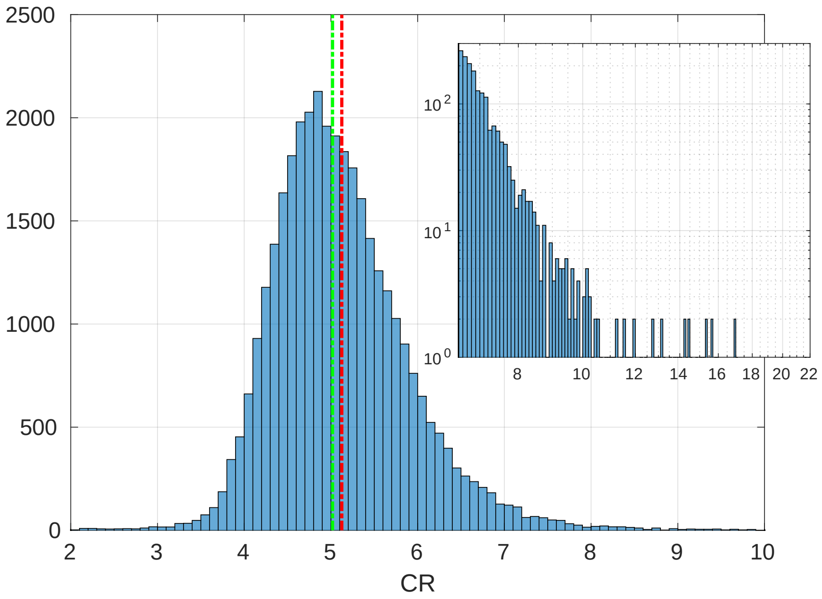

Figure 7.11. CR values distribution and zoom of the right tail of LIGO Livingston. Histogram bin width 0.1. The red dashed line is the mean, while the green one is the median.

their frequencies are suspiciously close to "round" frequencies. This suggests they are likely instrumental artifact. In order to confirm this hypothesis, we performed a follow-up around a small portion of their parameter space, using the procedure described in Sec. 6.5.

7.5.3 Candidates follow-up results

For each coincident candidate, we extracted a new BSD from the BSD database, centered around the candidate frequency, covering 1 Hz band and spanning 6 months. This BSD has been corrected using the parameters of the candidate. From this corrected time-series a new peak-map with FFTs 10 times longer, has been created. As explained in step 5. of section 6.5, from this peak-map we build the "overall peak-map" which is an ensemble of sub-peak-maps corrected for the nearby sky points of the follow-up grid. This cumulative peak-map is the input of the Multi-Hough map

The follow-up volume

We set the follow-up volume parameters as reported in Table 7.7. As explained in section 6.5, from the starting peak-map we select all the peaks contained in the frequency bandwidth (Δf_{fu} see Eq. 6.13) centered at the candidates frequency. The frequency bandwidth Δf_{fu} is different for each detector as shown in Table 7.7. This is due to the different locations of the detectors, which produce a difference in the

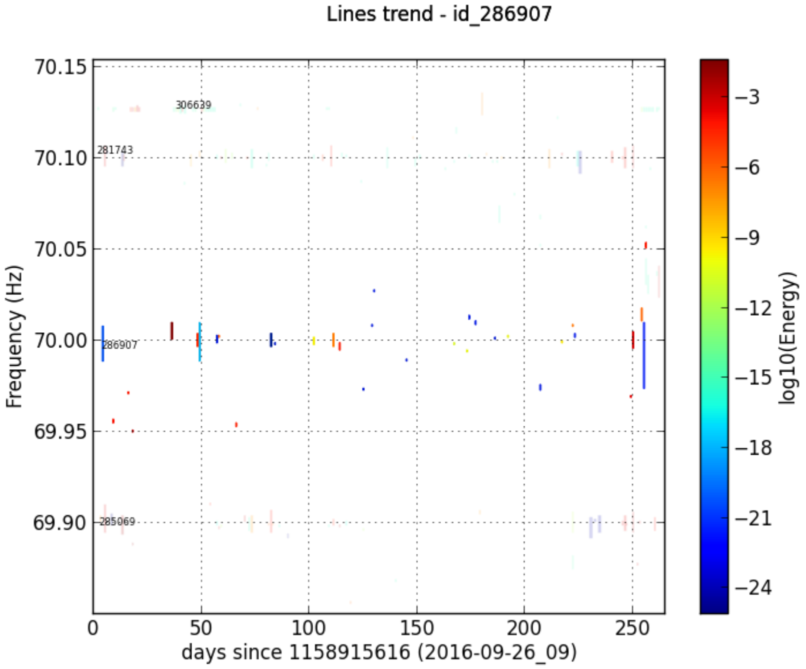

Figure 7.12. NoEMi summary plot around the frequency band of the candidate near 70 Hz. The plot show the trend of the identified line (ID 286907) which has been present from before the beginning of the O2 observational run.

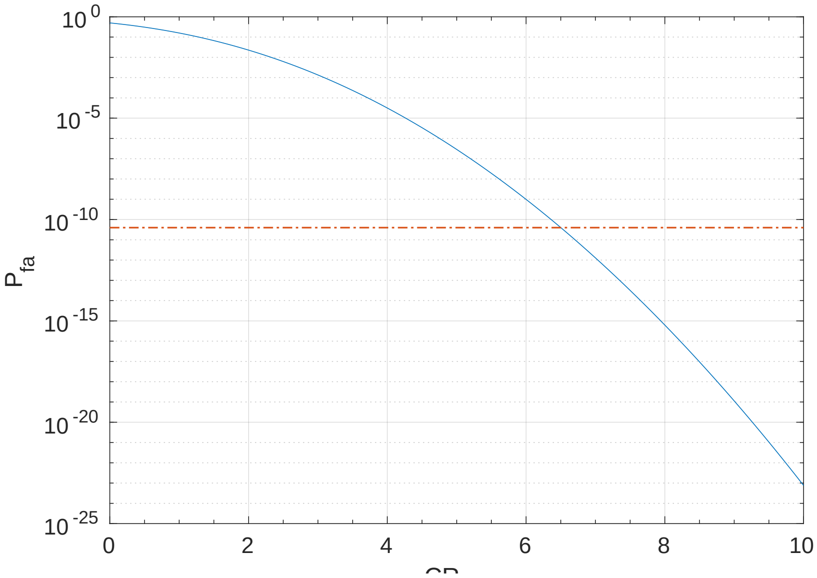

Figure 7.13. False alarm probability as a function of CR_{thr} (See Eq. 7.5). The red line corresponds to the probability of picking an average of one candidate over the total number of parameter space templates.

Doppler residual velocities.

The number of frequency bins used at this stage, can be computed as $n_{f_{fu}} = \frac{\Delta f_{fu}}{\delta f_H}$, where δf_H in this case will be the ratio between the enhanced frequency bin δf_{ref}, and the $K_f = 10$ over resolution factor of the Hough map.

Concerning the spin-down range, this covers 2 initial coarse bins, which correspond to ±20 refined spin-down bins around the candidate spin-down value, with a total of 41 refined spin-down bins used for the follow-up. Since we have corrected the initial peak-map using the candidate parameters, the spin-down values used will be centered at zero and will cover a residual spin-down of $\pm 1.1662 \times 10^{-12}$ Hz/s for candidate 1 and $\pm - 2.9537 \times 10^{-12}$ Hz/s for candidate 3, covering a total band of twice this minimum residual spin-down.

The widths of Δf_{fu} and $\Delta \dot{f}_{fu}$ set the size of the sub-peak-map used for the creation of the "overall peak-map".

The sky patch used for the construction of the refined sky grid is 1.5 times larger than the initial coarse sky bin (as shown in Figure 6.7). This new sky patch has an over resolution factor of 4. The total number of sky points used in the follow-up is equal to $13 \times 13 = 169$, with 13 values of λ and 13 values of β. $\Delta\lambda_{fu}$ and $\Delta\beta_{fu}$ are the refined steps between two points along λ and β in the new sky grid.

Table 7.7. Followup volume used for each of the candidates in the followup (cand 1 and 3). Δf_{fu} is the band of the selected peaks, $n_{f_{fu}}$ is the number of frequency bin used. This number is different for each detector since the band selected is slightly different. The spin-down range $\Delta \dot{f}_{fu}$ is centered at zero spin-down value and has been divided in 41 bins. The followup has been done using 169 nearby sky points with a step in λ and β as reported.

candidates	Δf_{fu} (10^{-5} Hz)	$n_{f_{fu}}$	$\Delta \dot{f}_{fu}$ (10^{-12} Hz/s)	$n_{\dot{f}_{fu}}$	$\Delta\lambda_{fu}$	$\Delta\beta_{fu}$	$n_\lambda \times n_\beta$
cand 1	3.600 (H) 3.411 (L)	201 (H) 190 (L)	2×1.1662	41	0.005°	0.258°	13×13
cand 3	4.817 (H) 4.505 (L)	212 (H) 198 (L)	2×2.9537	41	0.004°	0.228°	13×13

Once the "overall peak-map" is ready, we compute the Multi-Hough map containing all the single corrected Hough maps; On this we select the candidate corresponding to the maximum number count.

Refined candidates

This new refined candidate will have in principle a better estimated set of parameters, which are reported in Table 7.8. In order to confirm or discard the candidate we need to quantify if it is more significant than the starting one. We can compare the two by computing a sort of significance (CR_{hist}) from the peak-map frequency histogram, as follows:

$$CR_{hist} = \frac{n_{hist} - \mu_{hist}}{\sigma_{hist}} \tag{7.6}$$

where μ_{hist} and σ_{hist} are the mean and standard deviation of the histogram, while n_{hist} is the maximum number count found in ± 1 coarse frequency bin around the candidate. The histograms are done using peak-maps corrected with the parameters of the coarse candidate (before the follow-up) and the refined one.

Table 7.8. Parameters of the refined candidates after the followup.

refined candidates	frequency (Hz)	spin-down (Hz/s)	sky $(\lambda, \beta)^\circ$
cand fu 1 H	25.9975094	2.165×10^{-10}	(266.847, -6.898)
cand fu 1 L	25.9975178	2.149×10^{-10}	(266.824, -7.156)
cand fu 3 H	41.9959541	1.419×10^{-10}	(266.874, -6.977)
cand fu 3 L	41.9959414	1.403×10^{-10}	(266.863, -4.238)

Since we expect that the refined candidate has been picked over a refined grid of parameters, hence we have an higher sensitivity, in case of a real signal, we will see an increase of the CR_{hist} in the histogram of the peak-map corrected with the refined parameters.

In Figures 7.14 and 7.15, we can see the plot of the histograms described above, while the mean parameters of the histograms are reported in Tables 7.9 and 7.10. From the histogram we don't see any significant increase of the CR, which supports the noise or instrumental origin of both candidates.

Table 7.9. CR, mean and standard deviation computed for candidate 1. The mean level of L1 is lower compared to the mean level of H1. This suggest that the candidate found in coincidence was mainly due to a disturbance or noise fluctuation in H1. The critical ratio values in both detectors don't show any significant increase after the followup.

candidate 1	CR_{hist}	μ_{hist}	σ_{hist}
H coarse	3.472	26.081	5.737
H refined	3.466	26.092	5.743
L coarse	0.320	10.794	3.768
L refined	0.058	10.780	3.782

Table 7.10. CR, mean and standard deviation computed for candidate 3. Also for this candidate the critical ratio does not show any significant increase. The increase of the CR in L1 refined candidate is not compatible with the increase expected in case a real signal is present.

candidate 3	CR_{hist}	μ_{hist}	σ_{hist}
H coarse	3.408	27.512	6.011
H refined	3.412	27.483	6.013
L coarse	1.324	22.021	5.272
L refined	1.698	22.017	5.290

Candidate 1

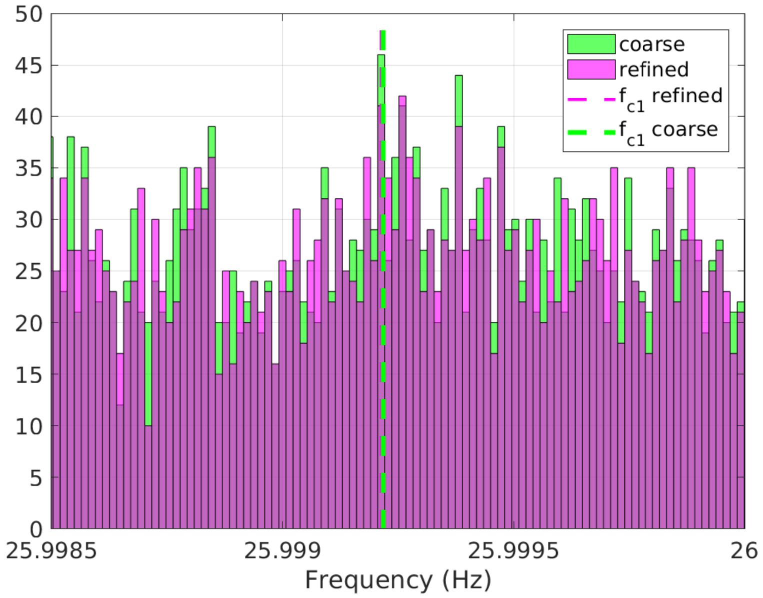

(a)

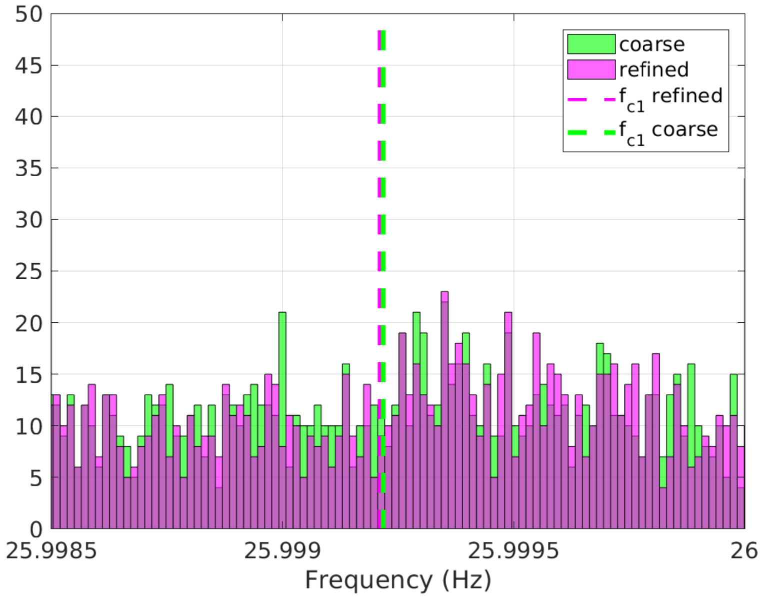

(b)

Figure 7.14. Frequency histogram of the peak-map corrected using the parameters of the coarse candidate (cand 1 in green), and corrected using the parameters of the refined candidate (refined cand 1 in magenta). (a) plot obtained from LIGO Hanford data; (b) plot obtained from LIGO Livingstone data; the dashed lines are the position of the frequencies of the candidates at the reference time MJD 57722.64 (beginning of the run).

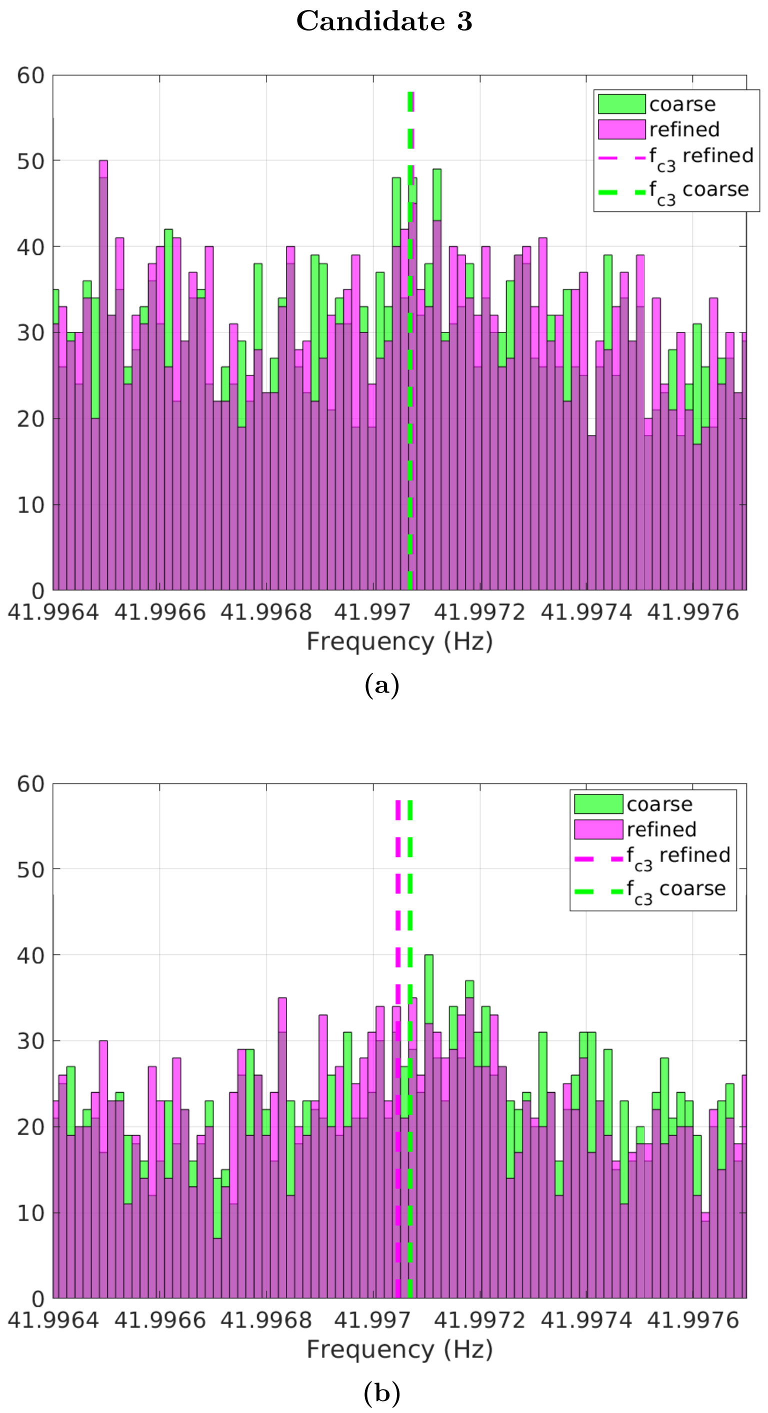

Figure 7.15. Frequency histogram of the peak-map corrected using the parameters of the coarse candidate (cand 3 in green), and corrected using the parameters of the refined candidate (refined cand 3 in magenta). (a) plot obtained from LIGO Hanford data; (b) plot obtained from LIGO Livingstone data; the dashed lines are the position of the frequencies of the candidates at the reference time MJD 57722.64 (beginning of the run).

Discussion and verification steps

We want to further verify the noise origin of those surviving candidates. First of all, as suggested from Figures 7.15, candidate 1 is probably due to a line present only in Hanford detector. To confirm this hypothesis we can take a look to the *persistency* distribution plot of the peak-map before and after the Doppler correction is applied (Figure 7.16). The persistency is defined as the number of FFTs in which a peak at a given frequency bin is present, normalized to the number of FFTs analyzed.

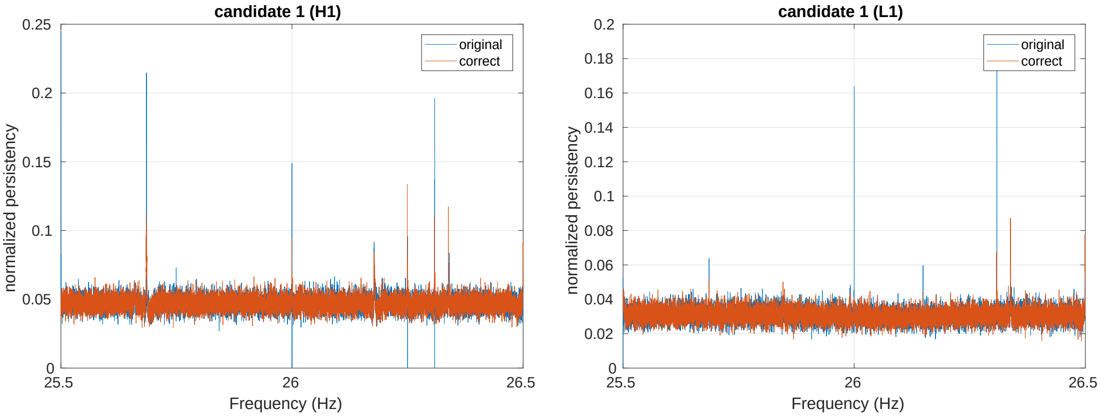

Figure 7.16. Comparison between persistency plot before and after the Multi-Doppler correction is applied for candidate 1. From the results of the follow-up we were expecting to see a persistent line only in Hanford after the correction.

Furthermore, if we check the CR values of the single candidates from each detector which have produced the coincidence, the values are 10.14 (H1) and 6.14 (L1). Since the sensitivity of L1 is better than the one for H1, we would have expected an higher CR for L1 candidate in case of a real signal.

What happen for candidate 3 instead is not so trivial. We can take a look again to the persistency plots in Figure 7.17 and check the values of the CR before coincidences, which in this case are both higher than the CR_{thr} (9.48 (H) and 7.64 (L)). What we can see is that after the Multi-Doppler correction the line at 42 Hz moved to the left producing the candidate we found in coincidences.

Those 2 coincident candidates are an example on how much data quality is critical for those kind of signals. In particular DetChar studies about lines, for which a lot of time and manpower is needed, are currently ongoing and the list of identified lines to be removed from O2 data, is still a work in progress.

As mentioned before the follow-up section, we knew from the beginning that those candidates were too "strangely" close to round frequencies, and were probably due to noise lines. This thesis has been confirmed by the study of the persistence.

7.6 Sensitivity of the search

Finally, although we discarded all the coincident candidates, we can compute the sensitivity of the search as discussed in section 6.6.5. We will use the Equation in formula 6.38 to estimate the minimum detectable strain $h_{0,min}$. This estimate has

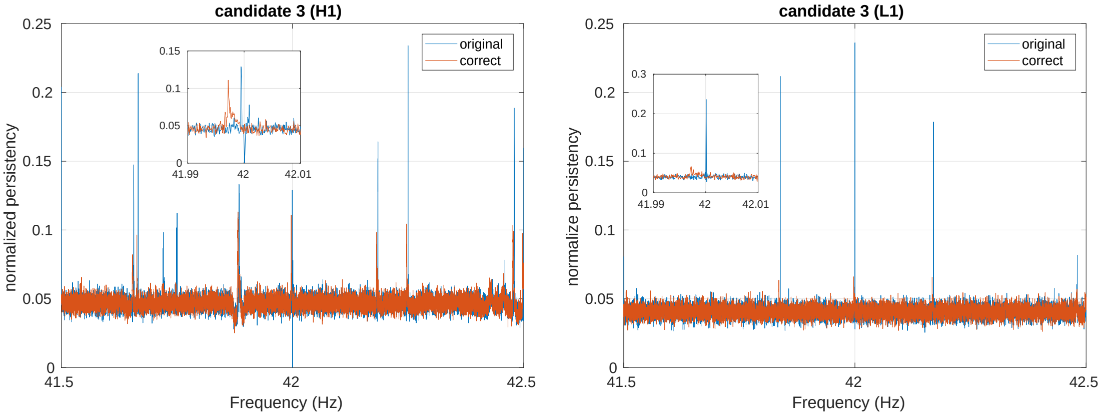

Figure 7.17. Comparison between persistency plot before and after the Multi-Doppler correction is applied for candidate 3. In Livingston is a line clearly present at 42 Hz plus 2 sidebands. After the Multi-Doppler correction the line at 42 Hz moved to the left producing the candidate we found in coincidences.

been computed for each 1 Hz band covered by the search. The minimum detectable strain will be a function of the frequency and will depend on the CR_{thr} we used in the search. We took as T_{FFT} and N (number of FFTs used), the correspondent values used in each 1 Hz band (which are the same per each 10 Hz band).
The resulting sensitivity curve estimation, which has been done for a confidence level of 95 % is reported in Figure 7.18

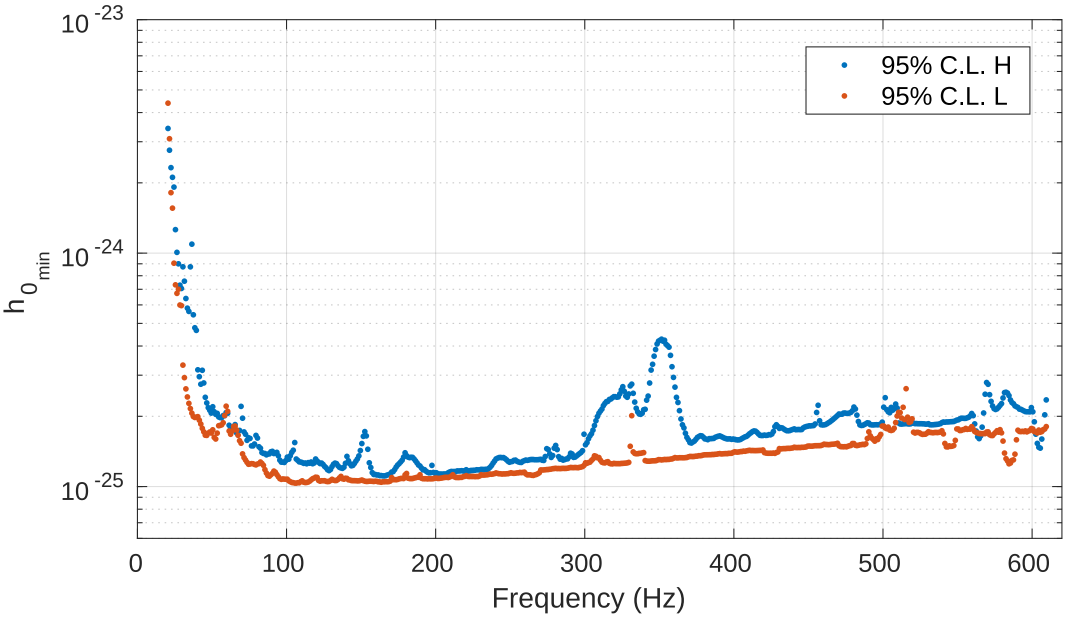

Figure 7.18. Sensitivity estimate with a 95% C.L. The best sensitivity value is reached around 110 Hz an is about $\sim 1 \times 10^{-25}$

The lower sensitivity value is reached around 110 Hz is of about $\sim 1 \times 10^{-25}$ which in principle is slightly better than the result found in [2]. In fact, we can only do a mild comparison with the last GC directed search [2], where the tightest upper limit (computed at 90% confidence level) corresponds to $\sim 3.35 \times 10^{-25}$. It is not possible to directly compare the two results since we have computed a sensitivity estimate at 95 % C.L, instead of an upper limit at 90 % confidence level. Furthermore, the setup of the searches was not the same, and in particular the coherence time used and the sensitivity of the two runs (O2 and S5) are different. We can compare the computational cost of the two searches, opportunely rescaling the number of templates and the total computational time used. As a result we have that our search is at least 10 times faster than the one described in [2].

Using the relationship between h_0 and the ellipticity ϵ (see Eq. 1.8) we can compute the corresponding minimum value for it as shown in Figure 7.19. The minimum ellipticity is $\sim 2.77 \times 10^{-6}$ at highest frequencies. Since the maximum predicted ellipticity for a "standard" neutron stars is a few times 10^{-6}, we can exclude the presence of maximally strained NS in the galactic center. In future runs, where the sensitivity will be improved, we expect to increase our chance of detection and place more constraints on the ellipticity of those compact objects.

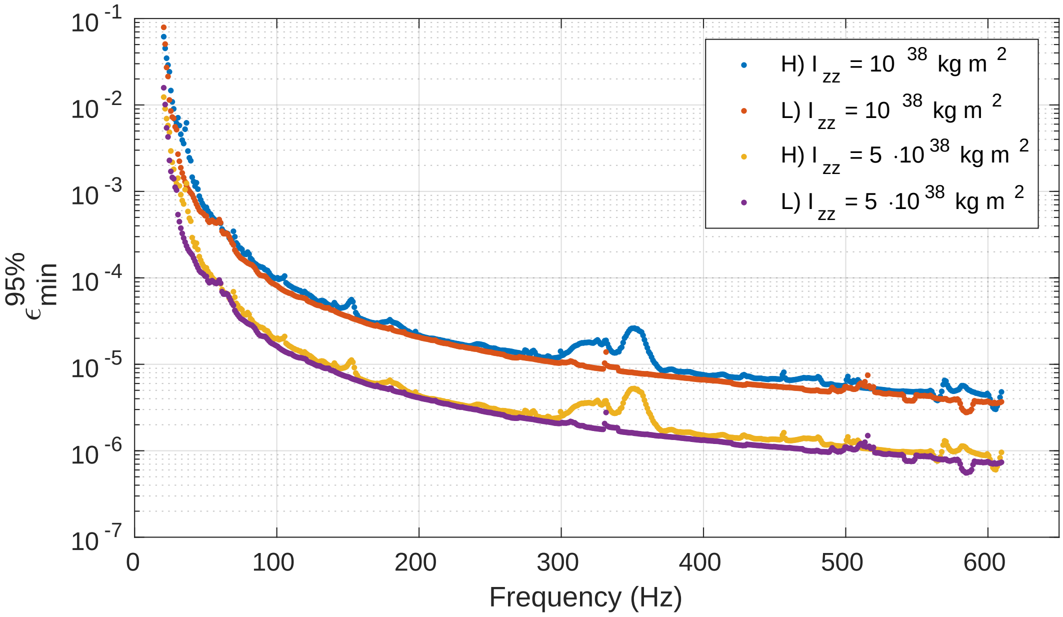

Figure 7.19. Estimates of the minimum detectable ellipticity using two values of I_{zz} expected for "standard" neutron stars (blue and red dots) and more exotic compact objects (purple and yellow dots). The plot show the ellipticity of a source in the few inner parsecs of the Galactic Center detectable by this search.

Conclusions

In this Thesis several aspects related to the search for gravitational waves have been tackled. In the first chapters, after an introduction to gravitational waves and to interferometric detectors, I described part of the big effort that is behind the scene of gravitational wave data analysis and, in particular, I focused on the spectral noise investigation, which is a crucial part of the data quality studies, and on which I have been deeply involved in the last three years. The identification of noise spectral disturbances (often called *noise lines*) through the use of suitable investigation and monitoring tools, plays a significant role in real searches, helping in discarding potential signal candidates and flagging portion of the parameter space which are not well suited for the analysis due to the presence of noise artifacts. In addition, noise line studies are important during detector commissioning as they help to identify noise sources which removal improves the detector sensitivity.

The second part of this Thesis is dedicated to the development of a new data organization framework, called Band Sampled Data collection, which simplifies and makes much more flexible all the data machinery needed in searches for continuous gravitational wave signals. It allows "on-the-fly" manipulation of the data, tailored to the type of signal the user wants to search for. This framework will have an important impact, in terms of analysis speed and flexibility, on most of the continuous wave searches. Indeed, many of the search pipelines developed by the Rome Virgo group will be adapted to the new framework in the near future. Moreover, it will be also useful for the development of search procedures for different kinds of signals. I am currently writing a paper containing a detailed description of the Band Sampled Data collection and examples of its use.

In order to test some of the potentialities of this framework, a brand new directed pipeline has been developed, building on some techniques used in previous continuous wave searches. This pipeline has been applied to a real search for CW signals from the few innermost parsecs of the Galactic Center region, using data of the second science run of LIGO (O2). This is the first time the Rome group performs a directed search. More generally, this is also the first directed search toward the Galactic center conducted on advanced detector data by the LIGO and Virgo Collaborations. No gravitational wave signal has been found and I have estimated the sensitivity of the search in terms of the minimum detectable amplitude strain, $h_{0_{min}}$. The best (i.e. lower) sensitivity value is reached around 110 Hz and is of about $\sim 1.03 \times 10^{-25}$. The sensitivity can be translated in the minimum ellipticity of potentially detectable sources. The best results are obtained at the highest frequency range and correspond to a minimum ellipticity of $\sim 2.77 \times 10^{-6}$, which is comparable to the expected maximum ellipticity of a "standard" neutron star and significantly smaller than the maximum ellipticity foreseen by more exotic equation of states (e.g. quark stars). In practice this means that we are potentially sensitive to the emission of CW signals also from NS with exotic EOS. A paper containing the results of this search will be written soon.

Advanced LIGO and Virgo detectors are currently in a new phase of upgrades and should re-start data taking in Fall 2018 with an improved sensitivity. The pipeline I have developed will be applied to future new data (O3), targeting some interesting regions of the sky (like the Galactic center and supernova remnants). Given the improved sensitivity of the detectors it could bring to the first detection of continuous gravitational waves from spinning neutron stars. The detection of these signals will provide a lot of information on the structure, characteristics and demography of these fascinating compact objects.

Appendix A

The *cont* and *tfstr* structures

Example of a *cont* structure created for the follow-up stage of candidate 1 in Hanford detector as described in Sec. 7.5.3

```
cont =

  struct with fields:

             t0: 5.7723e+04
          inifr: 41.5000
          bandw: 1
           v_eq: [15382×4 double]
           p_eq: [15382×4 double]
           Tfft: 2048
            ant: 'ligoh'
            run: 'O2'
            cal: 'C01'
      tcreation: '27-Jun-2017 19:33:27'
    durcreation: 12.1755
     mi_abs_lev: 0.0038
           oper: [1×1 struct]
        sb_pars: [1×1 struct]
          tfstr: [1×1 struct]
```

Contents of the *tfstr* substructure is shown below:

```
tfstr =

  struct with fields:

    peaktype: 'array'
         ant: 'ligoh'
          t0: 5.7723e+04
          dt: 1
       inifr: 41.5000
    bandw: 1
     lfft: 11008
      dfr: 9.0843e-05
       DT: 5504
    gdlen: 15756800
    subsp: [1×1 struct]
       pt: [1×1 struct]
  bsd_par: [1×1 struct]
    clean: [1×1 struct]
```

This structure contains all the meaningful information about the cleaning of the BSD file, and the very short FFT spectrum used for this purpose. See [28] for details about the very short FFT spectrum.

Appendix B

Few BSD header functions

BSD creator

Code header for the creation code of BSD files:

```
sfdb09_2bandgds_BSD(SFDB_list,foldout,frmin,frmax,BSD_BAND,nfft,run,ant,calibration,sim)
% Example:
sfdb09_2bandgds_BSD('sfdblist.txt',pwd,60,80,10,200,'O1','ligoh','C01',0); --> use real d
%
%SFDB09_2BANDGDS  creates BSD gds
%
%   SFDB_list      input file list of SFDB
%   foldout      output BSD folder
%   frmin,frmax  operation range (depends on the number of BSD to manage simultaneously,
%                 (for one gd 210 MB are needed)
%   BSD_BAND     frequency bandwidth (and inverse of the sampling time)
%   nfft         number of fft to use (if it is bigger than the total number of ffts in a
%   run          e.g 'O1','VSR4'
%   ant          e.g 'ligoh', 'ligol', 'virgo'
%   calibration sting e.g. 'C00' or 'C01' indicates the calibration version
%
%   sim           =1 sinusoid simulation
%
%                 =2 real data+ sinusoid

% Version 3.0 - April 2016
%
% From Ornella Piccinni and Sergio Frasca
% Department of Physics - Universita' "Sapienza" - Rome
```

Time-frequency cleaning structure creator

Time-frequency second cleaning, computes persistency and time-frequency removal of disturbances

```
function tfstr=bsd_tfclean(tfstr,anabasic)
% time-frequency cleaning
%
%   tfstr=bsd_tfclean(tfstr,anabasic)
%
%  - tf filter
%  - persistence
%  - noise adaptive filter
%
%    tfstr         tf structure as created by bsd_peakmap
%    anabasic      procedure control structure
%       .pers_thr  persistence threshold (0 -> no threshold; typical 0.3)
%       .tfh_df    time-frequency histogram df
%       .tfh_dt    time-frequency histogram dt (days) def 0.5
%       .tfh_pht   time-frequency histogram time phase (hours) def 8 local time
%       .tfh_thr   time_frequency threshold (0 -> no threshold)
%       .noplot    = 0  plot (default)

% Version 2.0 - September 2016
% Part of Snag toolbox - Signal and Noise for Gravitational Antennas
% by O.J.Piccinni and S. Frasca - sergio.frasca@roma1.infn.it
% Department of Physics - Sapienza University - Rome
```

BSD access

Data access function:

```
 [bsd_out,BSD_tab_out,out]=bsd_access(addr,ant,run,tim,freq,mode,modif,modifpost)
%
%    addr      path that contains BSD data master directory without the
 final dirsep
%    ant       antenna name
%    runame    run name
%    tim       [tini tfin] (mjd) ; if length(tim) = 1 the whole run
%    freq      [frini frfin] ; if length(freq) = 1 the full band with frini
%    mode      mode  = 0 only the output table
%                    > 0 creates the output bsd
%                    = 1 automatic
%                    = 2 sub-band of concatenated files
%                    = 20 sub-band, concatenates files (raw way)
%                    = 21 sub-ortho-band
%                    = 3 sub-period, many bands
%                    = 4 inter-bands sub-band
%   modif      (if present) modification structure: modifies accessed primary files
%              e.g. adding signals or sources; see bsd_acc_modif
%              [] no modification
%   modifpost  (if present) modification after the band extraction
% Snag Version 2.0 - October 2016
% Part of Snag toolbox - Signal and Noise for Gravitational Antennas
% by O.J.Piccinni and S. Frasca - sergio.frasca@roma1.infn.it
% Department of Physics - Sapienza University - Rome
```

Some new functions developed for data handling and manipulation using BSD:

```
bsd_5vec.m
bsd_acc_modif.m
bsd_access.m
bsd_access_str.m
bsd_cand.m
bsd_concsubband.m
bsd_dayplot.m
bsd_dopp_sd.m
bsd_extr_subtab.m
bsd_find_peaks.m
bsd_find_peaks_fp.m
bsd_frfilt.m
bsd_fu.m
bsd_fu0.m
bsd_holes.m
bsd_hough.m
bsd_hspot.m
bsd_hspot0.m
bsd_hspot1.m
bsd_hspot2.m
bsd_hspot_fu.m
bsd_hspot_fu_sab.m
bsd_interband.m
BSD_JOB.m
bsd_large_band.m
bsd_largerband.m
bsd_lowres_pows.m
bsd_mock_noise.m
bsd_mode.m
bsd_multi_dopp.m
bsd_name_piece.m
bsd_new_p_v.m
bsd_orthoband.m
bsd_par.m
bsd_patch.m
bsd_peakmap.m
bsd_peakmap_cell.m
bsd_peakmap_cell_err.m
bsd_peakmap_conv.m
```

```
bsd_piece_5vec.m
bsd_pows.m
BSD_PREPJOB.m
bsd_real.m
bsd_refine.m
bsd_refine_0.m
bsd_resamp.m
bsd_resamp0.m
bsd_resamp1.m
bsd_resampA.m
bsd_resenh.m
bsd_reshape.m
bsd_seltab.m
bsd_sid.m
bsd_softinj.m
bsd_specfilt.m
bsd_subband.m
bsd_tfclean.m
bsd_tfstr_add.m
bsd_tfstr_db.m
bsd_timfr_anabasic.m
bsd_v_dv.m
bsd_worm.m
bsd_zeroholes.m
bsd_zerointerv.m
check_bsd_table.m
check_inj.m
conc_bsd.m
conc_bsd - old.m
crea_BSD_table.m
crea_VPstr.m
cut_bsd.m
DIRECT_JOB.m
dopp_corr_residual.m
extr_5vec.m
file_tab_bsd.m
find_5vecphase.m
FOLLOWUP_JOB.m
fu_bsd.m
fu_bsd_patch.m
GENERAL_JOB.m
GENERAL_JOB_0.m
is_bsd.m
load_tab_bsd.m
sfdb09_2bandgds_BSD.m
show_dv.m
signal_5vec_bsd.m
```

`total_clean_gd.m`

Appendix C

Instrumental lines removed for the search

Here are reported the main instrumental lines removed in the search described in the last chapter. This is an incomplete list of known instrumental lines and combs, since the data quality study for O2 is still in progress.

```
Lines cleaning file for O2 up to 610 Hz

Column 1 - frequency spacing (Hz) of comb (or frequency of single line)
Column 2 - comb type (0 - singlet, 1 - comb with fixed width,
 2 - comb with scaling width)
Column 3 - frequency offset of 1st visible harmonic (Hz)
Column 4 - index of first visible harmonic
Column 5 - index of last visible harmonic
Column 6 - width of left band (Hz)
Column 7 - width of right band (Hz)

Lines with known sources in H1:

35.9000 0 0.0 1 1 0.0005  0.0005  % Calibration line
36.7000 0 0.0 1 1 0.0005  0.0005  % Calibration line
37.3000 0 0.0 1 1 0.0005  0.0005  % Calibration line
60.0000 2 0.0 1 9 0.06    0.06    % Power mains
331.900 0 0.0 1 1 0.0005  0.0005  % Calibration line
299.60  0 0.0 1 1 0.25    0.25    % Beam splitter violin mode 1st harmonic region
302.22  0 0.0 1 1 0.08    0.08    % Beam splitter violin mode 1st harmonic region
303.31  0 0.0 1 1 0.10    0.10    % Beam splitter violin mode 1st harmonic region
599.14  0 0.0 1 1 0.08    0.08    % Beam splitter violin mode 1st harmonic region
599.42  0 0.0 1 1 0.08    0.08    % Beam splitter violin mode 2nd harmonic region
604.49  0 0.0 1 1 0.07    0.07    % Beam splitter violin mode 2nd harmonic region
606.67  0 0.0 1 1 0.07    0.07    % Beam splitter violin mode 2nd harmonic region
504.0   0 0.0 1 1 9.0     9.0     % Quad violin mode 1st harmonic region
```

```
Lines with known sources L1:

33.7000 0 0.0 1 1   0.0005  0.0005 % Calibration line
34.7000 0 0.0 1 1   0.0005  0.0005 % Calibration line
35.3000 0 0.0 1 1   0.0005  0.0005 % Calibration line
331.300 0 0.0 1 1   0.0005  0.0005 % Calibration line
60.0000 2 0.0 1 10  0.06    0.06   % Power mains
305.9   0 0.0 1 1   0.3     0.3    % Beam splitter violin mode 1st harmonic region
307.34  0 0.0 1 1   0.01    0.01   % Beam splitter violin mode 1st harmonic region
307.5   0 0.0 1 1   0.05    0.05   % Beam splitter violin mode 1st harmonic region
315.1   0 0.0 1 1   0.3     0.3    % Beam splitter violin mode 1st harmonic region
333.33  0 0.0 1 1   0.01    0.01   % Beam splitter violin mode 1st harmonic region
508.5   0 0.0 1 1   11.5    11.5   % Quad violin mode 1st harmonic region
```

Bibliography

[1] Aasi, J., et al. The characterization of Virgo data and its impact on gravitational-wave searches. *Class. Quantum Gravity*, **29** (2012), 155002. `arXiv:1203.5613`.

[2] Aasi, J., et al. A directed search for continuous Gravitational Waves from the Galactic Center. *Phys. Rev. D - Part. Fields, Gravit. Cosmol.*, **88** (2013), 1. `arXiv:1309.6221`.

[3] Aasi, J., et al. Advanced LIGO. *Class. Quantum Gravity*, **32** (2015), 074001.

[4] Aasi, J., et al. Searches for Continuous Gravitational Waves From Nine Young Supernova Remnants. *Astrophys. J.*, **813** (2015), 39. `arXiv:1412.5942`.

[5] Aasi, J., et al. First low frequency all-sky search for continuous gravitational wave signals. *Phys. Rev. D*, **93** (2016), 42007. `arXiv:1510.03621`.

[6] Aasi, J., et al. Search of the Orion spur for continuous gravitational waves using a loosely coherent algorithm on data from LIGO interferometers. *Phys. Rev. D*, **93** (2016), 1. `arXiv:1510.03474`.

[7] Abbott, B. B. P. P., et al. Observation of gravitational waves from a binary black hole merger. *Phys. Rev. Lett.*, **116** (2016), 061102. `arXiv:1602.03837`.

[8] Abbott, B. P., et al. Binary Black Hole Mergers in the First Advanced LIGO Observing Run. *Phys. Rev. X*, **6** (2016), 041015.

[9] Abbott, B. P., et al. GW151226: Observation of Gravitational Waves from a 22-Solar-Mass Binary Black Hole Coalescence. *Phys. Rev. Lett.*, **116** (2016), 241103. `arXiv:1602.03837`.

[10] Abbott, B. P., et al. Observing gravitational-wave transient GW150914 with minimal assumptions. *Phys. Rev. D*, **93** (2016), 122004. `arXiv:1602.03843`.

[11] Abbott, B. P., et al. Properties of the Binary Black Hole Merger GW150914. *Phys. Rev. Lett.*, **116** (2016). `arXiv:1602.03840`.

[12] Abbott, B. P., et al. Tests of General Relativity with GW150914. *Phys. Rev. Lett.*, **116** (2016), 221101.

[13] Abbott, B. P., et al. All-sky search for short gravitational-wave bursts in the first Advanced LIGO run. *Phys. Rev. D*, **95** (2017), 042003. `arXiv:1611.02972`.

[14] Abbott, B. P., et al. Directional Limits on Persistent Gravitational Waves from Advanced LIGO's First Observing Run. *Phys. Rev. Lett.*, **118** (2017), 121102. `arXiv:1612.02030`.

[15] Abbott, B. P., et al. First Search for Gravitational Waves from Known Pulsars with Advanced LIGO. *Astrophys. J.*, **839** (2017), 12. `arXiv:1701.07709`.

[16] Abbott, B. P., et al. Gravitational Waves and Gamma-Rays from a Binary Neutron Star Merger: GW170817 and GRB 170817A. *Astrophys. J.*, **848** (2017), L13.

[17] Abbott, B. P., et al. GW170104: Observation of a 50-Solar-Mass Binary Black Hole Coalescence at Redshift 0.2. *Phys. Rev. Lett.*, **118** (2017), 221101. `arXiv:1706.01812`.

[18] Abbott, B. P., et al. GW170814: A Three-Detector Observation of Gravitational Waves from a Binary Black Hole Coalescence. *Phys. Rev. Lett.*, **119** (2017), 141101.

[19] Abbott, B. P., et al. Multi-messenger Observations of a Binary Neutron Star Merger. *Astrophys. J. Lett.*, **848** (2017), L12.

[20] Abbott, B. P., et al. Search for continuous gravitational waves from neutron stars in globular cluster NGC 6544. *Phys. Rev. D*, **95** (2017), 082005. `arXiv:1607.02216`.

[21] Abbott, B. P., et al. Search for Gravitational Waves Associated with Gamma-Ray Bursts during the First Advanced LIGO Observing Run and Implications for the Origin of GRB 150906B. *Astrophys. J.*, **841** (2017), 89. `arXiv:1611.07947`.

[22] Abbott, B. P., et al. Upper Limits on Gravitational Waves from Scorpius X-1 from a Model-Based Cross-Correlation Search in Advanced LIGO Data. *Astrophys. J.*, **847** (2017), 47. `arXiv:1706.03119`.

[23] Abbott, B. P., et al. Upper Limits on the Stochastic Gravitational-Wave Background from Advanced LIGO's First Observing Run. *Phys. Rev. Lett.*, **118** (2017), 121101. `arXiv:1612.02029`.

[24] Accadia, T., et al. The NoEMi (Noise Frequency Event Miner) framework. *J. Phys. Conf. Ser.*, **363** (2012), 012037.

[25] Acernese, F., et al. Cleaning the Virgo sampled data for the search of periodic sources of gravitational waves. *Class. Quantum Gravity*, **26** (2009), 204002.

[26] Acernese, F., et al. Advanced Virgo: a second-generation interferometric gravitational wave detector. *Class. Quantum Gravity*, **32** (2015), 024001. `arXiv:1408.3978`.

[27] Antonucci, F., Astone, P., Antonio, S. D., Frasca, S., and Palomba, C. Detection of periodic gravitational wave sources by Hough transform in the frequency and spin down plane. (2008). `arXiv:0807.5065`.

[28] Astone, P., Frasca, S., Palomba, C., and Moro, P. A. The short FFT database and the peak map for the hierarchical search of periodic sources. *Class. Quantum Grav*, **22** (2005), 1197.

[29] Astone, P., et al. A method for detection of known sources of continuous gravitational wave signals in non-stationary data. *Class. Quantum Gravity*, **27** (2010), 194016.

[30] Astone, P., et al. Method for all-sky searches of continuous gravitational wave signals using the frequency-Hough transform. *Phys. Rev. D - Part. Fields, Gravit. Cosmol.*, **90** (2014), 1. `arXiv:1407.8333`.

[31] ATNF. The ATNF Pulsar Database.

[32] Baade, W. and Zwicky, F. Supernovae and Cosmic Rays. *Phys. Rev.*, **45** (1934), 138.

[33] Balick, B. and Sanders, R. H. Radio Fine Structure in the Galactic Center. *Astrophys. J.*, **192** (1974), 325.

[34] Bartels, R., Krishnamurthy, S., and Weniger, C. Strong Support for the Millisecond Pulsar Origin of the Galactic Center GeV Excess. *Phys. Rev. Lett.*, **116** (2016). `arXiv:1506.05104`.

[35] Bell, A. R. Cosmic ray acceleration. *Astropart. Phys.*, **43** (2013), 56.

[36] Bono, G., Matsunaga, N., Inno, L., Lagioia, E. P., and Genovali, K. Stellar Populations in the Galactic Center. (2013), 1. `arXiv:1304.6211`.

[37] Chennamangalam, J. and Lorimer, D. R. The Galactic Centre pulsar population. *Mon. Not. R. Astron. Soc. Lett.*, **440** (2014), 86. `arXiv:1311.4846`.

[38] Deil, C. *HESS & FERMI Surveys of the Galactic Gamma-ray Source Population*. Ph.D. thesis (2011).

[39] Dobbs, C. L. and Burkert, A. The myth of the molecular ring. *Mon. Not. R. Astron. Soc.*, **421** (2012), 2940. `arXiv:1201.1775`.

[40] Einstein, A. and Albert. Über Gravitationswellen. *Sitzungsberichte der Königlich Preußischen Akad. der Wissenschaften (Berlin), Seite 154-167.*, (1918).

[41] Finn, L. S. and Chernoff, D. F. Observing binary inspiral in gravitational-radiation - one interferometer. *Phys. Rev. D*, **47** (1993), 2198. `arXiv:9301003`.

[42] Gabor, D. Theory of communication. *J Inst. Electr. Eng.*, **93** (1946), 429.

[43] Genzel, R., Eisenhauer, F., and Gillessen, S. The Galactic center massive black hole and nuclear star cluster. *Rev. Mod. Phys.*, **82** (2010), 3121. `arXiv:1006.0064`.

[44] Hartle, J. B. *Gravity: An Introduction to General Relativity.* Addison Wesley (2003).

[45] Hemming, G. and Verkindt, D. Virgo Interferometer Monitoring (VIM) (2017).

[46] HEWISH, A., BELL, S. J., PILKINGTON, J. D. H., SCOTT, P. F., and COLLINS, R. A. Observation of a Rapidly Pulsating Radio Source. *Nature*, **217** (1968), 709.

[47] Hodge, P. W. The Hubble type of the Milky Way Galaxy. *Publ. Astron. Soc. Pacific*, **95** (1983), 721.

[48] Hong, J., et al. <i>NuSTAR</i> HARD X-RAY SURVEY OF THE GALACTIC CENTER REGION. II. X-RAY POINT SOURCES. *Astrophys. J.*, **825** (2016), 132.

[49] Horowitz, C. J. and Kadau, K. Breaking strain of neutron star crust and gravitational waves. *Phys. Rev. Lett.*, **102** (2009), 191102. `arXiv:0904.1986`.

[50] Idrisy, A., Owen, B. J., and Jones, D. I. R -mode frequencies of slowly rotating relativistic neutron stars with realistic equations of state. *Phys. Rev. D - Part. Fields, Gravit. Cosmol.*, **91** (2015). `arXiv:1410.7360`.

[51] Jaranowski, P., Królak, A., and Schutz, B. F. Data analysis of gravitational-wave signals from spinning neutron stars: The signal and its detection. *Phys. Rev. D*, **58** (1998), 063001. `arXiv:9804014`.

[52] Kaspi, V. M. and Beloborodov, A. M. Magnetars. *Annu. Rev. Astron. Astrophys.*, **55** (2017), 261. `arXiv:1703.00068`.

[53] Krishnan, B., Sintes, A. M., Papa, M. A., Schutz, B. F., Frasca, S., and Palomba, C. Hough transform search for continuous gravitational waves. *Phys. Rev. D - Part. Fields, Gravit. Cosmol.*, **70** (2004), 1. `arXiv:0407001`.

[54] Kunneriath, D., et al. The Galactic centre mini-spiral in the mm-regime. *Astron. Astrophys.*, **538** (2012), A127. `arXiv:1201.2362`.

[55] LASER INTERFEROMETER GRAVITATIONAL WAVE OBSERVATORY. Specification of a Common Data Frame Format for Interferometric Gravitational Wave Detectors (IGWD) (2009).

[56] Lasky, P. D. Gravitational Waves from Neutron Stars: A Review. *Publ. Astron. Soc. of Aust.*, **32** (2015), e034. `arXiv:1508.06643`.

[57] LIGO Scientific Collaboration, et al. All-sky Search for Periodic Gravitational Waves in the O1 LIGO Data (2017). `arXiv:1707.02667`.

[58] Lorimer, D. The Galactic Millisecond Pulsar Population. *IAU Symp.*, **291** (2013), 237. `arXiv:1210.2746`.

[59] Macquart, J.-P. J.-P. and Kanekar, N. On Detecting Millisecond Pulsars At the Galactic Center. *Astrophys. J.*, **805** (2015), 172. `arXiv:arXiv:1504.02492v1`.

[60] Maggiore, M. *Gravitational Waves – Volume 1: Theory and Experiments.* Oxford University Press (2008).

[61] Manchester, R. N., Hobbs, G. B., Teoh, A., and Hobbs, M. The ATNF Pulsar Catalogue. *Astron.J*, **129** (2005), 1993. `arXiv:0412641`.

[62] Martynov, D. V., et al. Sensitivity of the Advanced LIGO detectors at the beginning of gravitational wave astronomy. *Phys. Rev. D*, **93** (2016). `arXiv:1604.00439`.

[63] McGee, R. X. and Bolton, J. G. Probable observation of the galactic nucleus at 400 Mc./s. *Nature*, **173** (1954), 985.

[64] Meadors, G. D., Goetz, E., Riles, K., Creighton, T., and Robinet, F. Searches for continuous gravitational waves from Scorpius X-1 and XTE J1751-305 in LIGO's sixth science run. *Phys. Rev. D*, **95** (2017). `arXiv:arXiv:1610.09391v1`.

[65] Merritt, D. the Distribution of Stars and Stellar Remnants At the Galactic Center. *Astrophys. J.*, **718** (2010), 739. `arXiv:0909.1318`.

[66] Misner, C. W., Thorne, K. S., and Wheeler, J. A. *Gravitation.* W. H. Freeman (1973).

[67] Mori, K., et al. NuSTAR HARD X-RAY SURVEY OF THE GALACTIC CENTER REGION. I. HARD X-RAY MORPHOLOGY AND SPECTROSCOPY OF THE DIFFUSE EMISSION. *Astrophys. J.*, **814** (2015), 94. `arXiv:1510.04631`.

[68] Muno, M. P., et al. A CATALOG OF X-RAY POINT SOURCES FROM TWO MEGASECONDS OF <i>CHANDRA</i> OBSERVATIONS OF THE GALACTIC CENTER. *Astrophys. J. Suppl. Ser.*, **181** (2009), 110. `arXiv:0809.1105`.

[69] Murphy, E. J., et al. Science with the VLA Sky Survey (VLASS). *Am. Astron. Soc. AAS Meet. #225, id.113.03*, **225** (2015).

[70] Owen, B. J. Maximum elastic deformations of compact stars with exotic equations of state. *Phys. Rev. Lett.*, **95** (2005). `arXiv:0503399`.

[71] Özel, F. and Freire, P. Masses, Radii, and the Equation of State of Neutron Stars. *Annu. Rev. Astron. Astrophys.*, **54** (2016), 401. `arXiv:1603.02698`.

[72] Palomba, C. Simulation of a population of isolated neutron stars evolving through the emission of gravitational waves. *Mon. Not. R. Astron. Soc.*, **359** (2005), 1150. `arXiv:0503046`.

[73] Palomba, C. The search for continuous gravitational waves with LIGO and Virgo detectors Cristiano Palomba, for the LIGO and Virgo Collaborations. In *Eur. Phys. Soc. Conf. High Energy Phys.*, vol. 5 (2017).

[74] Palomba, C., Astone, P., and Frasca, S. Adaptive Hough transform for the search of periodic sources. *Class. Quantum Gravity*, **22** (2005), S1255.

[75] Payne, D. J. B., Vigelius, M., and Melatos, A. Burial of the polar magnetic field of an accreting neutron star and gravitational wave emission. In *AIP Conf. Proc.*, vol. 968, pp. 227–232. Oxford University Press (2008). ISBN 9780735404854.

[76] Perez, K., et al. Extended hard-X-ray emission in the inner few parsecs of the Galaxy. *Nature*, **520** (2015), 646.

[77] Pfahl, E. and Loeb, A. Probing the Spacetime around Sagittarius A* with Radio Pulsars. *Astrophys. J.*, **615** (2004), 253. `arXiv:0309744`.

[78] Piccinni, O. J. An enhanced sensitivity procedure for continuous gravitational-wave detection. In *Nuovo Cim. C - SciNeGHE 2016*, p. 125 (2017).

[79] Piddington, J. H. and Minnett, H. C. Observations of galactic radiation at frequencies of 1200 and 3000 Mc/s. *Aust. J. Chem.*, **4** (1951), 459.

[80] Rajwade, K., Lorimer, D., and Anderson, L. Detecting pulsars in the Galactic centre. *Mon. Not. R. Astron. Soc*, **000** (2016), 1. `arXiv:1611.06977`.

[81] Rea, N., et al. a Strongly Magnetized Pulsar Within the Grasp of the Milky Way'S Supermassive Black Hole. *Astrophys. J.*, **775** (2013), L34. `arXiv:arXiv:1307.6331v3`.

[82] Regimbau, T. The astrophysical gravitational wave stochastic background. *Res. Astron. Astrophys.*, **11** (2011), 369. `arXiv:1101.2762`.

[83] Riles, K. Gravitational waves: Sources, detectors and searches (2013). `arXiv:1209.0667`.

[84] Saluson, P. R. *Fundamentals of Interferometric Gravitational Wave Detectors* (1994).

[85] Sathyaprakash, B., et al. Scientific objectives of Einstein Telescope. *Class. Quantum Gravity*, **29** (2012), 124013. `arXiv:1206.0331`.

[86] Schödel, R. and Others. The structure of the nuclear stellar cluster of the Milky Way. *aap*, **469** (2007), 125. `arXiv:0703178v1`.

[87] Schutz, B. F. *A First Course in General Relativity, Second Edition* (2015).

[88] The LIGO Scientific Collaboration and the Virgo Collaboration. Effects of Data Quality Vetoes on a Search for Compact Binary Coalescences in Advanced LIGO's First Observing Run. (2017). `arXiv:1710.02185`.

[89] The LIGO Scientific Collaboration, et al. First low-frequency Einstein@Home all-sky search for continuous gravitational waves in Advanced LIGO data. (2017). `arXiv:1707.02669`.

[90] The LIGO Scientific Collaboration, et al. First narrow-band search for continuous gravitational waves from known pulsars in advanced detector data. (2017). `arXiv:1710.02327`.

[91] The LIGO Scientific Collaboration, T. L. S., et al. Characterization of the LIGO detectors during their sixth science run. (2014). `arXiv:1410.7764`.

[92] Ville, A. Theorie et application de la notion du signal analytique. *IEEE Trans. Acoust.*, **26** (1978), 467.

[93] Walsh, S., et al. Comparison of methods for the detection of gravitational waves from unknown neutron stars. *Phys. Rev. D*, **94** (2016). `arXiv:1606.00660`.

[94] Yee, J. C., et al. The Science Case for an Extended Spitzer Mission. (2017).

[95] Yusef-Zadeh, F., et al. Star Formation in the Central 400 pc of the Milky Way: Evidence for a Population of Massive YSOs. *Astrophys. J.*, **702** (2009), 178. `arXiv:arXiv:0905.2161v1`.

[96] Zelati, F. C., et al. Chandra monitoring of the Galactic Centre magnetar SGR J1745-2900 during the initial 3.5 years of outburst decay. *Mon. Not. R. Astron. Soc.*, **471** (2017), 1819. `arXiv:1707.01514`.

[97] Zhu, S. J., et al. Einstein@Home search for continuous gravitational waves from Cassiopeia A. *Phys. Rev. D*, **94** (2016), 082008. `arXiv:1608.07589`.